

UNIVERSITY OF NAPLES FEDERICO II

PhD. Program in Structural, Geotechnical Engineering
and Seismic Risk - XXXIV Cycle



Thesis for the Degree of Doctor of Philosophy

Innovative structures obtained with Digital Fabrication technologies

by

Laura Esposito

Advisor: Prof. Ing. Costantino Menna

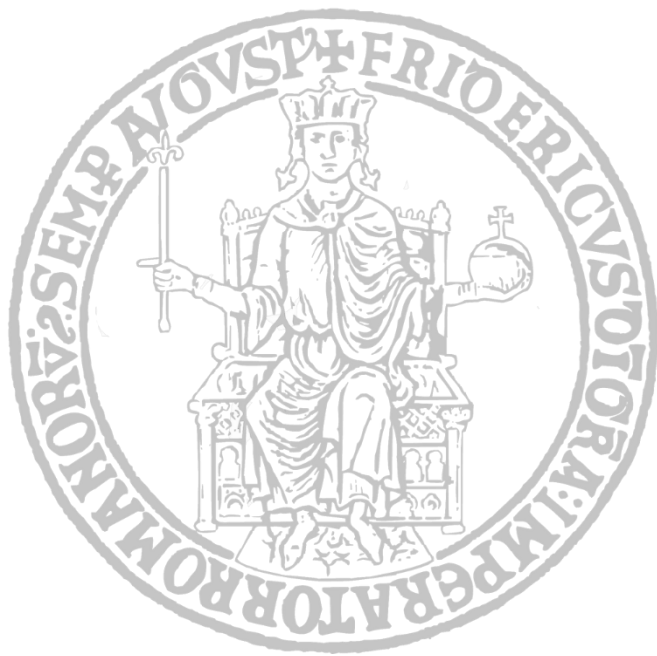
Scuola Politecnica e delle Scienze di Base
Dipartimento di Strutture per l'Ingegneria e l'Architettura

La borsa di dottorato è stata cofinanziata con risorse del
Programma Operativo Nazionale Ricerca e Innovazione 2014-2020 (CCI 2014IT16M2OP005),
Fondo Sociale Europeo, Azione I.1 "Dottorati Innovativi con caratterizzazione Industriale"



UNIONE EUROPEA
Fondo Sociale Europeo





Innovative Structures Obtained With Digital Fabrication Technologies

Ph.D. Thesis presented for the fulfillment of the Degree of Doctor of
Philosophy in Ingegneria Strutturale, Geotecnica e Rischio Sismico

by

Laura Esposito

2022



Approved as to style and content by

Advisor: Prof. Ing. Costantino Menna

University of Naples Federico II
Ph.D. Program in Ingegneria Strutturale, Geotecnica e Rischio Sismico
XXXIV cycle - Chairman: Prof. Iunio Iervolino



www.dist.unina.it/dottorati-di-ricerca/dottorati

Candidate's declaration

I hereby declare that this thesis submitted to obtain the academic degree of Philosophiæ Doctor (PhD) in Ingegneria Strutturale, Geotecnica e Rischio Sismico is my own unaided work, that I have not used other than the sources indicated, and that all direct and indirect sources are acknowledged as references.

Parts of this dissertation have been published in international journals and/or conference articles (see list of the author's publications at the end of the thesis).

Naples, March 11, 2022

Laura Esposito

Abstract

Digital Fabrication with Concrete is now emerging in the civil engineering field since it enables the construction of complex shape structures with a high level of digitalisation. The potentialities of digital fabrication employment in the construction field are many, and, to fully exploit them, it is necessary to expand the technical "know-how". The technological progress in this sector has recently grown, resulting in the design and realisation of numerous structural projects. However, different challenges must be solved concerning the cementitious material requirements and characterisation, code compliance, and definition of a structural design approach. The present work is collocated within this scenario to explore and address critical issues related to the most widespread additive manufacturing technique: 3D Concrete Printing (3DCP). This technology consists of a continuous extrusion of concrete filament through a nozzle attached to a robotic system, and it is based on early-age material requirements satisfaction (pumpability, extrudability and buildability). Therefore, the first topic addressed in this thesis work is the physical-mechanical characterisation of the fresh printable mortars. Specific testing procedures and experimental methods were developed to determine the main material properties (such as strength and stiffness under axial compressive load) and their evolution with the cement hardening process and build up progressing. These studies were performed in collaboration with the industrial partner Italcementi Heidelberg Cement Group. Experimental results were used to define an appropriate constitutive model that took into account the complex visco-elastic response of such innovative mortars. Moving to the hardened state of the printed structures, the reinforcement strategy was investigated since the cementitious material is brittle and has low tensile strength. In this framework, an interlaboratory study with a foreign institute (ETH Zürich) was conducted to investigate the steel bar reinforcement effectiveness (in terms of bond behaviour), focusing on the influence of the material/printing setup. The comparison between printed and cast pull-out specimens, made with a different

type of printable mortars and realised with two different printing setups, allowed understanding the main influencing factors of steel reinforcement inclusion. As a final step of the thesis work, the mechanical response of 3D printed structural elements was investigated through flexural tests carried out on topology optimised beams. For such beams, the effect on the resistance mechanism of the previously mentioned reinforcement strategy was also examined.

The thesis work addresses different but strictly correlated topics of the 3DCP technology concerning the design, production and testing of the structural element obtained. The presented research activities and the experimental results could be helpful for the standardisation of the testing procedures (for the material characterisation) and design approaches in the 3DCP field.

Keywords: 3D Concrete Printing, early-age material behaviour, analytical modelling, reinforcement strategy, 3D printed topology optimised beams.

Sintesi in lingua italiana

La Fabbricazione Digitale con il calcestruzzo sta emergendo sempre più nel campo dell'ingegneria civile poiché consente la costruzione di strutture di forme complesse grazie ad un elevato livello di digitalizzazione. Molteplici sono le potenzialità della fabbricazione digitale nel settore delle costruzioni, e, per sfruttarle appieno, è necessario accrescere il “know-how” tecnico. Il progresso tecnologico in questo settore ha permesso di portare a termine numerosi progetti strutturali. Tuttavia, essendo un campo così innovativo, numerose sono le sfide che ancora devono essere risolte, le quali risultano principalmente legate alla caratterizzazione dei materiali cementizi, alla conformità dei prodotti della fabbricazione con le normative attuali in tema di costruzioni ed alla definizione di un approccio di progettazione strutturale. Il presente lavoro si inserisce all'interno di questo scenario per esplorare e affrontare le questioni critiche relative alla tecnica di produzione additiva più diffusa: la stampa 3D con il calcestruzzo (3DCP). Questa tecnologia consiste in un'estrusione continua di un filamento di calcestruzzo attraverso un ugello collegato ad un sistema robotico. Poiché il processo si basa sul soddisfacimento di alcuni requisiti del materiale cementizio (pumpability, extrudability e buildability), il primo argomento affrontato in questo lavoro di tesi è la caratterizzazione fisico-meccanica delle malte stampabili allo stato fresco. In particolare, sono state sviluppate specifiche procedure di prova e metodi sperimentali per determinare le principali proprietà del materiale (come la resistenza e la rigidità in stato di compressione uniassiale) e la loro evoluzione con il processo di indurimento del cemento. Questi studi sono stati realizzati in collaborazione con il partner industriale Italcementi Heidelberg Cement Group. I risultati sperimentali sono stati successivamente utilizzati per definire un modello costitutivo appropriato, che tenesse conto della complessa risposta visco-elastica di tali malte innovative. Passando dallo stato fresco del materiale a quello indurito, sono state analizzate le possibili strategie di rinforzo, dato che il materiale cementizio è noto per essere fragile e con una bassa resistenza a

trazione. In questo contesto, è stato condotto uno studio interlaboratorio con un istituto straniero (ETH Zürich) per indagare l'efficacia del rinforzo strutturale in elementi stampati, studiando il comportamento del legame di interfaccia. Il confronto tra campioni stampati e gettati, realizzati con un diverso tipo di malta e con due diverse configurazioni di stampa, ha permesso di comprendere i principali fattori che influenzano l'inclusione del rinforzo. Come fase finale del lavoro di tesi, è stata studiata ed analizzata la risposta meccanica di elementi strutturali stampati in 3D attraverso l'esecuzione di prove di flessione su travi ottimizzate topologicamente. Per tali travi, è stato esaminato anche l'effetto dell'inclusione del rinforzo strutturale sul meccanismo di resistenza.

Il lavoro di tesi affronta differenti, ma strettamente correlati, argomenti della tecnologia 3DCP riguardanti la progettazione, la produzione e la sperimentazione degli elementi strutturali stampati. Le attività di ricerca e i risultati sperimentali di seguito presentati possono essere utili nell'ottica di una standardizzazione delle procedure di prova (per la caratterizzazione dei materiali) e degli approcci di progettazione nel settore della stampa 3D in calcestruzzo.

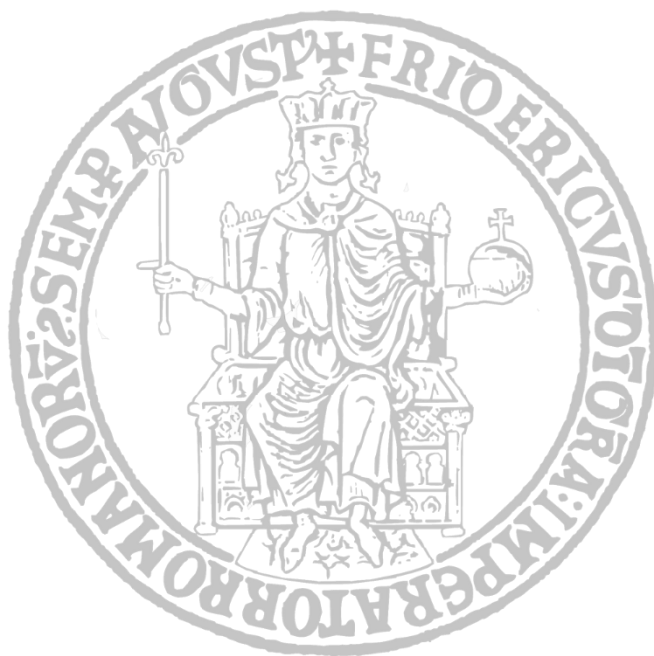
Parole chiave: Stampa 3D del calcestruzzo, comportamento del materiale allo stato fresco, modellazione analitica, rinforzo strutturale, travi stampate topologicamente ottimizzate.

Contents

Overview	26
1. Digital fabrication with concrete: main characteristics	30
1.1 Printable cement-based materials	34
1.2 Reinforcement strategies in 3DCP and case studies	36
2. Early age behaviour of 3D printable mortars	42
2.1 Uniaxial compressive behaviour	45
2.1.1 Effect of testing procedures.....	48
2.1.1.1 Methodological approach.....	49
2.1.1.2 Results and discussion.....	56
2.1.1.3 Failure prediction during printing	70
2.1.1.4 Remarks and recommendation	73
2.1.2 UUCTs: strength and stiffness evaluation.....	75
2.1.2.1 Experimental program.....	76
2.1.2.2 Results and discussion.....	78
2.1.3 Conclusive remarks.....	81
2.2 Early-age creep behaviour.....	83
2.2.1 Theoretical background.....	86
2.2.2 Determination of deformation under constant load.....	89
2.2.2.1 Experimental method	89
2.2.2.2 Experimental results and Burgers' model calibration	93
2.2.2.3 Analytical model validation	98
2.2.3 Deformation under printing-type loading history.....	103

2.2.3.1	Proposal of an experimental protocol.....	104
2.2.3.2	Experimental results and Burges' model calibration.....	106
2.2.3.3	Analytical collapse prediction models and experimental validation	116
2.2.4	Conclusion.....	124
3.	Reinforced printed elements: approach and characterisation.....	128
3.1	Interlaboratory study: UniNa and ETHZ.....	131
3.2	Materials and Methods.....	132
3.3	Specimens layout and production.....	137
3.4	Pull-out Testing.....	140
3.5	Results and Discussion.....	142
3.5.1	Overview.....	142
3.5.2	Bond-slip behaviour.....	143
3.5.3	Comparison with Model Code 2010 and existing literature.	146
3.5.4	Hardened properties from cut printed samples.....	149
3.6	Proposal for standardisation.....	151
3.7	Conclusion.....	152
4.	Topology optimised beams.....	154
4.1.1	Theoretical framework and optimisation algorithm.....	155
4.1.2	Beam layout and printing production.....	158
4.1.3	Steel reinforced topology optimised beams fabrication.....	162
4.1.4	Testing method.....	165
4.1.5	Experimental results and discussion.....	167
4.1.6	Conclusion.....	179
5.	Conclusion.....	182

Bibliography.....	188
Author's publications	202



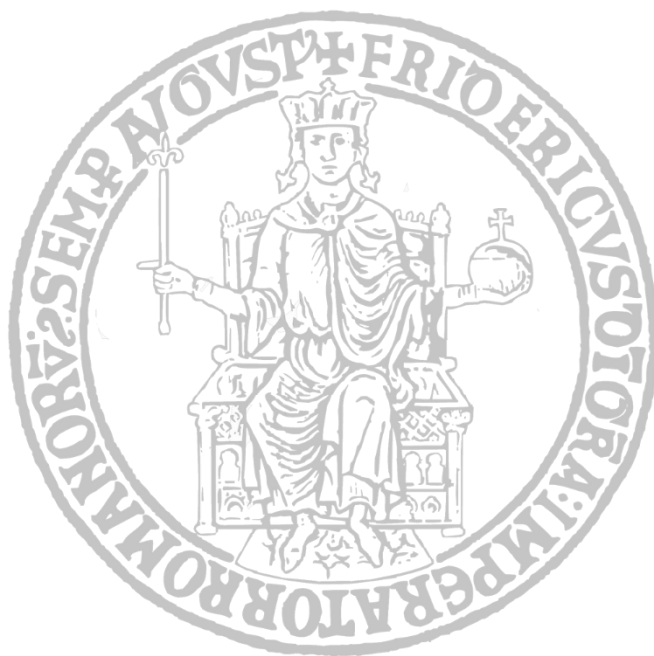
Acknowledgements

Firstly, I would like to express my gratitude to my tutor, Prof. Costantino Menna, for the continuous guidance and support during these years of my PhD study. Moreover, I would like to thank the reviewers of my thesis, Prof. Liberato Ferrara and Prof. Ezio Cadoni: their helpful recommendations are gratefully appreciated.

The experimental tests were partially performed in collaboration with the industrial partner Italcementi Heidelberg Cement S.p.A. at i.lab in Bergamo (Italy) during the period spent in the company. I would like to thank my tutors, Chiara Rossino and Maurizio Marchi, for their assistance and advice during the research activities.

Furthermore, part of the experimental activities presented in this thesis was designed and carried out in collaboration with the foreign Institute of Structural Engineering (IBK) at ETH Zürich during the research period spent abroad.

The research presented in this dissertation has been supported by the Italian Ministry of University and Research (MIUR) under program PON 2014-2020 (CCI 2014IT16M2OP005, Fondo Sociale Europeo, Azione I.1 “Dottorati Innovativi con caratterizzazione industriale”).



List of Figures

Figure 1-1: The RILEM process classification framework for DFC technologies [9].	32
Figure 1-2: Example of (a) 4 axis gantry system (Eindhoven, [20]) and (b) 6-axis robotic arm (Naples).	33
Figure 1-3: Number of projects realised with additive manufacturing (since the concept inception in 1997) [14].	34
Figure 1-4: Shear stress as a function of shear strain [21].	35
Figure 1-5: Examples of collapse during printing: (a) empirical buildability test geometry (from [14]) and (b) failure of a hollow cylinder (from [25]).	36
Figure 1-6: Reinforcement of 3DCP structures: placement of (a) straight reinforcement bars [29] and (b) steel bar truss in the print plane [30].	37
Figure 1-7: External reinforcement system with tightened bars [32].	38
Figure 1-8: (a) Entrained cable into the concrete filament [34] and (b) bicycle bridge developed at the TU/e [35].	38
Figure 1-9: 3D printing of a post-tensioned concrete beam designed by topology optimisation – Ghent University [36].	39
Figure 1-10: 3D Printed prestressed pedestrian bridge designed through topology optimisation approach (Kinomura et al. 2020 [38]).	40
Figure 2-1: 3D-printed openable mould: closed, open, positioning of the nylon membrane, example of a prepared sample.	51
Figure 2-2: Compression tests - REF-SP0.10-M-DR3. Average and individual results at different times : (a) 0 minutes, (b) 15 minutes, (c) 30 minutes, (d) 60 minutes. (UniNa mortar).	57

Figure 2-3: Effect of age: REF-SP0.10-M-DR3. Average comparison: (a) stress-strain curves & (b) compressive strength with the standard deviation. (UniNa mortar)..... 58

Figure 2-4: Samples prepared with different superplasticiser values: (a) REF-SP0.10-M-DR3, (b) SP0.00-M-DR3, (c) SP0.15-M-DR3, and (d) SP0.00-NM-DR3. 60

Figure 2-5: Effect of the printing condition, the average stress-strain curves: a) REF-SP0.10-M-DR3, (b) SP0.00-M-DR3, and (c) SP0.15-M-DR3. (UniNa mortar)..... 61

Figure 2-6: Effect of the printing condition and compressive strength, with the standard deviation. (UniNa mortar) 61

Figure 2-7: Effect of specimen preparation, average stress-strain curves: a) REF-SP0.10-M-DR3, (b) SP0.10-NM-DR3, (c) SP0.00-M-DR3, and (d) SP0.00-NM-DR3. (UniNa mortar)..... 62

Figure 2-8: Effect of specimen preparation, average compressive strength with the standard deviation: a) REF-SP0.10-M-DR3, SP0.00-M-DR3, SP0.00-NM-DR3, and (b) REF-SP0.10-M-DR3, SP0.10-NM-DR3. (UniNa mortar) 63

Figure 2-9: Effect of the displacement rate, average stress-strain curves: a) REF-SP0.10-M-DR3 and b) SP0.10-M-DR30. (UniNa mortar)..... 64

Figure 2-10: Effect of the displacement rate, average compressive strength, with the standard deviation. (UniNa mortar)..... 64

Figure 2-11: Evolution over time of the compressive strength (a) and Young's modulus (b). (UniNa mortar) 68

Figure 2-12: Evolution over time of the compressive strength (a) and Young's modulus (b) for different superplasticiser percentage values. (UniNa mortar) 68

Figure 2-13: Evolution over time of the compressive strength (a) and Young's modulus (b) with and without the membrane and with SP=0.10%. (UniNa mortar)..... 69

Figure 2-14: Evolution over time of the compressive strength (a) and Young's modulus (b) with and without the membrane and with SP=0.00%. (UniNa mortar)..... 69

Figure 2-15: Evolution over time of the compressive strength (a) and Young's modulus (b) for different displacement rate values. (UniNa mortar) 69

Figure 2-16: Comparison between the compressive strength and the vertical stress (red curves) and between the Young's modulus and the critical elastic modulus (blue curves) for the reference mix..... 72

Figure 2-17: Summary of analytical failure prediction - maximum layers' number - for each case examined: (a) analytical method, i.e. Equation 2-2 and Equation 2-5, and (b) failure mechanism map, i.e., Suiker [56] 73

Figure 2-18: (a) 3D printed plastic mould and (b) specimen demoulding. 76

Figure 2-19: Testing setup: MTS electromechanical Universal Testing Machine..... 77

Figure 2-20: Average stress-strain curves: a) i.tech N, (b) i.tech NF (DR30) 78

Figure 2-21: Average stress-strain curves: a) i.tech N, (b) i.tech NF (DR5) .. 79

Figure 2-22: Young's Modulus: a) i.tech N, (b) i.tech NF. 79

Figure 2-23: Compressive strength: a) i.tech N, (b) i.tech NF. 79

Figure 2-24: Linear viscoelastic model: (a) Maxwell, (b) Kelvin-Voigt and (c) Burgers. 89

Figure 2-25: Schematisation of the Burgers' model creep response (constant load between t_0 and t_F). 89

Figure 2-26: (a) Sketch and tested specimen and (b) loading history. 90

Figure 2-27: Logic scheme of the iterative process for experimental procedure and Burgers' model calibration. 91

Figure 2-28: Recorded testing head force for a Displacement Rate (DR) equal to 30 mm/min: (a) total testing time, (b) zoom detail. 94

Figure 2-29: Individual and average experimental total strain VS testing time for each considered resting time: (a) 0, (b) 15, (c) 30 and (d) 60 minutes. 95

Figure 2-30: Experimental strain: (a) average total strain vs time curves, (b) elastic vs average early-age creep strain for each considered resting time: (a) 0, (b) 15, (c) 30 and (d) 60 minutes.....	95
Figure 2-31: Time t_0 as a function of the material hardening.....	96
Figure 2-32: Time-dependent laws of Burgers' parameters: a) Maxwell and b) Voigt stiffness, and c) relaxation time.	97
Figure 2-33: Average experimental VS analytical temporal evolution of total strain curves.	98
Figure 2-34: Simulation of one-, two- and three-layer stacking sequence repeated for different resting times.	99
Figure 2-35: Simulation of the stacking process: Experimental VS Analytical total strain vs time curves.....	100
Figure 2-36: Vertical displacement prediction – Burgers' Model.....	102
Figure 2-37: (a) Schematic representation of the stress history acting on the first layer (b) Testing set-up and (c) strain vs time visco-elastic response.....	105
Figure 2-38: Vertical strain vs time curves for each tested specimen (Italcementi mortars).....	106
Figure 2-39: Burgers model calibration approach.....	110
Figure 2-40: Fitting of experimental strain vs time curve for the first load step (i.e. at 0 minutes of resting time)	111
Figure 2-41: i.tech N calibration: (a) evolution of the Burgers functions and (b) Experimental vs Burgers curves ($RSS_{sum}=0.049$).	113
Figure 2-42: i.tech NF calibration: (a) evolution of the Burgers functions and (b) Experimental vs Burgers curves ($RSS_{sum}=0.0211$)......	114
Figure 2-43: Experimental strain vs time curves fitting using a stress rate dependent Burgers model: (a) i.tech N and (b) i.tech NF.	115
Figure 2-44: Loading-rate dependent Burgers model: LR vs vector components $x(i)$	116
Figure 2-45: Printed specimens just before the failure.....	117
Figure 2-46: Schematisation of multiple layers through Burgers models in series.....	120

Figure 2-47: Example of self-buckling failure prevision	121
Figure 2-48: Self-buckling failure prediction: (a) i.tech N and (b) i.tech NF.	122
Figure 2-49: Self-buckling failure domain for i.tech N and i.tech NF.	123
Figure 2-50: Burgers equivalent stiffness vs time curves obtained simulating material with different $EM(t = 0)$	124
Figure 2-51: Buildability domains based on the Master Curves plotted in Figure 2-50	124
Figure 3-1: Prisms for material tests cut from the specimens: (a) illustration of three prisms cut out of one specimen (exemplary for the parallel printing configuration); (b) testing set up ("EN 196-1" 2016).....	136
Figure 3-2: Stress-strain relationship of the steel bar.....	136
Figure 3-3: 3D concrete printing setups including the pumping system: (a) ETHZ; (b) UniNa	138
Figure 3-4: Specimen preparation for the parallel printing configuration with reinforcing bars: (a) Placement of the formwork; (b) Printing of the first 10 cm and placement of the reinforcing bars; (c) Printing of the remaining 10 cm and cutting of the specimens and cutting.	139
Figure 3-5: Printing path of the various configurations: (a) parallel printing path; (b) perpendicular printing path.....	140
Figure 3-6: Images from the production of the samples: (a) Printing of specimens with reinforcing bars with the perpendicular configuration; (b) Printing of specimens with reinforcing bars with the parallel configuration.	140
Figure 3-7: Testing setup for the pull-out tests with reinforcing bars: (a) Testing setup schemes (Top: ETHZ, Bottom: UniNa); (b) Image of the test setup at ETHZ; (c) Image of the test setup at UniNa.	141
Figure 3-8: Bar plot showing all max stresses of all tests next to each other	142
Figure 3-9: Pull-out behaviour: (a) Cast specimens; (b) 3D printed specimens with the perpendicular configuration; (c) 3D printed specimens with the parallel configuration.	144

Figure 3-10: Sections through the reinforcing bar in untested specimens (top: parallel configuration; bottom: perpendicular configuration): (a) UniNa; (b) ETHZ.....	146
Figure 3-11: Sections through the reinforcing bar in tested specimens(perpendicular configuration): (a) UniNa; (b) ETHZ.	146
Figure 3-12: Analytical [92] vs experimental bond stress-slip relationship: (a) UniNa and (b) ETHZ.	147
Figure 3-13: Experimental correlations between compressive and bond strength and estimated values from the codes [97].	149
Figure 4-1: Beam domain: representation of the mesh.	155
Figure 4-2: Examples of Bezier curves: a) linear; b) quadratic; c) cubic. End-points are denoted as red squares, while control points are blue circles.	157
Figure 4-3: General depiction of the solution framework [109]	158
Figure 4-4: Simply-supported reference beam.....	158
Figure 4-5: Bezier curves solution and printing path definition for (a) i.tech N and (b) i.tech NF.	160
Figure 4-6: Principal stress in the optimised solution (a) i.tech N and (b) i.tech NF.....	160
Figure 4-7: Printing session for the production of the specimen NF_01 and NF_02.....	161
Figure 4-8: Point cloud acquisition and comparison with the Bezier parametric curves (specimen N_01).....	161
Figure 4-9: Example of the geometrical imperfection in the 3D printed elements.....	162
Figure 4-10: Steel reinforcement detailing (a) NR_01, (b) NR_02, (c) NFR_01 and (d) NFR_02.....	165
Figure 4-11: Testing set-up and instrumentation: (a) not reinforced and (b) reinforced beam with (c) the support details.	167
Figure 4-12: Force vs Deflection curves.	167

Figure 4-13: Not reinforced beam failure mechanisms: (a) picture before and after failure (specimen N_02) and (b) schematic representation of the failure mechanism..... 169

Figure 4-14: Pictures of the beams during the test execution: (a) NR_01, (b) NR_02, (c) NFR_01 and (d) NFR_02..... 170

Figure 4-15: Typical mechanical response of 3DCP reinforced optimised beam 171

Figure 4-16: Beams after test: (a) NR_01, (b) NR_02, (c) NFR_01 and (d) NFR_02..... 173

Figure 4-17: Percentage angle variation at Joint A and K..... 174

Figure 4-18: M-N resistant domain for (a) NR_01, (b) NR_02, (c) NFR_01 and (d) NFR_02. 176

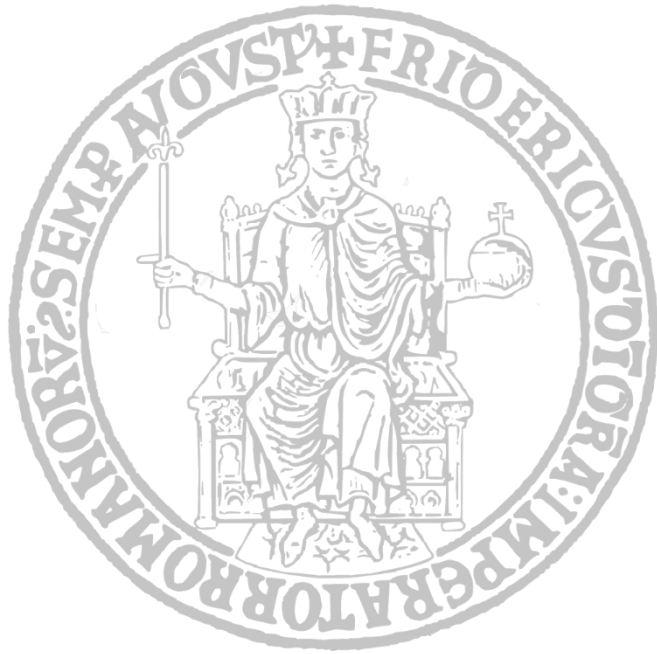
Figure 4-19: Stress state in concrete and steel bar between two consecutive cracks..... 177

Figure 4-20: Comparison in bearing capacity between experimentally 3DCP beams (i.tech N and i.tech NF) and traditional cast beams (designed according to [NTC2018])..... 179



List of Tables

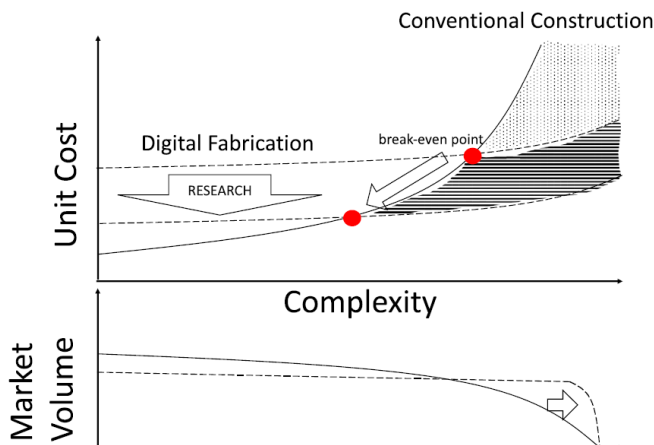
Table 2-1 Test matrix UUCT	53
Table 2-2 Printing parameters adopted.	56
Table 2-3 Influence of concrete ages (UniNa mortar)	58
Table 2-4 Influence of printing conditions. (UniNa mortar).....	62
Table 2-5 Influence of specimen preparation. (UniNa mortar).....	63
Table 2-6 Influence of displacement rate. (UniNa mortar)	65
Table 2-7: Test matrix.	93
Table 2-8: Testing parameters.....	105
Table 2-9: Burgers parameters calibrated at t=0min	111
Table 2-10: Solution of vector \boldsymbol{x} as a function of the stress rate.....	115
Table 2-11: Buildability test matrix and results	117
Table 3-1: Test matrix	133
Table 3-2: Overview of the mechanical characterisation at 28 days of the two mortars.....	135
Table 3-3: Overview of pull-out testing results.....	142
Table 3-4: Results of the flexural strength of the prisms cut from the specimens. f _{ct,fl} : Tensile strength of the concrete determined with flexural tests, f _c : compressive strength of the concrete	150
Table 4-1: Results of 3-points bending test performed on printed specimens	168



Overview

The thesis work focuses on implementing 3D Concrete Printing (3DCP) [1, 2] to fabricate reinforced concrete structures. 3DCP belongs to the broader and recent Digital Fabrication with Concrete (DFC) technology, representing one of the most widespread methods. DFC identifies the automated manufacturing techniques emerging in the construction field of structural and non-structural products without using traditional formworks [1]. In recent years, advances in computational design tools and industrial automation allowed the realisation of construction projects with high complexity and level of digitalisation by using DFC techniques [2–4].

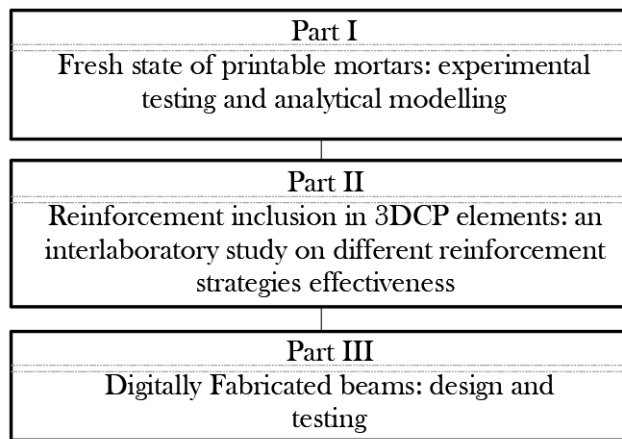
In conventional construction, the unit cost of a component increases with its complexity since it is challenging to produce it economically using one-time-use formworks. As schematically shown in the following figure, digital fabrication becomes more competitive as the complexity increases. In this sense, scientific research helps to shift the break-even point farther to the left, reducing the unit cost for digital fabrication [5].



*Top: unit cost vs complexity for conventional construction and digital fabrication
Bottom: market volume vs complexity. [5]*

Briefly, 3DCP technology consists of concrete layer (or filament) continuous extrusion through a nozzle attached to a robotic system (e.g., robotic arm, gantry system). Then, the concrete filament is deposited at the fresh state following a pre-defined printing path which reproduces the target geometry. If, on the one hand, this innovation could bring advantages in terms of construction time, cost, high-quality control and design flexibility [6], on the other hand, there are many unresolved and interesting new challenges to be faced [5]. Indeed, emerging research areas take on a new dimension and require attention due to the field's novelty. The doctoral research activities focused on different aspects of such technology. The first faced topic was the investigation and modelling of the behaviour of printable mortars at the fresh state. Particular attention was paid to testing procedures and experimental methods for the early age behaviour investigation to obtain the material properties and their evolution with the resting time. These properties are necessary for analytical and numerical modelling purposes, intending to know the mechanical response of the printed object in terms of deformation and to avoid a premature collapse during the printing process. In a second step, the hardened properties of 3D printed elements were studied. In particular, the investigation was focused on the effectiveness of the steel reinforcement strategy in 3D printed structural elements. As a last phase of the doctoral research, a numerical-experimental methodological approach was proposed to produce topology optimised reinforced concrete beams characterized by lightweight and proper structural properties. Most of the experimental studies herein presented were carried out in collaboration with the industrial partner Italcementi. Indeed, the printable mortars developed by Italcementi were used for printing applications, and part of their experimental characterisation at the fresh state was performed at the Innovation Laboratory (i.lab) in Bergamo, Italy. Furthermore, the collaboration with the University of Pavia allowed studying the mechanical response of the printable mortar developed at the University of Naples Federico II, for comparison purposes. With this latter cementitious formulation, many preliminary investigations permitted to define an adequate testing procedure for

fresh printable mortars. Since there are not yet standardised assessment procedures in the 3DCP production, the entire printing process and, consequently, the quality of the digitally fabricated elements are strongly influenced by the printing setup and material. Interlaboratory studies could help in such sense, allowing the comparison between different printing modalities and corresponding outcomes. In this regard, an interlaboratory study with the foreign university ETH Zurich was conducted through an exchange with the doctoral student working in the same field. An identical experimental campaign was carried out by the two students (Laura Esposito worked at ETHZ, while the foreign student worked at UniNa) to investigate the effectiveness of two alternative reinforcement types in 3DCP elements and the influence of different printing setups and materials on the steel-concrete bond. Based on the overall description above, the following work presents and discusses the main outcomes of the studies carried out during the three years and related to different topics in the 3DCP sector. In detail, the scientific research can be divided into three main interconnected parts.



A brief overview of Digital Fabrication and 3D-printing technologies is presented in *Chapter 1* to show the benefits and limitations of such a process, with particular emphasis on the topics faced in the thesis.

Chapter 2 (addressing *Part I* of the scheme above) discusses the results of experimental tests on early-age cementitious materials adequately developed for 3D printing applications. The critical aspects related to the determination of the early-age properties in the compressive state and their evolution with the material hardening will be faced in this chapter. Since the printing process is a transient condition, the time evolution of the printable material's physical and mechanical properties should be carefully considered. Furthermore, experimental data related to fresh-state characterisation can be used to calibrate analytical models able to predict the mechanical response of elements during the printing process (e.g., deformations, premature collapse, stability, buildability).

Chapter 3 (addressing *Part II* of the scheme above) deals with the result of an interlaboratory study on the incorporation of steel reinforcement into 3DCP concrete elements. In particular, the research goal is to understand the feasibility of including steel reinforcement into printed layers (i.e. small-diameter bar). The activity was carried out in collaboration with the foreign ETHZ university to investigate the influence of different printing setups and materials on the steel-concrete bond.

As a conclusive part of the research activities, *Chapter 4* (addressing *Part II* of the scheme above) describes the design and testing of a topology optimised digitally fabricated concrete beams, including also the reinforcement strategy developed and assessed in Chapter 3. In particular, topology optimised beams (designed with the approach developed within the same research group by Pastore et al. 2020) were produced with and without steel reinforcement to verify the solution's feasibility and investigate their load-bearing capacity, along with the definition of proper analytical models useful to interpret the structural behaviour.

1. Digital fabrication with concrete: main characteristics

Concrete is the most widespread building material commonly used in engineering constructions due to its helpful characteristics: general availability, broad applicability, relative ease of processing and handling, and ability to go from a fluid state, where it can fill a mould, to a solid-state, where it can then bear a structural load [5]. However, the construction sector requires a deep transformation to reduce environmental impacts and productivity. As a potential solution, adopting Industry 4.0 technologies in construction promises to enhance the sector's sustainability [7] [8]. Indeed, Digital Fabrication with Concrete (DFC) emerges in the construction industry, intending to optimise and automatise production processes, using digital data to drive manufacturing equipment towards the realization of concrete products. The resulting workflow improves productivity, efficiency, and manufacturing flexibility, positively impacting sustainability. Figure 1-1 shows the RILEM process classification framework, which can be applied (but not limited) to DFC technologies [9].

Different digital fabrication technologies can be grouped based on [5, 9, 10]:

- *extrusion process* in which concrete is automatically placed layer-by-layer through a moving nozzle, following a predefined digital path reproduced by cartesian gantry, robotic, crane, or cable robot systems [11–14]
- *formwork printing* in which concrete or other materials are used to fill a digitally fabricated formwork [15]
- use of *temporary supports* which are digitally designed against applied loads, fabricated, and then, subsequently concreted [16];
- *slipforming* consisting of a vertically moving formwork in which concrete is placed in the fluid state and hardens in a controlled manner;

in this way, it is possible to fabricate variable cross-sectional area structures (e.g. the smart dynamic casting system [3]);

- *particle bed 3D printing* (also known as ‘selective binding’ or ‘binder jetting’), which is based on the selective and automated deposition of a binder into a particles layer [17]

The first of the above methods is the concrete extrusion, or 3D Concrete Printing (3DCP) [11, 18], which belongs to Additive Manufacturing (AM) technologies of DFC (see Figure 1-1) and consists of concrete layer extrusion through a nozzle attached to a robotic system, such as a gantry system or robotic arm. The moving head of an automated printing apparatus typically extrudes a fresh and viscous cementitious mixture in the form of layers, following a digitalised path of a solid divided into several slices. Each slice has a pre-defined thickness and is repetitively placed on the previous layer until the end of the process, yielding the final concrete component.

The gantry style printers are relatively easy to scale up in size, but they are limited to vertical extrusion. The size of gantry printers currently in use varies from small versions to large scale printers that may be used to print entire building components [19]. An example of a large scale (i.e. $9\text{ m} \times 4.5\text{ m} \times 2.8\text{ m}$) four axis gantry robot was developed at Eindhoven University of Technology (Figure 1-2a).

On the contrary, robotic arms typically have a fixed dimension. Still, they face many complex tasks thanks to higher degrees of freedom. An example is the 6-axis robotic arm used at the University of Naples Federico II (also representing the system adopted in the printing session presented in this thesis) represented in Figure 1-2b.

In both cases, the printer is equipped with one or more devices to mix the mortar and pump it up to the extrusion head.

3DCP offers the advantages of eliminating the necessity of formworks to produce structural and non-structural elements with high shape flexibility, high-

quality control, reduced construction time and waste. For such reason, the number of projects and applications quickly grows, as visible in the chart proposed in [14].

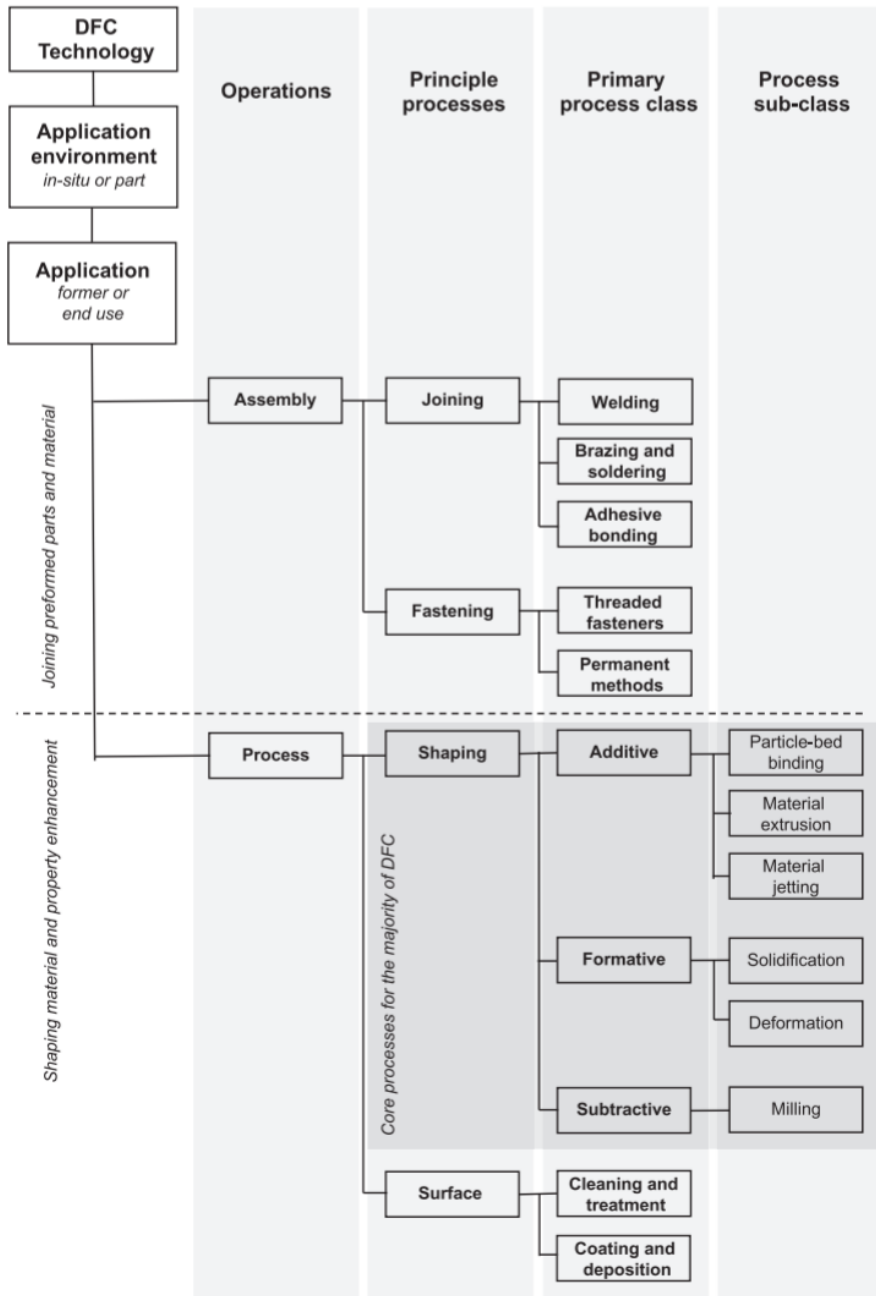


Figure 1-1: The RILEM process classification framework for DFC technologies [9].

(a)



(b)



Figure 1-2: Example of (a) 4 axis gantry system (Eindhoven, [20]) and (b) 6-axis robotic arm (Naples).

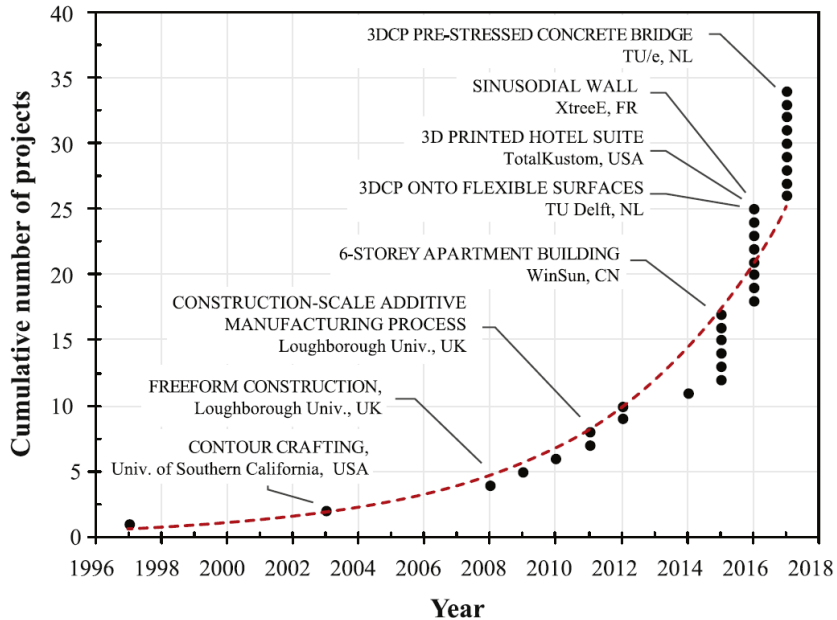


Figure 1-3: Number of projects realised with additive manufacturing (since the concept inception in 1997) [14].

1.1 Printable cement-based materials

Innovative cement-based materials are currently being developed to be employed in DFC techniques. Printable mortars behave as visco-plastic Bingham materials since they only flow when submitted to stresses higher than a critical threshold value called yield stress [21] (Figure 1-4).

The engineering challenges arising from such a process are manifold, and the primary requirements of cementitious materials for layered extrusion can be summarised as follows:

- Pumpability, which describes the ease with which the fresh mixture is transported from the pump to the extrusion nozzle [14];
- Extrudability, which is the ability to extrude the mixture through a nozzle without major cross-sectional deformation and with an acceptable degree of splitting/tearing of the filament [14];

- Buildability is the extruded material's ability to retain its geometry (shape and size) under sustained and increasing loads [22].

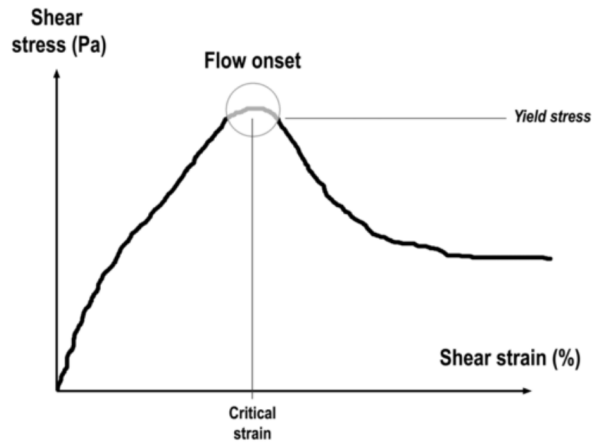


Figure 1-4: Shear stress as a function of shear strain [21].

Within this framework, the design and control of the overall printing process primarily consist of optimising fresh concrete compatible with the automated printing system [18, 23]. Specific rheological properties are required for concrete to be printed (pumpability and extrudability requirements), whereas the physical-mechanical properties are essential for buildability and filament shape retention after extrusion [24]. In this respect, the thixotropy is a fundamental property since it allows having low yield stress during the pumping and extrusion (i.e. when the material is subject to external forces) and higher yield stress just after the exit from the nozzle (i.e. once external forces come to zero) which should guarantee self-sustaining properties during the layer-by-layer build-up. Another issue concerning the building rate: on the one hand, it should be high enough to ensure adequate bond strength between the layers; on the other, it must be low enough to deliver adequate buildability and prevent premature collapse (Figure 1-5). As the height of the concrete element increases during the printing process, so does the hydrostatic pressure [14]. Accordingly, as there is no rigid mould during the construction process, high compressive strength and stiffness are required: after the deposition of fresh

material, each concrete layer must be able to bear its weight and that of the layers above it.

As a result, comprehensive knowledge of employed materials' rheological and mechanical behaviour allows predicting their response during the digital fabrication process: the designer can optimise the material performances, saving time and cost.



Figure 1-5: Examples of collapse during printing: (a) empirical buildability test geometry (from [14]) and (b) failure of a hollow cylinder (from [25]).

1.2 Reinforcement strategies in 3DCP and case studies

3DCP offers the advantages of eliminating the necessity of formworks to produce structural and non-structural elements bringing several advantages. However, this technology must face some challenges, mainly linked to the limited knowledge in areas such as incorporating reinforcement in structural concrete members.

Cementitious materials have a brittle mechanical behaviour and low tensile strength. Therefore, these materials are traditionally combined with reinforcement to improve ductility and produce load-bearing structures. However, for 3DCP, this inclusion of reinforcement is not straightforward due to the layered manufacturing process. The critical aspect with respect to the 3DCP technology is how to integrate reinforcement with minimum interference in the concrete shaping process [26]. Different reinforcement strategies for 3DCP technology were developed and explored in the available literature. A

brief review of such reinforcement strategies will follow. Please refer to available reviews for further details [1, 26–28]. Using *steel bars* to reinforce concrete structures is a standard construction method, and it was also employed in AM technology. For example, the straight walls of the 3D printed house [29] were reinforced by placing unbent bars into the still fresh concrete parallel to the printing plane and then covered by a subsequent layer of concrete (Figure 1-6a). The steel reinforcement was also prefabricated and welded (Figure 1-6b) to form the shape of the concrete in the 3-D printed office built in Dubai [30].



Figure 1-6: Reinforcement of 3DCP structures: placement of (a) straight reinforcement bars [29] and (b) steel bar truss in the print plane [30].

An alternative solution was suggested by Mechtcherine et al. [31]: it consists of using the Wire Arc Additive Manufacturing (WAAM) method in which reinforcing elements are built up in a drop-wise manner enabling a maximum geometric flexibility process. Tensile tests confirmed load-bearing and ductile behaviour comparable to conventional reinforced concrete. However, some hurdles of this kind of reinforcement concern the different printing speeds of the concrete and steel, the high temperatures generated during the steel printing and the elevated costs.



Figure 1-7: External reinforcement system with tightened bars [32]

Another reinforcement strategy example is the *external reinforcement* of the 3D-printed beam fabricated by the University of Naples "Federico II" [32] (Figure 1-7). The approach consisted of partitioning a reinforced concrete member into different segments separately printed and then assembled and reinforced using tightened steel bars. This approach facilitates the production of structurally optimised reinforced concrete elements, saving material usage and, at the same time, fabricating lighter structures. However, this solution brings some issues, such as the environmental degradation of the external bars and fire resistance.

3DCP technology could also produce *lost formwork* for conventional reinforced concrete. An example of this approach is presented in [15].

In 2017 a novel reinforcement with *metal cable* was presented at TU Eindhoven for 3DCP applications [33].



Figure 1-8: (a) Entrained cable into the concrete filament [34] and (b) bicycle bridge developed at the TU/e [35]

A rotating spool feeding the reinforcement into the printing head was employed to place these cables directly during printing, as shown in Figure 1-8a, resulting in a single automated manufacturing process. This kind of reinforcement is effective in only one direction, i.e. longitudinal to the filament. Steel cable was used as secondary reinforcement in the pedestrian and bicycle bridge developed at the Eindhoven University of Technology (TU/e) [35], which was placed in Gemert, Netherland (Figure 1-8b). This bridge is a large-scale application of *post-tension cables* and consists of printed elements, rotated 90° after printing, and then pressed together by post-tensioned prestressing tendons. In this way, 3DCP elements only work in compression, and no additional passive reinforcement in that direction is required [11]. Another example of a post-tensioned structure is the digital designed and manufactured concrete girder produced at Ghent University [36]. The beam was produced in separated segments subsequently assembled with post-tension cables running through the whole element, as shown in Figure 1-9.



Figure 1-9: 3D printing of a post-tensioned concrete beam designed by topology optimisation – Ghent University [36]

The final beam shape derives from the topology optimisation of a simply-supported beam subjected to a uniform load. In particular, the design of the 3DCP beam was based on the novel approach for the design of prestressed beams proposed by Amir and Shakour [37], adapted by Vantuyghem et al. [36] for three-dimensional setting and material properties. This case study

demonstrated that post-tensioning combined with the topology optimised geometry alleviated the difficulty of introducing steel reinforcement in 3D-printed concrete.

A similar TO approach was adopted for the reduced scale pedestrian bridge described in Kinomura et al. 2020 [38], resulting in a bridge structure consisting of 44 segments with different complex shapes, which were printed separately and unified through prestressed external reinforcement. The topology optimised shape obtained from the analysis was modified in a final shape taking into consideration workability and safety.

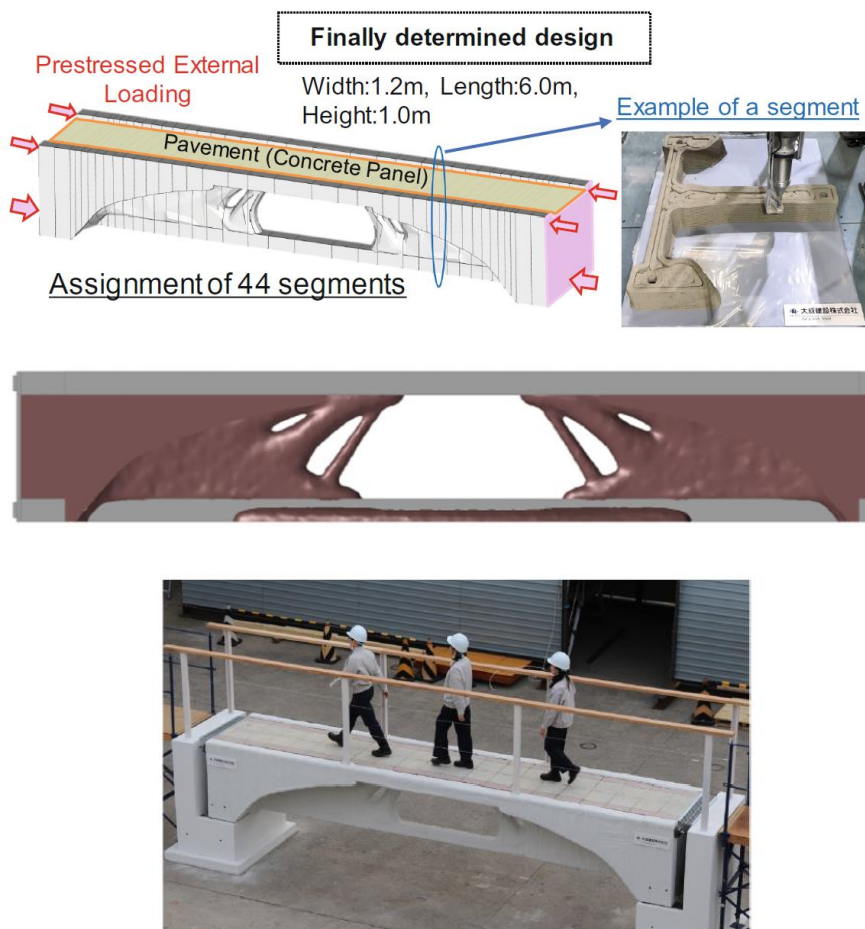


Figure 1-10: 3D Printed prestressed pedestrian bridge designed through topology optimisation approach (Kinomura et al. 2020 [38]).

From these examples, it appears that the effectiveness of the adopted TO strategy has to be balanced/adjusted with post-processing operations, such as concrete segment separation/joints, grouting, segment interface imperfections, etc.

2. Early age behaviour of 3D printable mortars

Innovative cement-based materials are currently being developed to meet the challenges of emerging DF techniques. Since no formworks sustain the fresh mortar during the production, the early-age behaviour (i.e. mechanical and rheological properties at fresh state) becomes more critical to ensure a successful process. Printable mortars behave as visco-plastic Bingham materials since they only flow when the shear stress is higher than the material yield stress. For such reason, the printability requirements are strictly correlated to the yield stress value. For example, referring to the buildability, many research studies in literature proposed strength-based failure criteria strictly correlated with the rheologic material properties. Perrot et al. [39] proposed a criterion based on a comparison of the vertical stress acting on the first printed layer to the critical stress linked to the material's yield stress with the aim to predict the buildability performances of cementitious printable mortars. The bi-linear model proposed by Kruger [40] is also based on the static yield stress evolution as a function of resting time: the thixotropy model was developed based on a material's shear strength in its plastic state, which can be characterised with a rheometer.

As a results, comprehensive knowledge of employed materials' rheological and mechanical behaviour allows predicting their response during the digital fabrication process: the designer can optimise the material performances, saving time and cost.

Due to the complex material nature, different types of experimental tests are needed to fully understand the behaviour of printable mortars in the fresh state. Recent studies in the literature aimed to investigate the most appropriate testing procedures to characterise the physical and mechanical behaviour of such cement-based materials at the fresh state. The most classical experiments

include Uniaxial Unconfined Compression Test (UUCT) [20] and rheological measurements (to quantify pumpability and extrudability) such as Rotational Rheometer Tests (RRT) [21, 39, 40] or Penetration Tests (PT) [41, 42], even though ad-hoc procedures have also been developed as the squeeze flow test [39].

During the experimental characterisation, many variables are essential to obtain reliable testing results: dry component to water mixing modality, specimen preparation and size, adopted loading/displacement rate, measurement instrumentation, total testing time etc. Since the printing process is a transient condition, the time evolution of the printable material's physical and mechanical properties should be carefully taken into account in the testing setup. Printable mortars harden during the testing execution due to cement hydration; hence the correct choice of all testing parameters could depend on the material age. The difficulty is mainly linked to the complex response of early age printable mortars, characterised by a viscous plastic response like any other cementitious material [21]. Fresh concrete behaves as a viscous material, and its response could change with the applied loading rate (or displacement rate). At the same time, the loading rate (or displacement rate) determines the testing duration, and its value becomes fundamental to avoid the not-negligible material hardening during the test. For example, Wolfs et al. [43] adopted a displacement rate value in compression tests high enough to neglect thixotropic build-up effects.

Such experimental data are quickly growing in the literature, helping define the adequate testing procedure to characterise the cement-based material employed in AM.

This chapter is focused on the experimental characterisation of the early-age behaviour of printable mortars, paying particular attention to (i) the uniaxial compressive behaviour and the effect of the testing procedure, and (ii) the early-age viscoelasticity or creep effects.

To this aim, the changes in the mechanical response with the resting/waiting time of different cementitious mortar types were investigated. Note that all mortars investigated were designed for 3D printing technology.

The first mix was developed in-house at University of Naples Federico II (*UniNa* mortar). It is composed of sand (maximum particle size 4 mm), 0.5% in weight of 18 mm polypropylene fibres (added to prevent plastic shrinkage-cracking during the early curing stage and after the deposition process), low water/cement ratio ($w/c = 0.39$) and a polycarboxylate superplasticiser (SP = 0.10% in weight of cement) used to improve printability performances (i.e., pumpability and extrudability). The mortar's average cubic strength, R_{cm} , at 28 days was equal to 53.5 MPa with a standard deviation of 3.1 MPa [44]. The resulting material density was 2411 kg/m³.

Italcementi company supplied the second mix (*i.tech N* mortar). It is a ready-mix and high yield strength cementitious material. Polypropylene fibres were added to the mix to avoid shrinkage, resulting in a second formulation named *i.tech NF*.

The effect of testing methods on the uniaxial compressive behaviour characterisation was studied in collaboration with the University of Pavia. The experimental campaign consisting of Uniaxial Unconfined Compression Tests (UUCT) was preliminarily performed on the *UniNa* mortar type to define the reliable procedures for the specimen preparation and highlight the most critical issues in this specific field. The optimised UUCT testing method was employed to assess the uniaxial compressive response of the Italcementi mortars. Since the testing procedure was optimised, a large number of specimens was prepared and tested accordingly by introducing new process-related variables, i.e., varying the Aspect Ratio of the specimens and the Displacement Rate of the compression test.

The optimised UUCTs allowed obtaining the stress-strain relationship for different resting/waiting time values and, consequently, the time-dependent

evolution laws of the elastic modulus and compressive strength of the 3D printable mortars investigated.

The early age viscous behaviour of printable mortars was also investigated and reported in this chapter. An appropriate testing procedure was defined to study the early age creep behaviour and time dependency at the fresh state. To this aim, preliminary experimental compressive tests under constant load were carried out on the UniNa mortar, and the outcomes were employed to calibrate the analytical visco-elastic Burgers model suitably identified to take into account such peculiarities.

Finally, based on the outcomes of both the UUCT and creep test, an experimental method was developed to reproduce better the stress state history experienced by the cementitious layer during the step-wise printing process. The experimental outcomes of such a new experimental setup were used to calibrate the constitutive viscoelastic Burgers model used to predict printed mortars' overall buildability/stability in the layered extrusion process.

2.1 Uniaxial compressive behaviour

With a specific emphasis on the buildability requirement, it is clear that adequate knowledge of the compressive behaviour of the fresh material is necessary. Tall structures manufactured in a vertical orientation are potentially affected by early-age instability and modelling them either mechanically and analytically is of great interest to manufacturers and structural engineers [14]. In particular, knowledge of the time evolution of the constitutive behaviour of concrete under compression is essential to predict the stress/strain state of each layer and ensure the stability of the entire element during the printing process. The stress state within each filament layer depends not only on the externally applied load but also on the boundary conditions, i.e. the state of confinement, which is strongly linked to the aspect ratio of the filament during printing [40]. In order to achieve a complete characterisation of the cementitious mortar's constitutive behaviour (i.e., the stress-strain relationships) as a function of early

age, compressive tests must be carried out within a proper time-frame that ideally takes into account: (a) the time elapsed between the release of the material from the printing nozzle to the subsequent printing steps (short time-scale); and (b) the overall time needed for the production of the complete element (long time-scale). Unfortunately, there have been no standard procedures for compressive tests on early-age printable concrete samples until now. Therefore, an appropriate test framework is required for design and simulation purposes to improve what is known about the time/process-dependent mechanical behaviour of this material (e.g., finite element analyses).

In the available literature, research has been carried out on the early-age compression properties of printable concrete [20, 39, 43, 45–48], as well as on the hardened state (minimum test age of 24 hours) [49–52]; nevertheless, the latter, is, in practice rarely helpful in predicting the mechanical performance of the structural element during the printing process. However, to predict the buildability performances of cementitious printable mortars, Perrot et al. [39] proposed a strength-based failure criterion based on a comparison of the vertical stress acting on the first printed layer to the critical stress related to the plastic deformation linked to the material's yield stress. This model was validated using squeeze flow tests performed on very early-age concrete. In particular, to simulate the progressive loading characterising a layer-by-layer construction, the authors loaded a cylindrical sample (height of 35 mm, a diameter of 60 mm) by applying 1.5 N load increments (corresponding to the increasing weight of the layer-by-layer deposition). The time gap between the load increments was also varied to simulate different building rates (in the range of 1 to 6.2 m/h). However, while this test was helpful in detecting sample failure, no information was provided on the stress-strain relationships of the compressed layers. Kazemian et al. [47] investigated shape stability (also called shape retention or "green" strength) using two different testing methods: "layer settlement" and "cylinder stability". These assessed the compression behaviour of layered samples rather than the printable concrete material itself. In the

cylinder stability test, a cylindrical sample with a total height of 80 mm (composed of two 40-mm concrete layers) was loaded with 5.5 kg (4.77 kPa). Any possible change in height resulting from the self-weight and applied load was then measured and recorded for different concrete mixtures. As a result, no stress-strain relationships for the concrete used in the layers were reported for this test method.

Given the physical state of early-age printable mortars, possible testing standards could be adapted from those valid for soil or fresh concrete. However, in some cases, these may not be appropriate and completely new test methods are required. Key aspects that are still to be addressed include the representative sample size, testing equipment, loading/displacement rate, specimen preparation in the pouring procedure, material compaction, and measurement devices. These testing conditions must also be defined in relation to the main parameters of the printing process (printing facility, pumping system etc.), as well as the printable material's characteristics (curing rate, slump etc.).

In contrast to previous studies, constitutive laws related to early-age printable concrete were proposed by Wolfs et al. [20, 43]. In particular, a custom triaxial compressive test (TCT) was carried out on cylindrical concrete samples with a diameter of 25 mm and a height of 50 mm, according to ASTM D2850. The samples were not compacted during preparation and were then subjected to triaxial compression in displacement-controlled conditions and at distinct concrete ages (15, 30, 60 and 90 minutes). The 15 mm/min displacement rate (i.e., 30% strain/min) was fast enough to prevent the effects of thixotropic build-up/ageing during a single test. The TCT results related to an equal-to-zero confining pressure can be compared with those of uniaxial unconfined compressive tests (UUCTs) performed by the same authors [20, 43]. In particular, the UUCTs were carried out on cylindrical concrete samples with a diameter of 70 mm and a height of 140 mm, designed according to ASTM D2166). In contrast to previous testing campaigns, the preparation procedure

aimed to obtain a homogeneous sample and consisted of using steel cylindrical moulds lined with a thin sheet of Teflon in combination with compaction for 5 s on a 30 Hz vibration table. The same concrete age range ($t = 5, 15, 30, 60$ and 90 minutes) was adopted for the tests, as was the same displacement rate of 42 mm/min (i.e., 30% strain/min), enabling a proper comparison to be made with the TCTs in terms of the stress-strain relationships. The comparison of the two sets of test results (UUCT and TCT) highlighted discrepancies in terms of the strength and stiffness values, which were probably associated with the better compaction of the samples in the UUCTs, which had improved the concrete's mechanical properties. Indeed, the imperfection density is typically more significant in fresh concrete without compaction. Moreover, the impact of such imperfections is generally amplified for small specimens (i.e., TCT).

2.1.1 Effect of testing procedures

Given the above, it appears that the need to define standard testing procedures is indisputable. However, establishing universal criteria for printable concrete would require a large number of relevant studies to encompass the performance of the different printing mixtures used in DF projects. The mechanical parameters (e.g., compressive stress-strain laws, stiffness, yield stress) of printable mortar in the unlayered state represent the starting point for implementing predictive models that simulate the printing process and any related mechanical phenomena/failures. Consequently, the aim of this chapter is to show sensitivity analyses on the various mechanical testing parameters towards standardised test methods for 3DCP and, based on the results, evaluate their effects on predictive buildability models. In particular, the following aspects are considered:

- *Materials and sample preparation:* during an automated printing process, it is possible to experience variations in the compaction/workability of the extruded material due to random changes in the water content, the different conditions of the stocked dry material, and human error. Furthermore, as the material is in an early-age state (i.e., fresh/viscous) when it emerges

from the printing nozzle, there are practical difficulties in simulating these conditions during the specimen preparation in the laboratory (i.e., pouring, compaction and demoulding).

- *Compressive test setup*: to run the experiments properly, representative samples must be subjected to compression load/displacement. As printable cement-based materials behave roughly like visco-plastic Bingham materials [21], their mechanical response is greatly affected by the sample size and loading rate, which could significantly impact the measured strength.
- *Evolution over time of the compression stress-strain*: the compressive strength and stiffness of early-age concrete inevitably change during the printing process; as its mechanical properties alter quickly, each layer behaves differently, especially for high-value cycle-times (i.e., the time required to complete one build layer) [14].

The outcomes of UUCTs performed on a reference printable cementitious material (i.e., UniNa mortar) are compared with the results achieved by varying: (a) the amount of superplasticiser (SP) used (in percentage terms); (b) the sample preparation procedure; and (c) the displacement rate adopted during the test. Furthermore, the UUCTs were examined at distinct concrete ages ($t = 0, 15, 30$ and 60 minutes) to define the evolution of the corresponding constitutive stress-strain laws over time. In detail, $t=0$ was the shortest time possible considering the specimen preparation procedure, which includes the mould filling, slightly compaction, demolding and placing of the sample in the test setup, which took approximately 3 min. Finally, the overall test outcomes were implemented in an available stability model to identify the effect of the testing variability on the maximum printed stable height of the concrete elements.

2.1.1.1 Methodological approach

Starting with the reference UniNa mix (described in the introduction of Chapter 2), variations in the SP percentage were considered to study changes in the

material's consistency during the printing process or sample preparation. The following conditions were examined: (a) the absence of superplasticiser (0.00% - SP0.00 ending in the acronym of the sample series), which replicates low sample compaction or a very dry pumped concrete material; and (b) 0.15% SP (SP0.15 ending in the acronym of the sample series), replicating the further manipulation of the specimen to obtain a homogeneous or compacted concrete material.

Compression tests were performed on cylindrical samples with a diameter (d) of 60mm and a height (h) of 120mm. This geometry was chosen to exclude size effects due to particle size distribution and ensure diagonal shear failure ($h/d=2$). Larger specimens might not correctly represent the dimensional scale of the concrete during the printing process (in which layers are in the order of centimetres), while thinner specimens could be affected by squeezing or local deformations induced by loading plates. In the mixing procedure, the fine aggregate, cement and filler were initially mixed for 60 seconds at a low speed (140 rpm). Subsequently, these dry components were mixed with polypropylene fibres (140 rpm 30 seconds). Water was then added, and mixing retook place for 60 seconds (140 rpm). Finally, a poly-carboxylic SP was added gradually, mixing for 120 seconds at high speed (285 rpm). In general, experimental tests on conventional cast concrete cannot be executed until the first setting has occurred (approximately 24 hours). However, the layered extrusion technique is a process in which subsequent fresh concrete layers are stacked on top of each other.

Consequently, the first challenge during an experimental test is linked to the very early age of the material to be tested; there are inevitably more difficulties during the preparation of the specimen in such cases (i.e., casting, compaction and demoulding). Indeed, it is challenging to extract specimens from the moulds even after the first setting without affecting their integrity. A plastic 3D-printed openable mould (see Figure 2-1) was designed to overcome this

issue. As a temporary mould was used, part of the gravity-induced stresses was sustained by this support through interface adhesion.

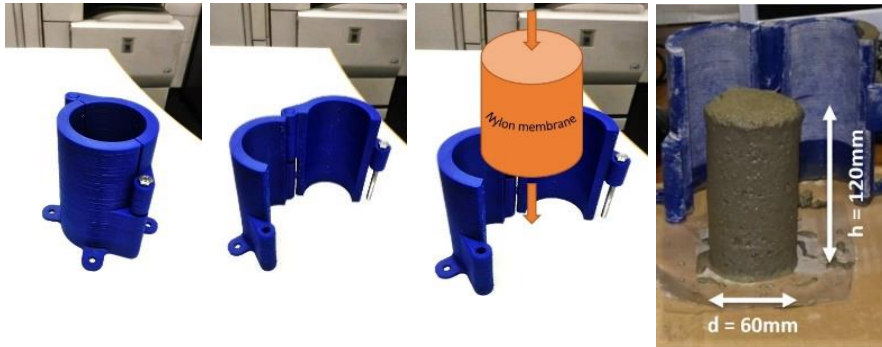


Figure 2-1: 3D-printed openable mould: closed, open, positioning of the nylon membrane, example of a prepared sample.

However, after demoulding, the sample could have been affected by residual stresses, deformations under self-weight and imperfections. As a consequence, improvements in sample preparation were achieved by using an internal nylon membrane (interposed between the mould and the later surface of the specimen) that effectively reduced the interface friction; in addition, to completely eliminate the effect self-weight due to 120 mm sample height, a pre-load of 2kPa was applied on each sample of the series. After the cast procedure, the sample was demoulded and the membrane removed; in this way, the curing took place in the same condition for both the sample cast with the membrane and the one cast without it. The impact of specimen preparation was also investigated by comparing the results obtained with (M in the sample series acronym) or without (NM in the acronym of the sample series) the membrane during the sample preparation.

Cylindrical specimens were tested using an MTS electromechanical Universal Testing Machine with a 10 kN capacity in a displacement-control condition at room temperature $T \approx 22^\circ\text{C}$. The tests were performed up to a vertical strain of 12%, i.e., 15 mm displacement. As no physical measurement of a sample was possible without altering it (e.g., attaching extensometer or strain gauges), the stresses and strains were deduced from force-displacement data obtained from

the testing machine. Young's modulus was computed as the secant modulus from 0% to 2% strains. However, since this interval might change as a function of the material printing characteristics (in [20] this range is 0-5% strain), it is necessary to establish a reliable strategy to identify allowable ranges for elastic modulus measurement. Indeed, (i) tests are generally carried out in a very low load level regime (especially for very early age), in which slight material variations (e.g., mix design, environmental conditions) may determine pronounced stiffness variations, (ii) Young's modulus values may depend on the specific method adopted for the strain estimation. In order to determine the stress-strain law's evolution over time, the compressive tests were carried out at distinct concrete ages ($t = 0, 15, 30$ and 60 minutes) with a displacement rate (DR) of 3 mm/min . As the mechanical properties of concrete and other cementitious composites are known to be rate-sensitive in the hardened and fresh state, while strength and other properties improve as the strain rate increases [53], the compressive tests were also performed with a higher DR value ($30 \text{ mm/min} = \text{one order of magnitude higher}$). Furthermore, the tests at $\text{DR} = 30 \text{ mm/min}$ were carried out only for the reference mix, i.e., REF-SP0.10-M, in order to investigate only one variability at a time; this rate was still within the displacement rate range that is currently used to test printable mortars [20, 43].

The UUCTs were performed by varying: (a) the concrete age ($t=0, 15, 30$ and 60 minutes); (b) the percentage of SP added to the mix ($0.00, 0.10$ and 0.15% in weight of cement); (c) the sample casting procedure (with or without the membrane); and (d) the displacement rate (3 mm/min and 30 mm/min). Five samples were prepared and tested for each specimen series. Table 2-1 summarises the experimental tests concerning the six series of samples. Each specimen set is identified by the acronym "SP_{xx}-yM-DR_{zz}", where: "SP_{xx}" represents the percentage of SP added (SP0.00, SP0.10 and SP0.15); "yM" indicates whether the membrane was or was not used during the casting (M and NM, respectively); and "DR_{zz}" is the value of the displacement rate in mm/min

(DR3 and DR30). The reference printable mix is indicated by the acronym "REF-SP0.10-M-DR3".

Table 2-1 Test matrix UUCT

Variables	Uniaxial Unconfined Compression Test					
Acronym	REF-SP0.10-M-DR3	SP0.00-M-DR3	SP0.15-M-DR3	SP0.00-NM-DR3	SP0.10-NM-DR3	SP0.10-M-DR30
1. Age [min]	0, 15, 30, 60	0, 15, 30, 60	0, 15, 30, 60	0, 15, 30, 60	0, 15, 30, 60	0, 15, 30, 60
2. Superplasticizer [%]	0.1	0.0	0.15	0.0	0.1	0.1
3. Membrane	Yes	Yes	Yes	No	No	Yes
4. Displacement rate [mm/min]	3.0	3.0	3.0	3.0	3.0	30.0
Samples per set	5	5	5	5	5	5
Tot. samples	20	20	20	20	20	20

As the concrete material was mainly in the early-age state throughout the printing process, implying low strength and stiffness values, stability checks of the structural build-up had to be performed as a function of the increasing height of the printed element and the building rate. The stability checks included: (i) a compressive plastic yielding check and (ii) a self-buckling instability check.

The structural performance of early-age concrete and, in turn, the overall printed element stability strictly depends on the temporal evolution of some of the mechanical parameters derived from experimental characterisations. The UUCT experimental results were then used to determine the stress-strain relationships for the different concrete ages, providing the evolution over time of the compressive strength $\sigma_{c,max}(t)$ and the Young's Modulus $E(t)$. The continuous time-variation compressive strength and stiffness laws were obtained through linear regression of the data related to each tested sample series. Based on these laws ($\sigma_{c,max}(t)$ and $E(t)$), an analytical model was used to predict the compressive failure of the first layer or the self-buckling failure of the printed element due to its weight during the printing process. It was made the hypothesis that each layer would be instantaneously stacked. The interval time between the deposition of one layer and then the next, T_{print} , (i.e., the

cycle-time) subsequently depended on the layer height and building rate, as follows:

$$T_{print} = \frac{h_{layer}}{B_R}$$

Equation 2-1

The success of the printing process, in general, is strongly correlated to the building rate B_R [mm/min], with the time variable between the subsequent printed layers being fundamental [39]. In our study, the maximum number of layers that could be stacked before collapsing due to the compressive failure of the first layer was obtained by comparing the vertical stress in the first layer $\sigma_v(t)$ (depending on the weight of the subsequent layers) and its developed strength $\sigma_{c,max}(t)$:

$$\sigma_v(t) = H(t)\rho g \geq \sigma_{c,max}(t)$$

Equation 2-2

where: H is the total height of the printed element depending on time (increasing by discrete thickness values corresponding to the single-layer height); ρ is the material's density; and $\sigma_{c,max}(t)$ is the linear law obtained from experimental data. It should be pointed out that, depending on the testing procedure used and, in particular, on the time $t=0$ condition adopted, a bi-linear increase in strength could also be observed after the material extrusion [54]. The elastic self-buckling failure check was performed according to Greenhill's equation [55] [Equation 2-3]: a free-standing vertical column buckles under its weight if its height exceeds the following critical value:

$$H_{crit}(t) = \left(\frac{7.83 \cdot E(t) I_{min}}{\rho g A} \right)^{\frac{1}{3}}$$

Equation 2-3

where: $E(t)$ is the experimental time-evolution law of the printable concrete elastic modulus; I_{min} is the minimum moment of inertia (depending on the shape of the printed element); A is the cross-section area; and ρ is the density of

the material. A similar equation was used by [21] to predict the loss of stability of linear walls obtained with 3DCP technology. Based on the simple geometry of one linear meter of wall wide, the previous expression becomes:

$$H_{crit}(t) \approx \left(0.65 \cdot \frac{E(t)\delta^2}{\rho g}\right)^{\frac{1}{3}}$$

Equation 2-4

with the minimum moment of inertia equal to $I_{min} = \delta^3/12$ and the cross-section area to $A = \delta$. The self-buckling failure could be predicted approximately by comparing the printed element height and the critical height (according to Greenhill's) as the printing time increases. The stability check was also conducted using the comparison between the elastic modulus and its critical value $E_{crit}(t)$:

$$E(t) \leq E_{crit}(t) \approx 0.65^{-1} \cdot \frac{H^3(t)\rho g}{\delta^2}$$

Equation 2-5

Another model has also been considered to provide a more reliable interpretation of the results derived from testing procedure variability. In particular, the mechanistic model developed by Suiker [56] to determine the mechanical performance of straight wall structures in the 3D printing process is adopted for this purpose. Suiker provided a useful graphical tool to predict the two main failure mechanisms, the elastic buckling and the plastic collapse, by considering the most relevant process parameters. The failure mechanism maps are available in Suiker [56] for different wall types, i.e., for different boundary conditions (free, simply supported and fully clamped wall). Hence, the two above described methods for the failure prediction, i.e. Equation 2-2 and Equation 2-5, and the Suiker failure maps, were implemented for a straight free wall geometry, adopting the results obtained from each test condition examined (see the summary of the test matrix Table 2-1). Such results are the continuous time-variation compressive yield strength and stiffness laws obtained through linear regression of the data related to each tested sample series. In this way, it was possible to study the impact of the specific testing

procedure on the predictions of the structural performance of the element during the printing process. Table 2-2 summarises the printing parameters adopted for the numerical implementation of the failure criterion.

Table 2-2 Printing parameters adopted.

Layer width δ [m]	Layer height h [m]	Building rate [m/h]	Density [kg/m^3]
0.04	0.01	2.00	2411

2.1.1.2 Results and discussion

The experimental test results are described in this section in relation to the stress-strain curves. In particular, the data are grouped and compared as a function of the concrete age to study the impact of the material's consistency, the sample preparation, and the displacement rate. In the following stress-strain diagrams, the curve related to each sample is reported in grey and the average curve in black. As the samples were not perfectly flat, the force of the loading cell began to stabilise around 5 N, meaning that the stress-strain curves started from a stabilised value of 2 kPa (2 kPa is the stress at 0% strain). As previously mentioned, the time $t = 0$ was the shortest time possible, taking into account the specimen preparation procedure, which took approximately 3 min. As a result, this had possibly led to a slight overestimation of the mechanical properties in the early minutes in which thixotropic build-up takes place. The discussion of the results is structured as follows: (a) the force-displacement and stress-strain curves related to the reference mix are described and compared for each curing-time value; (b) the impact of the material's consistency and how the sample was prepared are examined; and (c) the results achieved at different displacement rates are compared.

Influence of the concrete age

Figure 2-2 contains the experimental force-displacement curves for the reference concrete-printable mix (five specimens), while Figure 2-3 portrays the corresponding comparison between the average stress-strain curves related to distinct concrete ages.

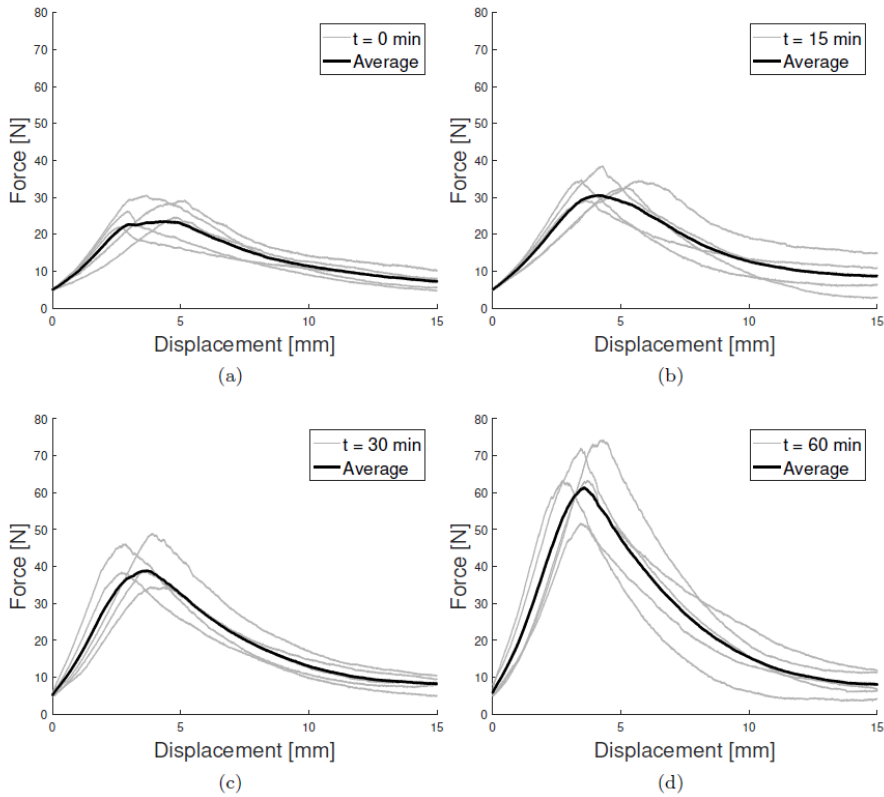


Figure 2-2: Compression tests - REF-SP0.10-M-DR3. Average and individual results at different times : (a) 0 minutes, (b) 15 minutes, (c) 30minutes, (d) 60 minutes. (UniNa mortar)

The compressive stress reached a peak value (i.e., compressive strength $\sigma_{c,max}$) after initial linear-elastic behaviour (the strain limit of the elastic range was about 2% for all the concrete ages), and then fell back again along the softening branch. It can be seen that there was a transition from plastic to brittle behaviour as the resting time increased, depending on lateral deformations; as fresh concrete is almost visco-plastic, lateral deformations are hampered by relatively low stiffness (which increases with the curing time), causing failure by bulging. In contrast, the older samples expanded less and had a more definite failure plane evolution. The curing time increased the strength and stiffness values: the material became stronger (higher yield stress) and more rigid (higher elastic modulus). The augmented macroscopic elastic modulus and yield stress increased from an increase in the size and number of hydrate-bridges between

the percolated cement particles. This phase is referred to as structuration [21]. In detail, the average compressive strength was 8.80 kPa at 0 minutes, rising to 22.48 kPa at 60 minutes; meanwhile, the Young's modulus increased from 210 kPa at 0 minutes to 607 kPa at 60 minutes (see Table 2-3). The overall percentage increases with respect to the concrete age from 0 to 60 minutes were 156% and 189% for the compressive strength and stiffness, respectively.

Table 2-3 Influence of concrete ages (UniNa mortar)

	Concrete Age			
	0 min	15 min	30 min	60 min
Compressive Strength, σ				
REF-SP0.10-M-DR3	8.80 kPa	11.64 kPa	14.00 kPa	22.48 kPa
RSD (σ)				
REF-SP0.10-M-DR3	15.87 %	11.76 %	17.49 %	14.72 %
Young's Modulus, E				
REF-SP0.10-M-DR3	210 kPa	252 kPa	430 kPa	607 kPa
RSD (E)				
REF-SP0.10-M-DR3	33.25 %	21.31 %	36.63 %	44.83 %

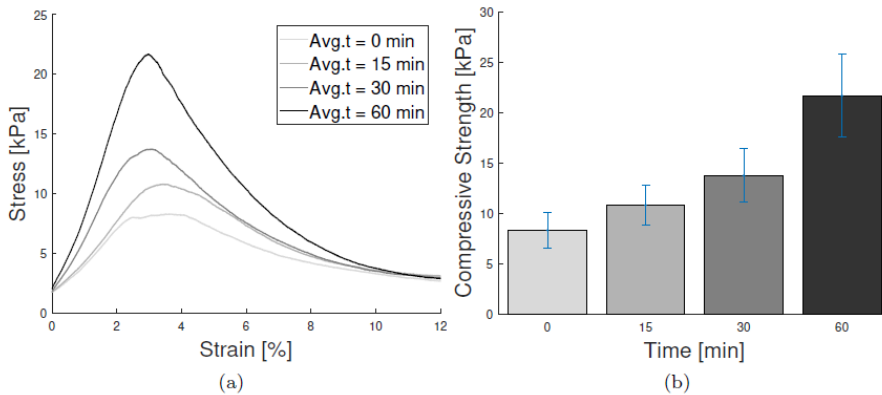


Figure 2-3: Effect of age: REF-SP0.10-M-DR3. Average comparison: (a) stress-strain curves & (b) compressive strength with the standard deviation. (UniNa mortar)

Influence of the material and sample preparation

During the sample preparation, the absence of SP in the mix (the SP0.00-M-DR3 sample series) resulted in a loss of workability/compaction and the corresponding samples were characterised by more imperfections and voids. Accordingly, the SP0.00-M-DR3 sample (see Figure 2-4(b)) mostly reproduced the state with limited compaction after the rough pouring of the material into

the mould. In contrast, an incremental increase in the SP percentage (SP0.15-M-DR3) compared to the reference mix led to the excessive fluidity of the material, resulting in possible particle segregation. Indeed, the sample series SP0.15-M-DR3 (see Figure 2-4(c)) may have reproduced the excessive manipulation of the material before testing. Figure 2-5 contains a comparison between the average time-dependent stress-strain curves of the reference mix (a) (REF-SP0.10-M-DR3) and the average curves obtained with SP values of 0.00% (b) and 0.15% (c) (SP0.00-M-DR3 and SP0.15-M-DR3, respectively). All these tests were performed using a nylon membrane inside the cylindrical mould. In cases (b) and (c), there was a reduction in the compressive strength and elastic modulus. Figure 2-6 describes the average value of the compressive strength as a function of time and the SP percentage: the mixes with too little or too much SP (SP0.00-M-DR3 and SP0.15-M-DR3) had lower compressive strength values (at $t=0$ the compressive strength was 8.80 kPa for the reference mix and about 5 kPa for SP0.00-M-DR3 and SP0.15-M-DR3) and higher relative standard deviations (RSDs). Indeed, at $t=0$, the RSD was 15.87% for the reference mix and 39.46% and 43.08% for SP weight values of 0.00% and 0.15%, respectively. Table 2-4 contains a summary of the average compressive strengths, Young's modulus and RSDs for each investigated condition. The compressive behaviour of the REF-SP0.10-M-DR3 and SP0.00-M-DR3 series was compared with the experimental data obtained without the use of the nylon membrane during the pouring of the concrete material (SP0.10-NM-DR3 and SP0.00-NM-DR3, respectively). Figure 2-7 highlights the impact of the membrane by comparing the stress-strain curves, while the average compressive strength values are summarised in Figure 2-8. The combination of 0.10% SP with the membrane produced the highest stiffness and strength values and the lowest RSDs. In contrast, the corresponding sample without the membrane (SP0.10-NM-DR3) experienced a high reduction in strength and stiffness, even at very early ages. For example, at $t=60$ minutes, the compressive strength (see Table 2-5) decreased from 22.48 kPa (REF-SP0.10-M-DR3) to 5.44 kPa (SP0.10-NM-DR3), i.e., by approximately 75%, while the

elastic modulus (see Table 2-5) decreased from 607 kPa(REF-SP0.10-M-DR3) to 124 kPa (SP0.10-NM-DR3), i.e., by approximately 80%. Furthermore, the results obtained without the membrane had higher RSDs: at 60 minutes, these figures were 14.72% and 27.78%, respectively, for REF-SP0.10-M-DR3 and SP0.10-NM-DR3 (see Table 2-5). These results were probably due to the adhesion between the plastic mould and the fresh concrete specimen: when the mould was open, part of the gravity-induced stress moved from the mould to the specimen as tangential stresses, causing an initial deterioration in the specimen itself. Additionally, if the casting occurred without a membrane, the demoulding phase could have altered the specimen in terms of its geometrical imperfections or disaggregation.

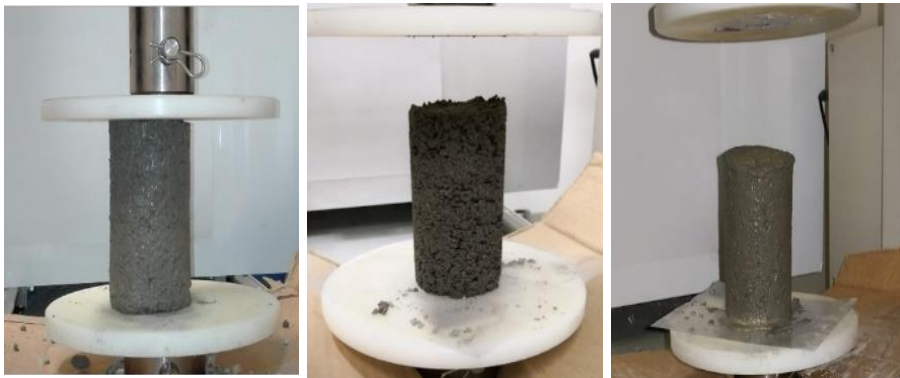


Figure 2-4: Samples prepared with different superplasticiser values: (a) REF-SP0.10-M-DR3, (b) SP0.00-M-DR3, (c) SP0.15-M-DR3, and (d) SP0.00-NM-DR3.

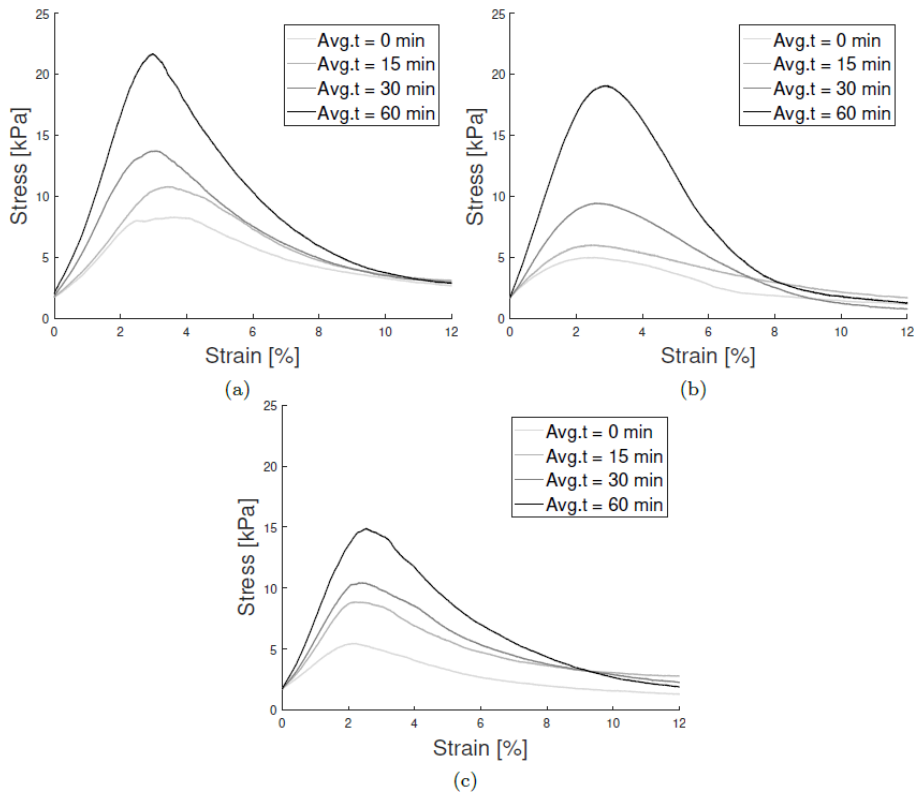


Figure 2-5: Effect of the printing condition, the average stress-strain curves: a) REF-SP0.10-M-DR3, (b) SP0.00-M-DR3, and (c) SP0.15-M-DR3. (UniNa mortar)

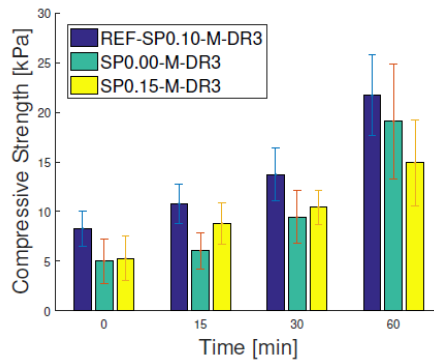


Figure 2-6: Effect of the printing condition and compressive strength, with the standard deviation. (UniNa mortar)

Table 2-4 Influence of printing conditions. (UniNa mortar)

	Concrete Age			
	0 min	15 min	30 min	60 min
Compressive Strength, σ				
REF-SP0.10-M-DR3	8.80 kPa	11.64 kPa	14.00 kPa	22.48 kPa
SP0.00-M-DR3	5.10 kPa	6.02 kPa	8.94 kPa	19.20 kPa
SP0.15-M-DR3	5.46 kPa	9.16 kPa	11.24 kPa	16.10 kPa
RSD (σ)				
REF-SP0.10-M-DR3	15.87 %	11.76 %	17.49 %	14.72 %
SP0.00-M-DR3	39.46 %	25.23 %	33.17 %	25.82 %
SP0.15-M-DR3	43.08 %	24.35 %	12.78 %	21.34 %
Young's Modulus, E				
REF-SP0.10-M-DR3	210 kPa	252 kPa	430 kPa	607 kPa
SP0.00-M-DR3	116 kPa	164 kPa	320 kPa	627 kPa
SP0.15-M-DR3	137 kPa	312 kPa	358 kPa	510 kPa
RSD (E)				
REF-SP0.10-M-DR3	33.25 %	21.31 %	36.63 %	44.83 %
SP0.00-M-DR3	98.36 %	40.41 %	45.35 %	6.71 %
SP0.15-M-DR3	75.57 %	40.50 %	15.38 %	20.90 %

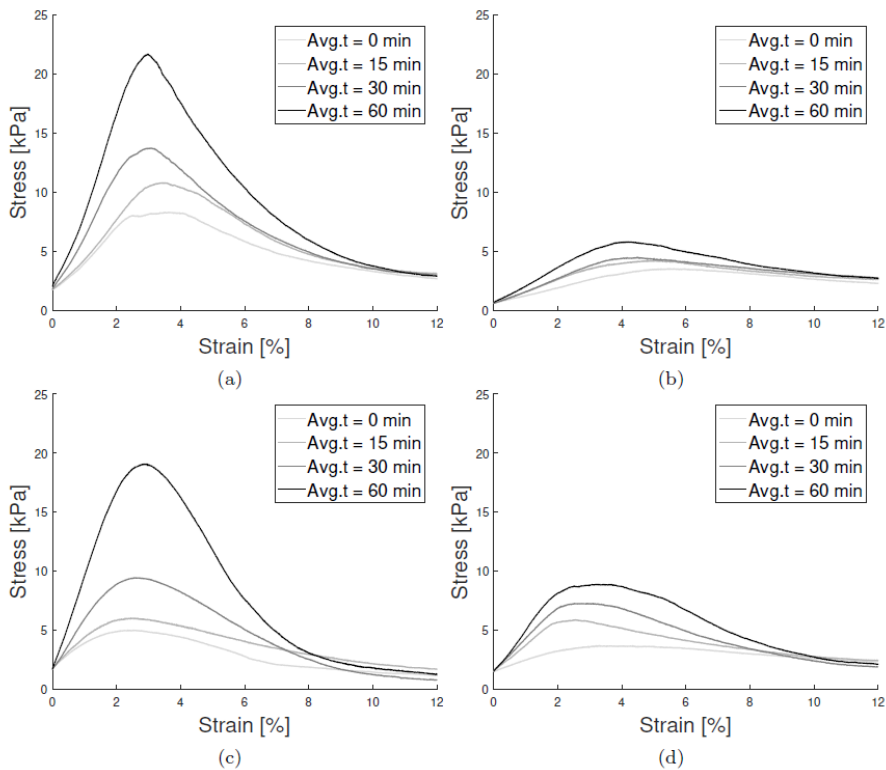


Figure 2-7: Effect of specimen preparation, average stress-strain curves: a) REF-SP0.10-M-DR3, (b) SP0.10-NM-DR3, (c) SP0.00-M-DR3, and (d) SP0.00-NM-DR3. (UniNa mortar)

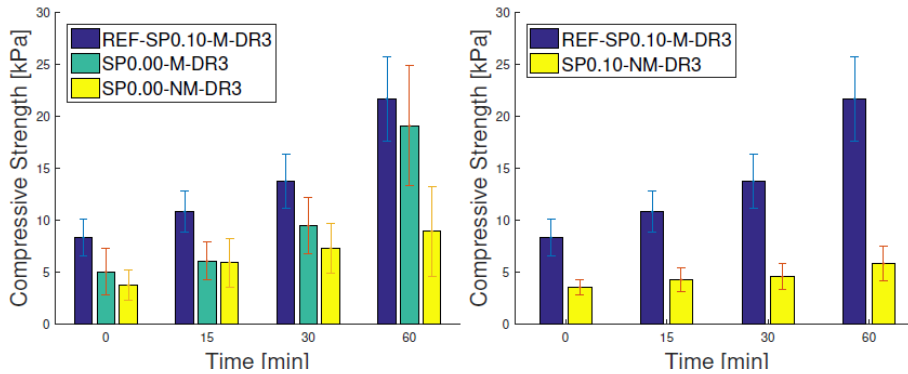


Figure 2-8: Effect of specimen preparation, average compressive strength with the standard deviation: a) REF-SP0.10-M-DR3, SP0.00-M-DR3, SP0.00-NM-DR3, and (b) REF-SP0.10-M-DR3, SP0.10-NM-DR3. (UniNa mortar)

Table 2-5 Influence of specimen preparation. (UniNa mortar)

	Concrete Age			
	0 min	15 min	30 min	60 min
	Compressive Strength, σ			
REF-SP0.10-M-DR3	8.80 kPa	11.64 kPa	14.00 kPa	22.48 kPa
SP0.10-NM-DR3	3.62 kPa	3.82 kPa	4.30 kPa	5.44 kPa
SP0.00-M-DR3	5.10 kPa	6.02 kPa	8.94 kPa	19.20 kPa
SP0.00-NM-DR3	4.14 kPa	5.92 kPa	7.56 kPa	9.82 kPa
	RSD (σ)			
REF-SP0.10-M-DR3	15.87 %	11.76 %	17.49 %	14.72 %
SP0.10-NM-DR3	25.74 %	24.45 %	21.06 %	27.78 %
SP0.00-M-DR3	39.46 %	25.23 %	33.17 %	25.82 %
SP0.00-NM-DR3	29.08 %	37.97 %	29.42 %	44.75 %
	Young's Modulus, E			
REF-SP0.10-M-DR3	210 kPa	252 kPa	430 kPa	607 kPa
SP0.10-NM-DR3	68 kPa	94 kPa	93 kPa	124 kPa
SP0.00-M-DR3	116 kPa	164 kPa	320 kPa	627 kPa
SP0.00-NM-DR3	88 kPa	182 kPa	212 kPa	305 kPa
	RSD (E)			
REF-SP0.10-M-DR3	33.25 %	21.31 %	36.63 %	44.83 %
SP0.10-NM-DR3	25.72 %	58.32 %	48.48 %	37.33 %
SP0.00-M-DR3	98.36 %	40.41 %	45.35 %	6.71 %
SP0.00-NM-DR3	57.47 %	74.31 %	66.52 %	82.50 %

Impact of the displacement rate

The average time-dependent stress-strain curves reported in Figure 2-9 were obtained using two different displacement-rate values (3mm/min vs 30mm/min) for the compression tests. The strain rate generally affected the strength values rather than the stiffness. At low concrete ages (up to 15

minutes), the increase in strength was approximate + 20% and was related to the visco-plastic behaviour of the fresh material. As expected, the compressive strength increased as the age reached 60 minutes, especially when the material became brittle: at t=60 minutes, the compressive strength at displacement rates of 3 mm/min and 30 mm/min was 22.48 kPa and 34.84 kPa, respectively, a percentage increase of about 55% (see Table 2-6). Although a higher strain rate had beneficial effects in terms of compressive strength, the experimental data were less reliable: the results of DR30 had higher RSDs (see Table 2-6). The elastic modulus did not seem sensitive to the strain rate: the difference in these values for REF-SP0.10-M-DR3 and SP0.10-M-DR30 were contained within the experimental scatter range (see Table 2-6).

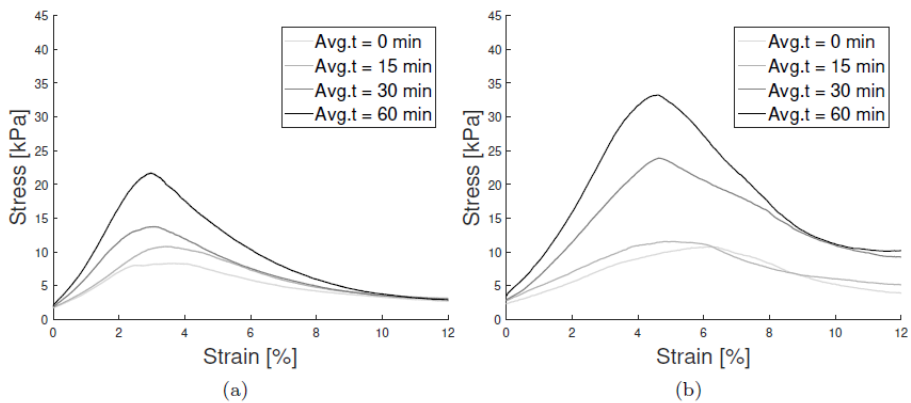


Figure 2-9: Effect of the displacement rate, average stress-strain curves: a) REF-SP0.10-M-DR3 and b) SP0.10-M-DR30. (UniNa mortar)

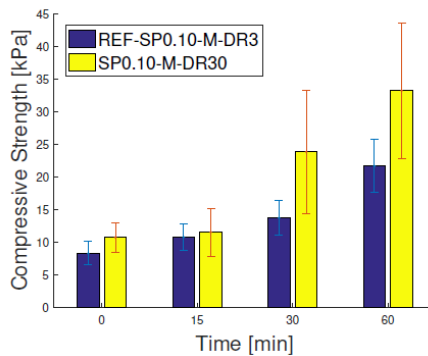


Figure 2-10: Effect of the displacement rate, average compressive strength, with the standard deviation. (UniNa mortar)

Table 2-6 Influence of displacement rate. (UniNa mortar)

	Concrete Age			
	0 min	15 min	30 min	60 min
	Compressive Strength, σ			
REF-SP0.10-M-DR3	8.80 kPa	11.64 kPa	14.00 kPa	22.48 kPa
SP0.10-M-DR30	11.14 kPa	12.54 kPa	26.04 kPa	34.84 kPa
	RSD (σ)			
REF-SP0.10-M-DR3	15.87 %	11.76 %	17.49 %	14.72 %
SP0.10-M-DR30	10.40 %	18.06 %	40.35 %	22.30 %
	Young's Modulus, E			
REF-SP0.10-M-DR3	210 kPa	252 kPa	430 kPa	607 kPa
SP0.10-M-DR30	176 kPa	256 kPa	488 kPa	763 kPa
	RSD (E)			
REF-SP0.10-M-DR3	33.25 %	21.31 %	36.63 %	44.83 %
SP0.10-M-DR30	25.44 %	21.50 %	43.21 %	17.93 %

Figure 2-11, Figure 2-12, Figure 2-13, Figure 2-14 and Figure 2-15, portray the time evolution of the compressive strength, $\sigma_{c,max}(t)$, and the stiffness, $E_c(t)$, (a and b, respectively). The empirical compressive strength and stiffness relationships as a function of the concrete age were obtained through linear regression of the experimental data related to each tested sample series. The results were then grouped and compared as a function of the concrete age to examine the impact of the material, sample preparation and displacement rate on the mechanical properties. In detail, the comparison was made by studying the effect: of the SP weight (see Figure 2-12); the use (or not) of the membrane during the casting (see Figure 2-13, Figure 2-14, respectively, for 0.00% and 0.10% SP); and the displacement rate (see Figure 2-15).

The linear fit relationships (Equation 2-6) of the compressive strength and Young's Modulus related to the reference mix (REF-SP0.10-M-DR3, see Figure 2-11) were as follows:

$$\sigma_{c,max}(t) = 0.23t + 8.24 [kPa]$$

$$E_c(t) = 6.98t + 191.4 [kPa]$$

Equation 2-6

Figure 2-12 highlights that the mixes with too little or too much SP (SP0.00-M-DR3 and SP0.15-M-DR3, respectively) produced worse mechanical

performances (by up to 58%), especially in terms of the compressive strength. This behaviour shows that the real conditions of the mortar during printing must be carefully reproduced to prevent low compaction or segregation if intense vibration is applied. Figure 2-13 and Figure 2-14 portray the impact of the membrane for SP0.00 and SP0.10, respectively. It appears to be clear that the sample is significantly altered if the demoulding phase occurs without the membrane. Such an effect was more evident for the mix with 0.1% SP, as the specimen appeared to be homogeneous after the casting (see Figure 2-4 (a)) and the only source of the disturbance was due to demoulding. Indeed, when the sample was prepared with 0% SP, there were more voids inside it (see Figure 2-4 (b)) than with 0.1% SP, and the demoulding disturbance was lower.

Furthermore, Figure 2-13 and Figure 2-14 also reveal that the effect of the membrane was more evident as the concrete age increases. Indeed, as the concrete hardened over time, the geometrical imperfections and voids, which increased in the absence of the nylon membrane, were potentially detrimental for strength development, especially when the material became more brittle. In this scenario, the failure mode was strictly linked to the propagation of cracks. This must be avoided during testing, as the material does not match the real printing conditions, in which the printed mortar generally appears to be very compacted and has no visible imperfections/voids. The comparison between the tests carried out at different displacement values (3mm/min and 30mm/min) is reported in Figure 2-15. The mechanical properties improved when the test was carried out at a higher displacement rate, especially in terms of compressive strength (approximately +21, +40, +51 and +62% for $t=0, 15, 30$ and 60 minutes, respectively). Indeed, the mechanical properties of the cementitious materials in the hardened state were known to be rate sensitive, based on three hypotheses in the literature [53]:

- The Stefan effect, which links the rate sensitivity to the presence of viscous pore fluid inside the cementitious material.

- The rate sensitivity of the crack propagation, which can alter the fracture mechanism, attenuate the crack velocity, and cause preferential cracking through higher strength regions.
- The inertial effects.

It is known that the failure of brittle materials depends on the cracking processes, while the fracture energy increases with a rising strain rate, which also increases the load [57]. Consequently, the compressive-strength increments grew with the displacement rate when the mechanical behaviour became more brittle: the distance between the two interpolating lines in Figure 2-15 (a) increases with the concrete resting time. In detail, the strength increment at 0 min (from 8.24 kPa to 9.94 kPa, i.e. a percentage increment-increase equal to 21%) was probably only due to the viscous behaviour (point 1 above), as also found for the squeeze-flow effect [58]. Meanwhile, there was a further strength increment that was probably linked to the rate sensitivity of the crack propagation as the time increased (point 2 above): at 60 minutes, the total strength increment was 13.7 kPa (an increase of about 62%). These findings highlight that a proper test displacement rate must be defined to: prevent unexpected overestimations of the compressive strength throughout the concrete age, and ensure that the testing range is compatible with the material's curing time and printing process. For instance, with a quick-setting printable mortar, higher displacement rates (in the order of tens of millimetres per minute) should be adopted for the compressive test to prevent physical changes in the specimen as a function of the concrete's age. Even though quick-setting mortar is still compatible with the printing process (i.e., higher building rates could be adopted), the rate at which each printed layer is loaded/deformed by the subsequent layers remains relatively low. Consequently, that rate must be comparable with the test loading/displacement rate to avert strain-rate effects.

In contrast, there were no appreciable changes in Young's modulus values for the resting time-examined: the difference in the values related to REF- SP0.10-M-DR3 and SP0.10-M-DR30 were within the experimental scatter range. The

linear interpolating relationships related to each case are set out in the graphic legend of the corresponding figure (Figure 2-11, Figure 2-12, Figure 2-13, Figure 2-14, Figure 2-15) concerning the strength and stiffness time-evolution. These were executed in the failure prediction analytical model (compressive and self-buckling failure) to assess the impact of the test parameters on the buildability performances of the investigated printable concrete.

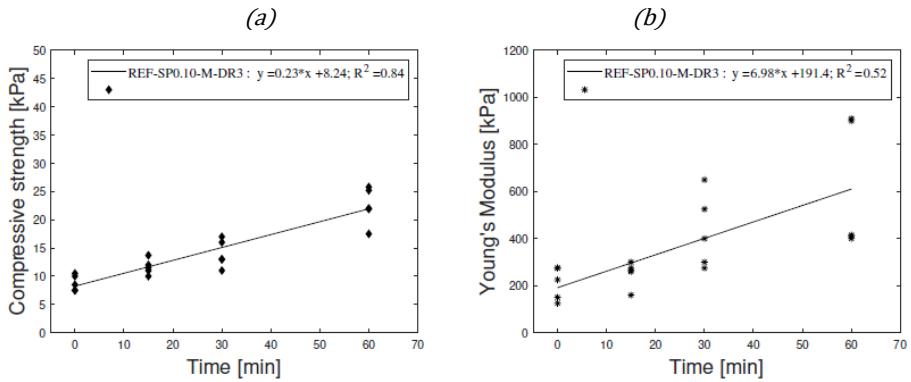


Figure 2-11: Evolution over time of the compressive strength (a) and Young's modulus (b). (UniNa mortar)

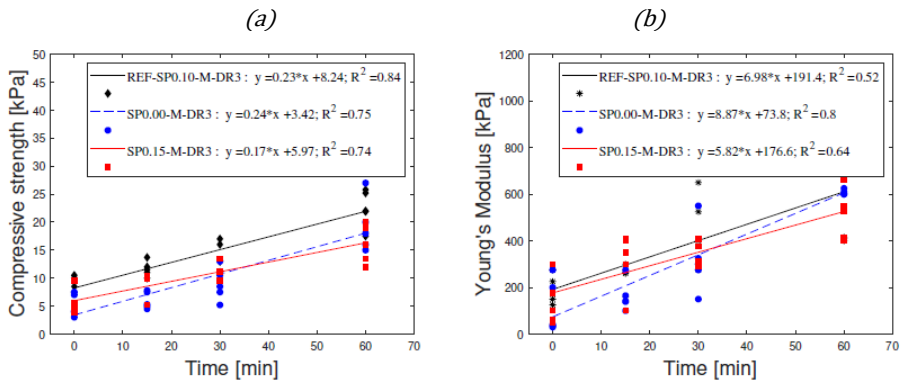


Figure 2-12: Evolution over time of the compressive strength (a) and Young's modulus (b) for different superplasticiser percentage values. (UniNa mortar)

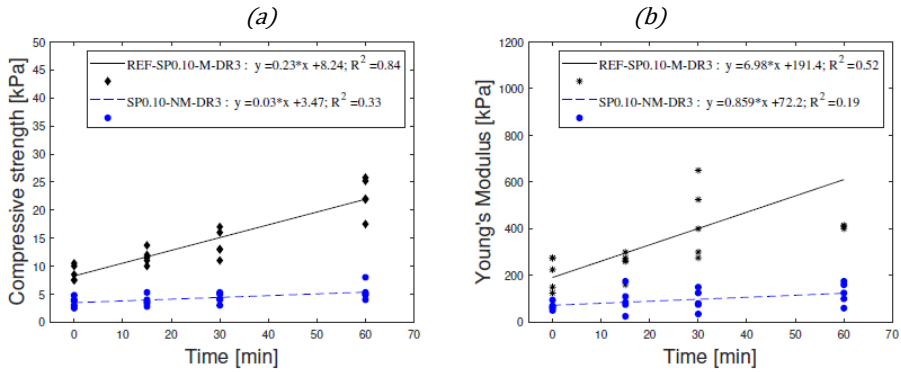


Figure 2-13: Evolution over time of the compressive strength (a) and Young's modulus (b) with and without the membrane and with SP=0.10%. (UniNa mortar)

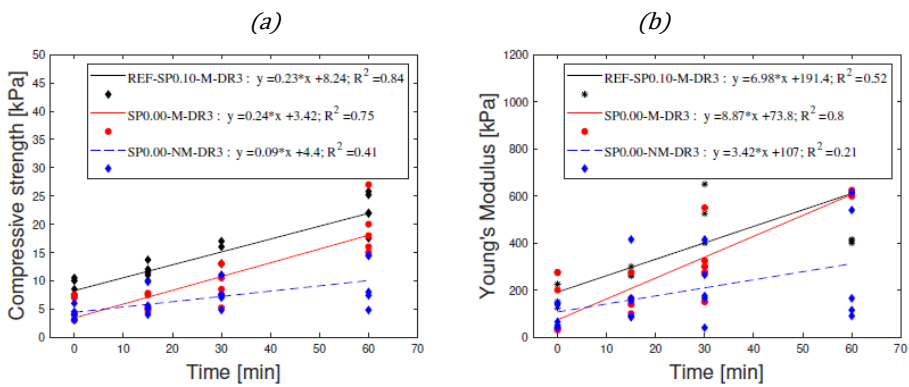


Figure 2-14: Evolution over time of the compressive strength (a) and Young's modulus (b) with and without the membrane and with SP=0.00%. (UniNa mortar)

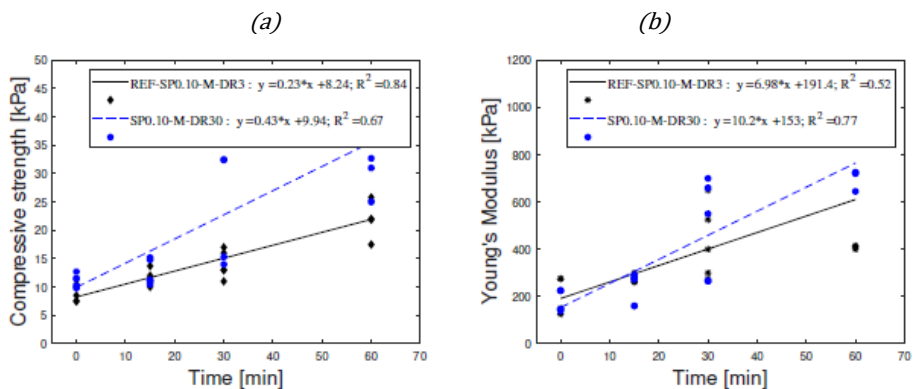


Figure 2-15: Evolution over time of the compressive strength (a) and Young's modulus (b) for different displacement rate values. (UniNa mortar)

2.1.1.3 Failure prediction during printing

The need to define an adequate testing procedure for the mechanical characterisation of printable mortars is strongly linked to the correct prediction of the critical height of the element during printing. However, it should be noted that the structural build-up process could also be affected by other issues, such as the shear stress failure, excessive deformation, and geometry imperfections. This section describes the analytical failure criterion adopted to predict the compressive failure of the first layer or the self-buckling failure of the entire printed element. The analytical criterion was used to quantify the failure prediction capability as a function of the testing-procedure variability experienced during the experimental characterisation of the compression behaviour of the printable mortars (i.e., in the absence of a standardised testing procedure).

The first failure prediction was based on Equation 2-2 and Equation 2-5, which were in turn based on the wall geometry hypothesis described in section 2.1.1 and referred to each testing condition investigated (i.e. variations in the material and testing procedure, the use of the membrane and the displacement rate). Concerning the reference mix, Figure 2-16 shows the evolution of the: experimentally-derived compressive strength (red dashed line) and vertical stress (continuous red line); the experimentally-derived Young's modulus (blue dashed line); and the critical elastic modulus (continuous blue line). The vertical axis is expressed in a semi-logarithmic scale for a better representation. All the variables are reported as a function of the stacked layers, n , which is linked to the time variable through the following expression:

$$n = \frac{t \cdot B_R}{h_{layer}}$$

Equation 2-7

In this graphical representation, the intersection point between the experimentally based and analytical criterion curves corresponds to the number of layers that determine the failure of the printing element due to self-buckling

(blue circle) or plastic yielding (red circle); the lowest values of n represent the maximum number of layers that can be produced by printing that kind of mortar. For the reference mix, the maximum compressive strength in the first layer was achieved when 49 layers were stacked above it, while the self-buckling failure occurred after the deposition of 22 layers; the self-buckling thus occurred first, and the 22 layers correspond to the failure prediction of the printed wall. The same numerical evaluation was made using the experimental stress-strain data obtained from each testing-condition variable. Figure 2-17 (a and b, respectively for analytical method, i.e. Equation 2-2 and Equation 2-5, and failure mechanism map, i.e., Suiker [56]) contains a summary of the results, reporting the number of layers corresponding to the compressive failure (coloured bars) or the self-buckling failure (square symbol); the colours represent the series groups belonging to the same experimental variation, with grey, green, orange, and blue corresponding to the reference mix, the use of the membrane, changes in the amount of SP, and the displacement rate, respectively. In all cases, the failure was due to the self-buckling. Even though the results could change with the building rate, the critical printed element height (i.e. the maximum number of layers) mainly varied depending on the specific test results adopted in the analytical failure criterion, ranging from a maximum value of 22 (for the reference testing procedure and SP0.15-M-DR3) to a minimum of 15 (SP0.10-NM-DR3) for both methods (see Figure 2-17 (a) and (b)). Based on these results, it is clear that a slight variation within the material (i.e. a variation of consistency, the presence of voids, the previous stress-state) seems to affect the compressive failure prediction more; indeed, the maximum number of layers failing in compression changed from a minimum of 15 to a maximum of 49 (reference mix). Alternatively, the displacement rate used during the compressive test could lead to a relevant error in the compressive failure prediction: the results show that by varying the displacement rate from 3mm/min to 30mm/min, there was a shift in the predicted critical number from 49 to 91. Accordingly: (a) the use of the external membrane during the casting improved the repeatability of the test results, due

to the lower disturbance induced on the sample during the demoulding - the failure prediction was more trustworthy when the external membrane was used; and (b) the lower or higher percentage of SP used (compare SP0.00-M-DR3 and SP0.15-M-DR3 with REF-SP0.10-M-DR3) changed the maximum number from 20 to 49 and 18 to 22 (Figure 2-17(a)) and from 21 to 49 and 16 to 19, (Figure 2-17 (b)), respectively, for the compressive and self-buckling failures. Finally, both methods provided approximately the same results for the compressive failure prediction. At the same time, more significant differences were experienced for the self-buckling collapse: such differences were probably due to the increased accuracy of Suiker's model, which incorporates the most relevant process parameters [56] The variability that characterises the printing process/material and, in turn, the testing procedures could significantly affect the failure prediction. Until now, a good matching between numerical/analytical models and the experimental buildability tests has been demonstrated in a limited number of cases [40, 48, 56]. It should be pointed out that, to achieve accurate modelling (FEA or analytical), it is also necessary to consider additional important aspects, such as the geometry of the printed object, modelling strategy, material/process imperfections etc. These findings underline the need to define standard procedures for the mechanical characterisation of the material to achieve greater reliability of results to be used in predictive analytical/numerical models.

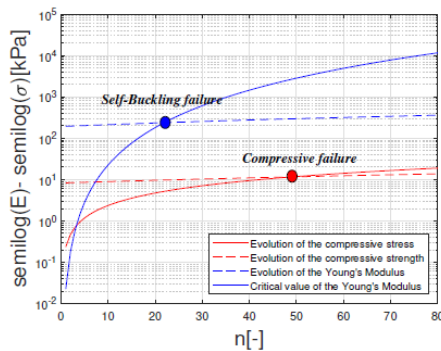


Figure 2-16: Comparison between the compressive strength and the vertical stress (red curves) and between the Young's modulus and the critical elastic modulus (blue curves) for the reference mix.

(a)



(b)

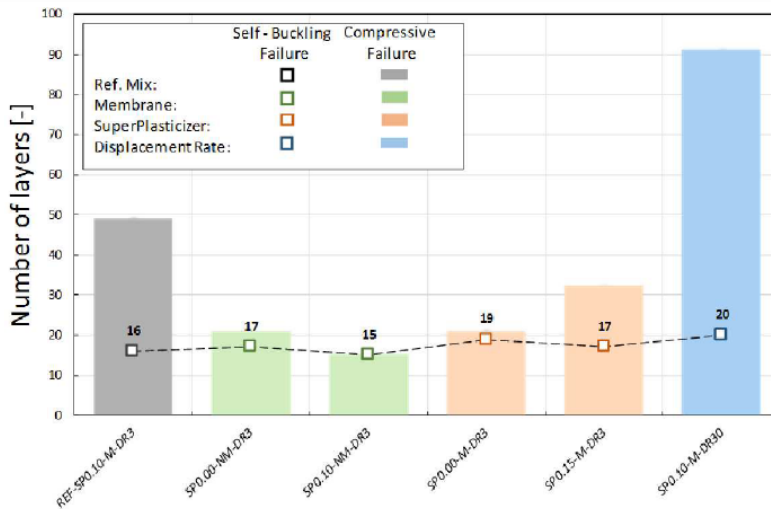


Figure 2-17: Summary of analytical failure prediction - maximum layers' number - for each case examined: (a) analytical method, i.e. Equation 2-2 and Equation 2-5, and (b) failure mechanism map, i.e., Suiker [56]

2.1.1.4 Remarks and recommendation

This section presented and discussed possible correlations between experimental characterisation procedures and failure criteria for 3D-printable concrete mixes.

The experimental program consisted of unconfined uniaxial compression tests (UUCTs) on a reference concrete-printable mix that was subjected to changing testing procedures, including the: (a) concrete age; (b) material and sample preparation; and (c) displacement rate adopted.

- (a) The concrete age affects the early-age mechanical response. As the resting time increased to 60 minutes, there was a transition from plastic to brittle behaviour and an increase in strength (from 8.80 to 22.48 kPa) and stiffness (from 210 to 607kPa). This behaviour was also experienced when varying the testing procedures.
- (b) In the reference mix, the amount of SP used was varied to bring about material preparation/compaction changes. Increasing and decreasing the quantity of SP appeared to lower the strengths, stiffness (strength began at 5kPa for both SP0.00 and SP0.015) and experimental scatter (RSD reached a peak of 43.08%). This aspect highlights the need to accurately reproduce the physical state of the printing mortar without excessive compaction while also avoiding rough pouring.
- (c) The sample preparation was varied to evaluate the use of the membrane during casting. The results without the membrane had the lowest strength (from 3.62 to 5.44 kPa) and stiffness (from 68 to 124 kPa), exhibiting high variability (compressive strength RSD reached a peak of 44.75%). This indicates that smooth surfaces protect the specimen from imperfections and voids that are detrimental for compressive tests.
- (d) The displacement rate affects the stress-strain response at different concrete ages. As the rate increased, there was a large rise in compressive strength (from 22.48 to 34.84 kPa), despite a decrease in accuracy (compressive strength RSD reached 40.35%).

Starting from the experimental compressive strength $\sigma_{c,max}$ (t) and stiffness E (t) relationships, an analytical failure criterion was used to predict the printed element's compressive or self-buckling failure. Summarising:

- In the whole cases, i.e. for each testing protocol, the failure was due to the loss of stability.
- Failure due to compression was much more affected by the testing variability, especially when considering the effect of the displacement rate, which led to more significant differences.
- The use of an external membrane improved the repeatability of the test, and the failure prediction was more reliable.
- The overall effect of the various testing procedures may lead to a failure prediction variability in the range of 30-40%.

2.1.2 UUCTs: strength and stiffness evaluation

In the previous section, the experimental campaign was presented and discussed for the UniNa 3D printable mortar to set up reliable testing procedures for determining the compressive behaviour of the investigated materials. It allowed to bring out the adequate procedure for preparing cylindrical specimens of 3D printable mortar at fresh state along with the setup of relevant testing parameters. Following such procedure (i.e. specimen preparation and testing set-up), the compressive behaviour of i.tech mortars developed by Italcementi (i.e. i.tech N and i.tech NF) was studied through a similar experimental campaign. At the innovation laboratory (i.lab) of Italcementi, a large number of UUCTs were executed by varying the specimen Aspect Ratio ($AR=0.5, 1$ and 2) and the Displacement Rate ($DR=5, 10$ and 30 mm/min) adopting the Design of Experiments methods (DoE). However, only the more significant results are presented (i.e., $AR=2$ and $DR=5$ and 30 mm/min).

More in detail, the aim was to evaluate the stress-strain relationship of the fresh i.tech mortars over time and assess the time-dependent constitutive law in terms of Young's modulus and compressive strength.

2.1.2.1 Experimental program

Uniaxial unconfined compression tests were performed at different values of the concrete age, i.e. $t=0$, 10, 20 and 30 minutes for the cementitious formulations i.tech N and i.tech NF. Also in such case, the reference time $t=0$ was the shortest time, about 6 minutes, necessary to start the test (taking into account the sample preparation and its placement into the testing machine).

In the mixing procedure, the dry components were mixed with water using the Hobart mixing machine for 4.5 minutes. The resulting material was used to prepare the cylindrical specimens, with a diameter of 60mm and a height of 120mm. The mortar was cast inside a 3D printed plastic mould (Figure 2-18 (a)) internally coated with a membrane. The membrane and disarming oil helped the demoulding procedure (Figure 2-18 (b)) after the specimen position into the testing machine: this operation required about 6 minutes (counted from the end of the mixing phase).

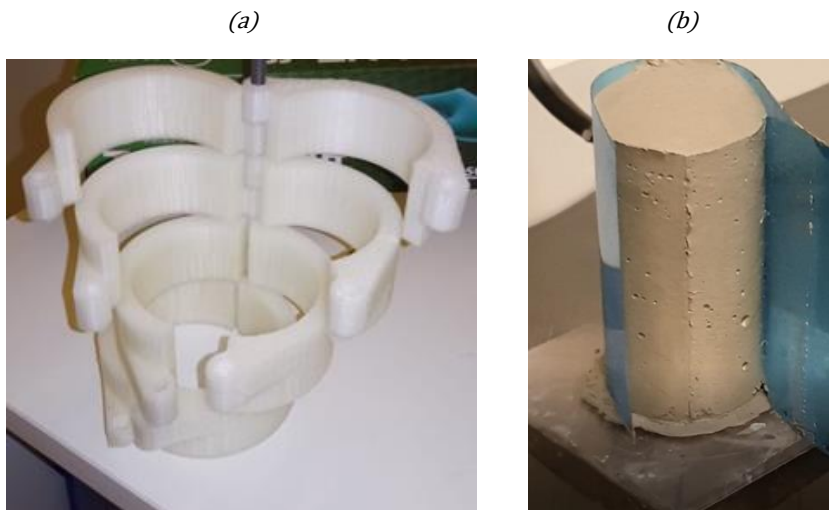


Figure 2-18: (a) 3D printed plastic mould and (b) specimen demoulding.

The testing machine used was the MTS electromechanical Universal Testing Machine with a 1kN cell capacity (a picture of the testing set-up is reported in Figure 2-19). A 2N preload was applied to the specimen just after its demoulding in order to have a flat loading surface. Then the load was removed,

and the test began only after waiting for the resting time (0, 10, 20 or 30 minutes).

The tests were carried out under displacement control, adopting 5 and 30 mm/min as cross-head displacement rate values ("DR"). These values are similar to those adopted in section 2.1.1 and were chosen to study the effect of (i) the strain rate applied and (ii) testing duration in relation to the hardening of the material. The strain rate $\dot{\epsilon}$ applied to the specimen is given by:

$$\dot{\epsilon} = \frac{d\epsilon}{dt} = \frac{d}{dt} \left(\frac{h_{specimen}(t) - h_{specimen}(t=0)}{h_{specimen}(t=0)} \right) = \frac{1}{h_{specimen}(t=0)} \cdot \frac{dh_{specimen}(t)}{dt}$$

$$\text{where } \frac{dh_{specimen}(t)}{dt} \equiv DR \left[\frac{mm}{sec} \right]$$

Equation 2-8

Equation 2-8 returns a strain rate of 0.04 and 0.25 [min^{-1}], for DR=5mm/min and DR=30mm/min, respectively.



Figure 2-19: Testing setup: MTS electromechanical Universal Testing Machine.

The force-displacement testing output was converted in a stress-strain law. In detail, the vertical stress was obtained by dividing the recorded machine force for the updated cross-sectional area, which was assessed according to ASTM D2166/D2166M, while the strain was obtained by dividing the displacement of the loading head for the initial value of the sample height. For every specimen,

three specimens were prepared to obtain an average value of the mechanical properties and a measurement of the standard deviation. The Young's modulus value was obtained as secant modulus in the 0-2% strain range, which identified the elastic limit behaviour, while the compressive strength value was obtained as the peak stress value.

2.1.2.2 Results and discussion

Figure 2-20 and Figure 2-21 display the average stress-strain relationship over time for (a) i.tech N and (b) i.tech NF, and for DR=30mm/min and DR=5mm/min, respectively. As for the UniNa mortar, there was a transition from plastic to brittle behaviour over resting time. It can be observed that the peak position (i.e., the maximum value of the compressive strength) shifts toward a lower strain value as the time increases for each DR case.

Figure 2-22 and Figure 2-23 show the linear regression law for Young's modulus and compressive strength obtained from the elaboration of stress-strain data. i.tech NF cementitious formulation showed a higher initial value and slope of Young's modulus and compressive strength than i.tech N. This behaviour is linked to the presence of the fibres, which absorb part of the water: this results in a lower w/c ratio with consequent higher performances.

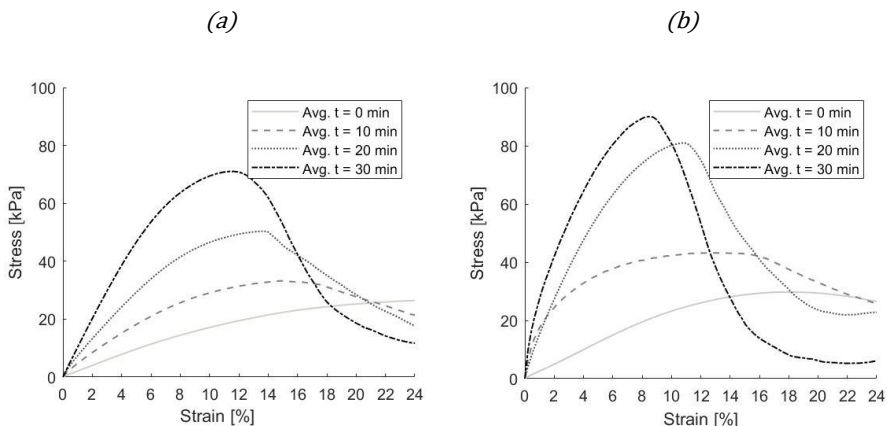


Figure 2-20: Average stress-strain curves: a) i.tech N, (b) i.tech NF (DR30)

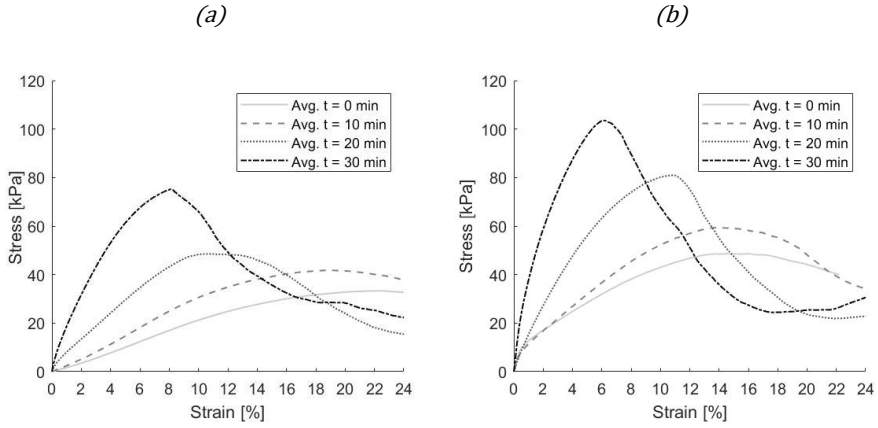


Figure 2-21: Average stress-strain curves: a) *i.tech N*, (b) *i.tech NF (DR5)*

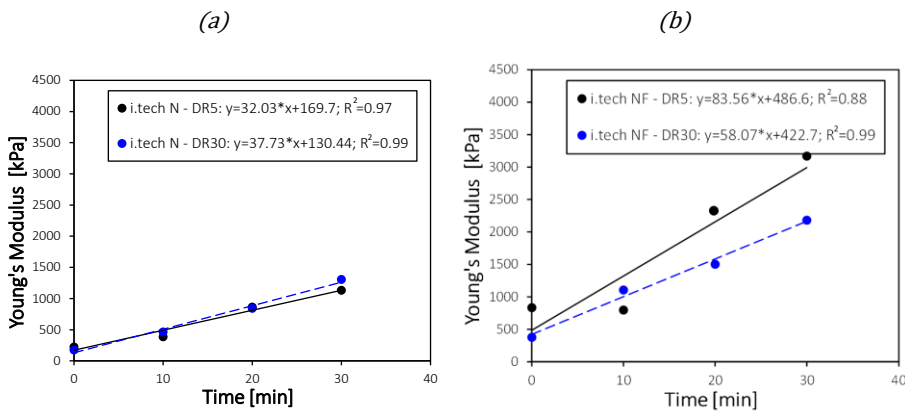


Figure 2-22: Young's Modulus: a) *i.tech N*, (b) *i.tech NF*.

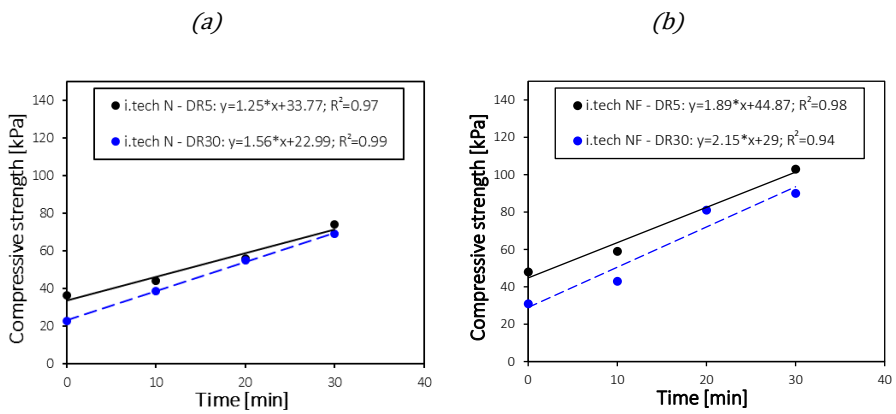


Figure 2-23: Compressive strength: a) *i.tech N*, (b) *i.tech NF*.

The different strain rate values (a) affected the mechanical strength, while (b) negligible differences were observed for Young's modulus. Considering the regression, the compressive strength grows from 22.99 to 33.77 kPa and from 29.0 to 44.87 kPa (at 0 minutes) for i.tech N and NF, respectively. Furthermore, the growth rate (i.e. the slope of the line) is slightly higher for DR=30mm/min: 1.56 vs 1.25 kPa/min and 2.15 vs 1.89 kPa/min, for i.tech N and NF.

Comparing the UCCT results between UniNa and Italcementi mortars allowed a better interpretation of the early-age behaviour of printable materials for which the extrudability is guaranteed as a common pre-requisite. Indeed, the first outcome (a) is in contrast with that observed for UniNa mortar, i.e. almost unvaried compressive strength with DR adopted; the reason is that for Italcementi mortar, the test duration is dominant over the rate sensitivity (as detected in 2.1.1.2) due to a faster setting time of the material. At the same applied strain value, the material tested with DR=5mm/min (i.e., longer test duration) has more advanced cement hydration than that tested with 30mm/min, and for such reason, it showed better compressive strength performances. This effect tends to reverse with the resting time. As experienced with UniNa mortar, the failure of brittle materials depends more on the cracking processes since the fracture energy (and, consequently, the peak load) increases with the strain rate [53]. This aspect means that (i) the compressive-strength increases with DR, and (ii) the increment in strength is more significant with the material hardening since it becomes brittle.

In contraposition, the hydration process of the UniNa mortar takes more time and starts later with respect to the Italcementi material. This difference implies that the UniNa material is more sensitive to viscous phenomena. Therefore, it appears that the hydration kinetics of a specific material suitable for 3D printing (i.e., which guarantees extrudability and pumpability) plays a major role in both i) time evolution of the mechanical properties to be used for buildability models and ii) strain rate sensitiveness which is representative of the velocity condition of the filament from the nozzle.

2.1.3 Conclusive remarks

The experimental characterisation was focused on the early-age compressive response of two types of printable mortar: UniNa and Italcementi mortar.

A preliminary experimental campaign was carried out on the UniNa mortar to study the effect of the testing procedures on the uniaxial compressive properties evaluation. Indeed, there are no standard procedures for the compressive characterisation of fresh printable mortars, and the specific experimental method adopted could influence the resulting data. Specifically, unlike cast concrete, the material's behaviour evolved during the build-up process; for such reason, the time-dependent compressive properties and the effectiveness of the testing procedures that may affect buildability were studied. Thanks to this experimental program, it was possible to define the testing procedure and highlight critical points in the investigation of fresh properties, such as the specimen preparation and the need to accurately reproduce the physical state of the printing mortar without excessive compaction avoiding rough pouring. The experimental method developed was used to investigate the different cementitious formulations used in this thesis work: the i.tech N and NF Italcementi mortars.

The completion of the UUCTs for both mortar types allowed the obtainment of the stress-strain relationships and their evolution with the resting time in the range 0-60 min and 0-30 min, for UniNa and Italcementi mortar, respectively. There was a transition from plastic to brittle behaviour and increased strength and stiffness for both materials with increasing resting time.

In addition, it was observed that the DR value affected the compressive response but differently for the tested materials. Indeed, for the Italcementi mortar, the test duration prevails over the rate sensitivity, as detected for UniNa mortar: at the same strain, the material tested with the lowest value of DR was older than that tested with high strain rate, and for such reason, it showed better mechanical performances. On the contrary, there was a significant rise in

compressive strength as the DR increased for the UniNa mortar. As a result, the correct value of DR should be high enough to avoid the material curing during the test execution but sufficiently low to do not have viscous effects (such as the rate sensitivity of the compressive strength).

In the specific case, the UniNa material is more sensitive to viscous phenomena since the hydration process takes more time and starts later with respect to the Italcementi material. This means that a higher value of DR is preferable for the Italcementi material, while the contrary is valid for the UniNa formulation.

Further efforts should be made to develop proper testing guidelines that incorporate the main features of given printing technology (e.g., available building rates, pressure during extrusion, nozzle characteristics) and the material's chemical/curing properties.

Firstly, it should be considered that the pumpability of concrete will inevitably change void distribution into the extruded filament. The precise experimental replicability of the "extruded" condition is difficult to guarantee with conventional testing methods (i.e., traditional compression testing procedures) unless compaction applies.

UUCT can provide the stress-strain relationship over time, but it cannot reproduce the effective conditions of the printed filament during the build-up construction process. Furthermore, triaxial compressive states may arise at smaller aspect ratios (i.e., extruded concrete layers), affecting the compressive strength.

It should also be noted that improved measurements techniques are desired in the future; for instance, the accuracy of the results could be improved through the optic measurement, as reported in [20]. In this way, the mechanical parameters could be reliably used in predictive models for both the printing stage (i.e., early-age concrete) and the hardened state.

2.2 Early-age creep behaviour

3D printable mortars in the fresh state (i.e., from pumping, exit from the nozzle to layer deposition) behaves predominantly as a visco-elastic material [59–61]. Generally, viscoelasticity combines viscous and elastic behaviours; the key properties of visco-elastic materials are the stress relaxation (i.e., the stress level decreases under constant applied strain over time) and the creep effect (i.e., the strain level increases under constant applied load over time). In order to distinguish and define the limit between pure viscous and elastic behaviours, the dimensionless Deborah (De) number is employed in rheology, and it is defined as the ratio of two characteristic times [62]: the relaxation time t_r [sec] (i.e., time for the material to reach the equilibrium after perturbation) and the observation time T [sec]. A low value of the De number means that the material behaves as a viscous Newtonian fluid; on the contrary, if the De value is high, the material behaviour is dominated by elasticity. Since fresh cementitious materials initiate the hardening after the extrusion from the nozzle, a transition from a visco-elastic to an elastic behaviour is expected: such transition is driven by flocculation mechanisms and cement hydration kinetics over time and depends on the specific material utilised in the 3DCP process. The layer-by-layer deposition occurring during 3DCP generates progressive and stepwise compression in the concrete filaments, which undergo increasing levels of axial strain while the hardening process takes place simultaneously. Additionally, delayed deformations of compressed layers may also appear during the automated process, specifically in the (short or long) time elapsed between subsequent deposition heights, affecting either the dimensional accuracy (i.e., through the accumulation of layer deformation) or the buildability/stability performance of the printed element. Hence, it is fundamental to characterise the long-term compressive response of printable mortars at a very early age as it can lead to additional (and/or not negligible) deformations under the progressively applied load. The mix design of printable mortars is generally characterised by a high paste volume, a low water-to-cement ratio (w/c), a high

dosage of mineral additions and superplasticiser, often mixed with a viscosity-modifying agent [63]. Such particularities affect the visco-elastic properties of the resulting fresh material: on the one hand, low water-to-cement ratios yield higher compressive strengths over time; on the other hand, high paste volumes are more sensitive to creep and shrinkage [64–66]. The evolution over time of the degree of hydration strongly influences the mechanical response in cement-based materials; therefore, higher creep strains are experienced if the traditional concrete is demoulded and loaded at early ages than in the hardened state [64, 67–72]. It is reasonable to expect similar behaviour in the cementitious materials employed in the 3DCP.

The aim of this section is to identify the critical aspects related to the early-age creep characterisation and modelling of printable mortars commonly used in 3DCP. Under a constant load, the early-age mortar shows a total strain value divided into two rates: an instantaneous and a delayed strain [67]. The former is mainly correlated to the elastic material response and adopted printing process parameters (e.g., material pressure coming from the nozzle, printing speed, building rate). At the same time, the latter is mainly studied by surface thermodynamics theories that treat the cement paste as a two-phase material, i.e., characterised by micro-diffusion of both pore water and solid particles [73]. While pore water micro-diffusion is mainly correlated with settlement, consolidation and drying phase [67], solid particles micro-diffusion makes the solid phase more mobile, and therefore it is considered the direct source of creep [73]. In fresh mortars, the time range in which the delayed strain completely develops is drastically shorter than in hardened ones: further delayed deformations certainly continue to develop over time, but their magnitude is negligible for the phenomenon and the production process herein investigated. Accordingly, such delayed strain was designated as "early-age creep" for the specific applications of 3DCP.

To this scope, time-dependent uniaxial compression tests were preliminary designed and carried out on cylindrical specimens of UniNa 3D printable

mortar to evaluate the material response under constant load at different resting times (i.e., 0, 15, 30 and 60 minutes) and, at the same time, define a proper methodological experimental approach. Then, the experimental outcomes were used to calibrate a 1-D analytical model (i.e., the Burgers' model [74]), which considers the visco-elastic response exhibited by the printable mortar.

Once determined the suitability of the Burgers' model for predicting early age creep, a similar experimental-analytical approach was implemented for the Italcementi mortars, i-tech N and NF, including, however, additional printing-related optimisation aspects in the methods. In particular, cylindrical specimens were subjected to a wider step-wise loading history, reproducing the stress state of the first stacked layer during the printing process. Since this test can reproduce any load history or – equivalently - any building rate (by varying the increment load applied for every step and the maintaining time of such force), it is more flexible and allows replicating different printing parameter values (as the interlayer time, material density and filament height). Even in this case, the experimental outcomes were successively used to calibrate the analytical Burgers model through a numerical algorithm implemented in Matlab. The resulting analytical model can be a helpful tool to predict the actual vertical displacement of a 3D printed object during the automated stacking process, including the cumulated non-instantaneous deformations. Indeed, assuming that each deposition step is characterised by an instantaneous constant load application (i.e., the weight of one filament) before the subsequent layers, the instantaneous and creep strain can be assessed. Moreover, identifying a proper time-dependent stress-strain behaviour of the 3D printable mortar is a key advancement for establishing constitutive laws to be adopted in finite element or numerical simulations. Therefore, the calibrated 1-D viscoelastic model is used to evaluate the vertical displacement of a 3D printed element, focusing on the influence of the time gap between two subsequent layers and the 3D printable mortar stiffness.

2.2.1 Theoretical background

The constitutive stress-strain relationship of a viscoelastic material is strongly dependent on the time variable, referred to the applied load or strain. In particular, the mechanical response over time is the result of both the loading history and the strain rate, and it is characterised by the stress relaxation and creep effects. The overall mechanical response is modelled through simple spring–dashpot systems (for elastic and viscous behaviour, respectively), connected in series or parallel. The constitutive equation of the elastic component (i.e., the spring) is:

$$\sigma = \varepsilon \cdot E$$

Equation 2-9

where σ [kPa] is the stress, ε [-] is the strain, and E [kPa] is Young's modulus. Equation 2-10 models the viscous time-dependent behaviour:

$$\sigma = \eta \cdot \frac{d\varepsilon}{dt}$$

Equation 2-10

where η [kPa·sec] is the material viscosity, $d\varepsilon/dt$ [sec⁻¹] is the rate of change of strain, and t [sec] is the time of observation. Typically, more articulated analytical models can be constructed from Equation 2-9 and Equation 2-10 to better reproduce viscoelastic materials' time-dependent response. The *Maxwell model* is represented by an elastic spring and a coupled viscous damper, as shown in Figure 2-24a. Since both devices are subjected to the same stress, the model is also called the iso-stress model. By applying the derivative of total strain with respect to time and using Equation 2-9 and Equation 2-10, the stress-strain relationship is governed by Equation 2-11 (the subscript “*M*” refers to the Maxwell device).

$$\frac{d\varepsilon}{dt} = \frac{\sigma}{\eta_M} + \frac{1}{E_M} \cdot \frac{d\sigma}{dt}$$

Equation 2-11

Such a model provides a stress behaviour that decays exponentially with the application of time permanent deformation (i.e., stress relaxation). The model does not accurately predict the creep effect under constant load σ_0 so the strain will increase linearly with time (with a slope of σ_0/η_M).

The *Kelvin-Voigt model* is represented by spring and damper arranged in parallel (see Figure 2-24b); both devices are subjected to the same strain, so the total stress is governed by Equation 2-12 (in which the subscript “K” refers to the Kelvin-Voigt device).

$$\sigma = E_K \cdot \varepsilon + \eta_K \cdot \frac{d\varepsilon}{dt}$$

Equation 2-12

Through Equation 2-12, it is possible to demonstrate that such a model is accurate to describe the creep effect: if constant stress (i.e., $\sigma(t) = \sigma_0$) is applied the strain ε will increase over time until a maximum value of σ_0/E_K , depending on the viscosity η_K . By contrast, the model has some limitations for stress-relaxation modelling: if a constant strain (i.e., $\varepsilon(t) = \varepsilon_0$) is applied, the model provides a constant value of the stress $\sigma = E_K \cdot \varepsilon_0$ without predicting its decrease.

A further elaboration of the spring–dashpot systems to describe viscoelastic materials is represented by the *Burgers’ model*. It comprises the Maxwell and Kelvin-Voigt models connected in series, as shown in Figure 2-24c and Figure 2-25. Intending to get the creep function, i.e., the analytical law of the time-dependent strain under constant applied load, the stress function has to be introduced through Equation 2-13:

$$\sigma(t) = \sigma_0 \cdot H(t - t_0)$$

Equation 2-13

where σ_0 [kPa] is the amplitude of the imposed stress at the time t_0 [sec] and $H(t)$ [-] is the *unit step function*. The creep function can be obtained by introducing the stress function $\sigma(t)$ (Equation 2-13) in Equation 2-11 and

Equation 2-12. Employing further analytical steps [75], it is possible to calculate the total strain $\varepsilon(t)$. As a result, the creep function of the Burgers' model can be obtained through the superposition principle, combining the response of Maxwell and Kelvin-Voigt model. The resulting analytical law for the strain variation over time is reported in Equation 2-14.

$$\varepsilon(t) = \frac{\sigma_0}{E_M} + \frac{\sigma_0}{E_K} \cdot \left(1 - e^{-\frac{t}{t_r}}\right) + \frac{\sigma_0}{\eta_M} \cdot t$$

Equation 2-14

where t_r [sec] is the relaxation time (expressed as the ratio η_K/E_K in the Kelvin-Voigt model). Equation 2-14 provides the total strain as the result of three components: the instantaneous strain, the delayed elastic strain and the irreversible creep strain (Figure 2-25). In detail, the dampers with viscosity values of η_K and η_M allow modelling the so-called primary and secondary creep, respectively. The former tends to decrease over time, whereas the latter dominates the long-term deformation with the stationary creep rate σ_0/η_M .

One of the main advantages of Burgers' viscoelastic model is the simple identification of four parameters from experimental time-dependent strain curves, as already done in literature for traditional Portland cement paste [60, 61]. This model was chosen to describe the strain response recorded under a constant applied load during experimental tests. Since the issue to be faced is related to a monotone load history of the 3D printing process, the unloading response is neglected. Specifically, the analytical model is herein used to predict the material response under the constant load related to a single-stacked layer. As a result, the total strain can be represented as the sum of two components: a time-independent strain, i.e., the instantaneous strain, and the time-dependent strain, i.e., delayed elastic strain and irreversible creep strain (as represented in Figure 2-25).

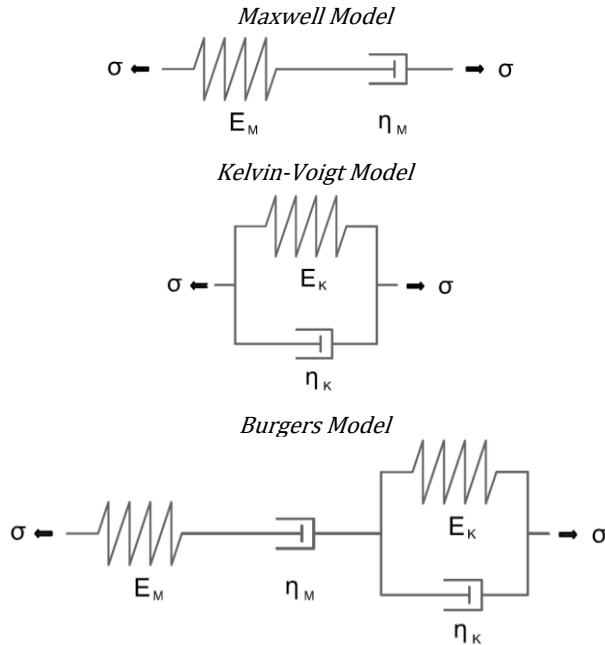


Figure 2-24: Linear viscoelastic model: (a) Maxwell, (b) Kelvin-Voigt and (c) Burgers.

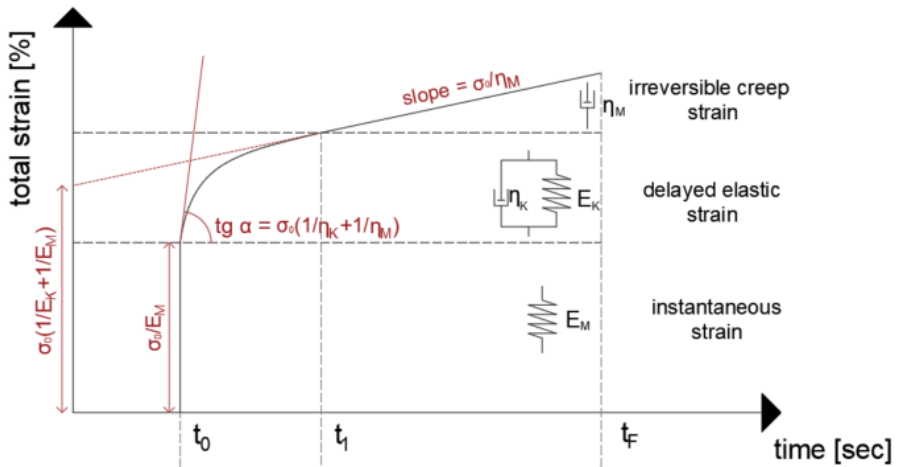


Figure 2-25: Schematisation of the Burgers' model creep response (constant load between t_0 and t_F).

2.2.2 Determination of deformation under constant load

2.2.2.1 Experimental method

Early-age creep tests under uniaxial compression load were performed on cylindrical specimens, having the diameter, d , of 60mm and the height, h , of 120mm (Figure 2-26a): the geometry was chosen to exclude size effects due to

particle size distribution and to have $h/d=2$, i.e., introducing diagonal shear failures. Specimens were tested using an MTS electromechanical Universal Testing Machine, with 10kN capacity, at room temperature $T=22^{\circ}\text{C}$ and relative humidity $RH=60\%$. According to [76], such specimens were produced using a plastic 3D-printed openable mould (in order to provide good shape retention) and by using an internal nylon membrane (to reduce the specimen-to-mould interface friction effectively). After the casting procedure, the specimen was demoulded and the membrane removed; in this way, the curing took place in the same drying condition for both the specimen and the 3D printed object.

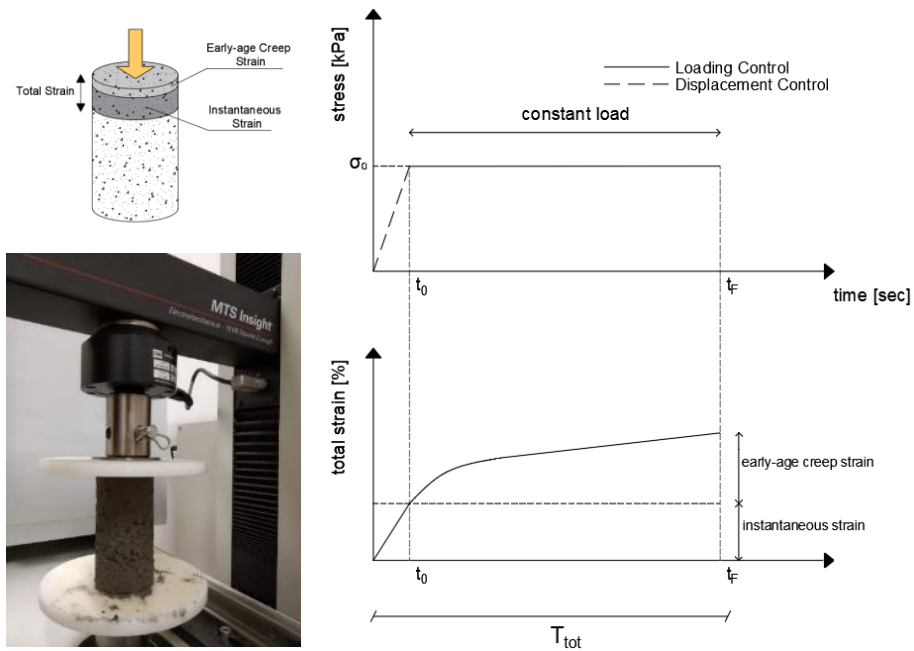


Figure 2-26: (a) Sketch and tested specimen and (b) loading history.

Figure 2-26b illustrates the loading history, which was composed of two parts: an increasing linear branch up to the target load, F_0 (i.e., 8N, the weight of the specimen), performed in the displacement-control condition in the range of time $0 - t_0$; and a horizontal - constant over time - branch, performed in the load-control condition in the range of time t_0 and t_f . The displacement vs time testing record was converted in a total strain vs time curve. In detail, the total

strain ε_{tot}^{Exp} was obtained by dividing the displacement of the loading head by the specimen height; whereas the target stress σ_0 was obtained by dividing the recorded target force F_0 by the updated cross-sectional area, assessed according to the equation provided in Section 8 of ASTM D2166/D2166M [77]. To avoid non-controlled interferences with time dependent material behaviour, the overall testing procedure was iteratively calibrated in order to satisfy two constraints:

- a) the Displacement Rate (DR) in the increasing linear branch up to the target load, F_0 must be high enough to consider the load instantaneously applied (the relaxation time t_r must be greater than the time t_0 , so that viscous strains can be considered negligible in the time range $0 - t_0$);
- b) the whole test duration ($T_{tot} = t_0 + t_f$) must permit the full development of the early-age creep strain.

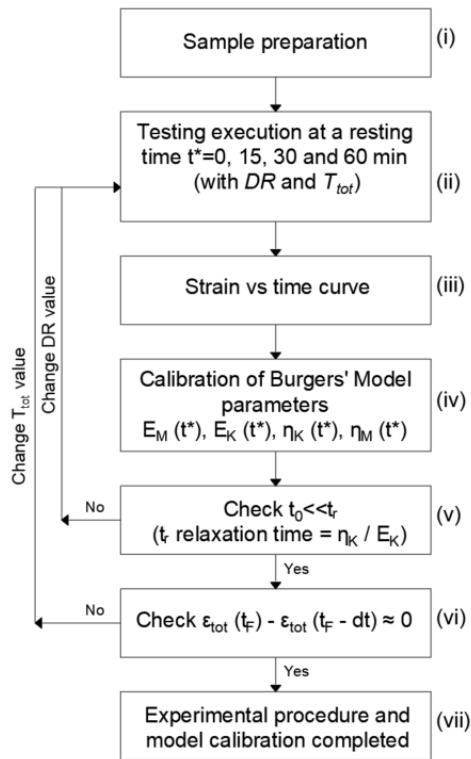


Figure 2-27: Logic scheme of the iterative process for experimental procedure and Burgers' model calibration.

For the sake of clarity, the logic scheme of the iterative process is reported in Figure 2-27. As schematically reported in Figure 2-27, (i) three specimens were prepared according to [76] and (ii) tested with an initial value of DR and T_{tot} , selecting a specific resting time among $t^*=0, 15, 30$ and 60 minutes. Subsequently, (iii) once the average total strain vs time curve was experimentally obtained, (iv) the Burgers' model parameters were assessed exploiting the following equations:

$$\text{Equation 2-15} \quad \varepsilon(t_0) = \frac{\sigma_0}{E_M}$$

$$\text{Equation 2-16} \quad \lim_{t \rightarrow \infty} \dot{\varepsilon}(t) = \frac{\sigma_0}{\eta_M}$$

$$\text{Equation 2-17} \quad \varepsilon(t_1) - \varepsilon(t_0) = \sigma_0/E_K \quad \text{where } \frac{d\varepsilon}{dt} = \text{constant for } t \geq t_1$$

$$\text{Equation 2-18} \quad \text{avg} \left(\frac{\varepsilon_{tot}^{Exp}(t) - \varepsilon_{tot}^{BURGERS}(t, t_r)}{\varepsilon_{tot}^{Exp}(t)} \right) < 0,01\%$$

Equation 2-15 allows assessing the stiffness value of the Maxwell spring, with the simplified initial assumption (to be checked with subsequent iterations) that at time t_0 only an elastic instantaneous strain arises, i.e., the viscous contribution is neglected. Equation 2-16 requires that, after t_0 , the slope of the experimental curve is equal to the σ_0/η_M ratio for long-lasting observation times: such a condition allows the determination of the viscosity value of the Maxwell damper η_M in Figure 2-24a. Equation 2-17 allows evaluating the stiffness of the Kelvin-Voigt spring E_K in Figure 2-24b, which defines the maximum value of the early-age creep strain. Equation 2-18 is used for the calibration purpose, which allows finding the relaxation time value t_r (expressed as the ratio η_K/E_K in the Kelvin-Voigt model) that minimises the relative error between experimental and analytical curve data; in detail, the matching was done in the range $t_0 - t_r$: the goal-seeking tool was used to find the t_r value, which substituted in Equation 2-14 provides an average scatter of 0.01% (i.e., $\varepsilon_{tot}^{BURGERS} - \varepsilon_{tot}^{Exp}$).

Once obtained the Burgers' parameter values, it is possible to verify that (v) the value of the time t_0 is negligible if compared with the relaxation time of the

material (i.e., condition (a) above) and that (vi) the strain is fully developed (i.e., condition (b) above).

Table 2-7: Test matrix.

Early-age creep Test (calibration procedure)			
Variables	Acronym		Target Load
Displacement Rate [mm/min]	DR _{xx}		
Test Duration [sec]	T _{yy}	DR _{xx} -T _{yy} -t _{zz}	8 N
Resting time [min]	t _{zz}		
Total specimens for iteration	3		

Table 2-7 contains a summary of the experimental tests carried out. Each iteration was executed for different values of the mortar ages (i.e., 0, 15, 30 and 60 minutes) in order to obtain the evolution over time of the resulting viscoelastic parameters that, in turn, could be useful for modelling the evolution of the printing process. Indeed, by determining the Burgers' model parameters for different resting times, each printed layer's total strain accumulated over time due to the building up process can be accurately quantified. Each specimen set is identified by the acronym "DR_{xx}-T_{yy}-t_{zz}", where: "DR_{xx}" represents the displacement rate in mm/min, "T_{yy}" indicates the test duration in seconds, and "t_{zz}" is the resting time in minutes.

2.2.2.2 Experimental results and Burgers' model calibration

By iterating the process shown in Figure 2-27, it was possible to calibrate the analytical Burgers' model for each value of the resting time (i.e., 0, 15, 30, 60 minutes), characterising the evolution over time of the viscoelastic material behaviour. The iterative process allowed obtaining the testing parameter values suitable to investigate the early-age creep for the tested fresh mortar.

Starting from DR=3mm/min and T_{tot}=300 sec, the iteration process converged to the calibrated values of DR=30mm/min and T_{tot}=500 sec. In detail, the optimal and calibrated displacement rate adopted in this study is congruent with

other works available in literature focused on cement-based printable mortar [20, 43, 78].

In the following, the experimental results and the calibrated parameters of the Burgers' model are reported and discussed. The average force vs time diagram representative of the different specimens is reported in Figure 2-28, in which it is possible to observe that a stiffer material (e.g., after 60 minutes of resting time) can reach the target load (8N) in a shorter time, once the DR is defined.

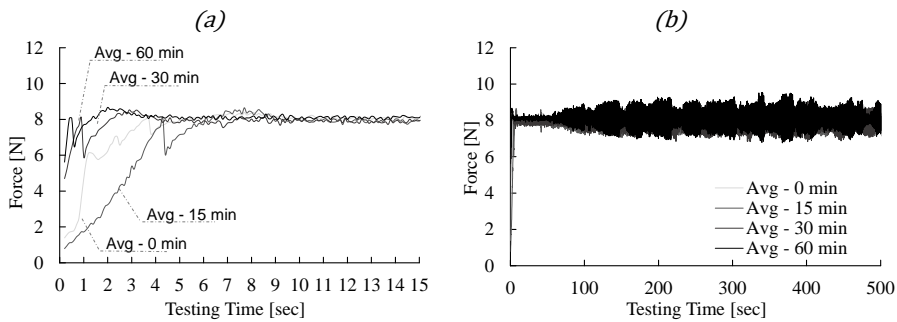


Figure 2-28: Recorded testing head force for a Displacement Rate (DR) equal to 30 mm/min: (a) total testing time, (b) zoom detail.

In Figure 2-29, the total strains ε_{tot} are plotted as a function of the testing time, from 0 to 500 seconds, for each value of mortar ages (0, 15, 30 and 60 minutes) investigated and for each tested specimen (dotted curves represent the different samples whereas continuous ones the average curves). It is worth noting that the total strain ε_{tot} decreases from 2.2% (at 0 minutes) to 0.6% (at 60 minutes) and its increment asymptotically tends to zero after about 300 seconds of testing time.

As aforementioned, fresh mortars exhibited both an instantaneous and early-age creep strain under a constant load. It is possible to notice that early-age creep deformation in time, recorded for the investigated 3D printable mortar, reflect the typical creep deformation trend of hardened traditional concrete [79, 80]; however, conversely to the creep effect in traditional concrete, early-age creep strains develop in terms of seconds. Finally, fresh mortar experimental

curves depicted in Figure 2-29 show an increasing slope of the first branch (i.e., representing the loading phase), passing from 0 to 60 minutes.

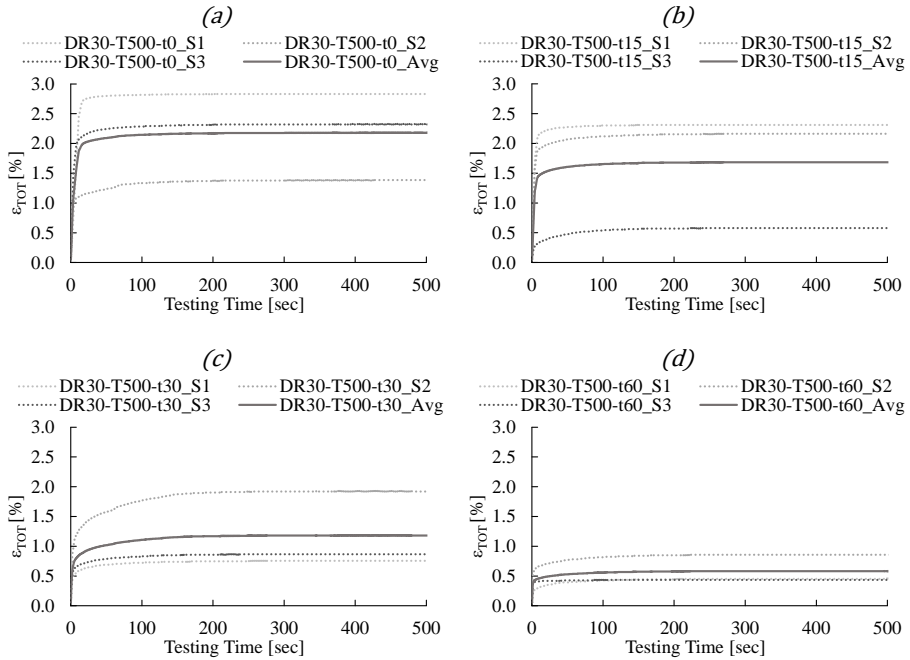


Figure 2-29: Individual and average experimental total strain VS testing time for each considered resting time: (a) 0, (b) 15, (c) 30 and (d) 60 minutes.

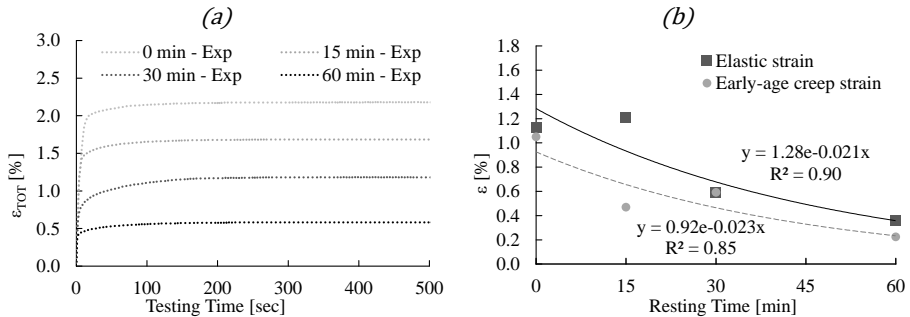


Figure 2-30: Experimental strain: (a) average total strain vs time curves, (b) elastic vs average early-age creep strain for each considered resting time: (a) 0, (b) 15, (c) 30 and (d) 60 minutes.

Figure 2-30 illustrates the experimental average total strain vs time curve, whereas Figure 2-30b summarises the amount of the elastic and early-age creep strain obtained from experiments. Both curves decrease in time due to the material hardening evolution: the early-age creep strain represents a

pronounced amount of the total vertical deformation, with a value of 1.1% and 0.2% at 0 and 60 minutes, respectively. It is worth noting that, up to 30 minutes (i.e., where it is possible to find the transition from viscous to brittle shear failure behaviour) the absolute value of early-age creep is large. The calibration of the Burgers' model parameters as a function of the resting time of the printable mortar was achieved by employing the experimental average total strain vs time curves plotted in Figure 2-30a and using Equations 6-9. Primarily, the time t_0 was found as the testing time at which the strain rate was less than 0.1% compressive strain/sec. At time t_0 , the corresponding strain value $\varepsilon(t_0)$ was assumed as the purely instantaneous elastic component. The time t_0 , as expected, strongly depends on the resting time (see also Figure 2-28): at earlier ages, the material is less stiff, so the time t_0 is higher; while for larger resting times, the function of time t_0 reduces up to zero as asymptotic limit (Figure 2-31).

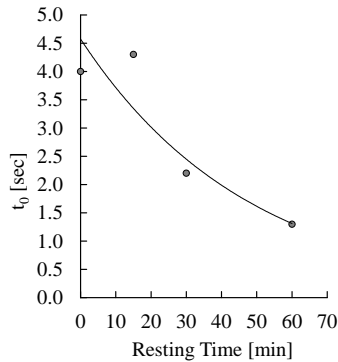


Figure 2-31: Time t_0 as a function of the material hardening.

Similarly, the values of the spring stiffness, E_M and E_k , and the value of the damper viscosity, η_K , were determined from the average curves of Figure 2-30. As a result, a time-dependent law was found for each of the Burgers' model parameters by the linear fitting of experimental data, as shown in Figure 2-32. From the analysis of the values obtained, both stiffness values (i.e., Maxwell and Voigt stiffnesses, E_M and E_K) increase with the resting time (Figure 2-32a and b); this means that both instantaneous and delayed elastic strain (Figure

2-25) tend to decrease with the hydration process. Furthermore, the relaxation time increases over time (Figure 2-32c): indeed, the evolution of the cement hydration leads to the transition from a viscous-fluid to an elastic-plastic solid behaviour, to the extent that the time required to reach the equilibrium state after a stress/strain perturbation tends to grow. Moreover, from Figure 2-30a it is clear that the last part of all time-strain experimental curves has a flat slope.

As a result, Equation 2-16 leads to a very high value of the Maxwell viscosity η_M , which means that the Maxwell damper can be neglected in this study and for the observation time selected.

$$\text{Equation 2-19} \quad E_M(t) = 9.6 \cdot t + 178.8 \text{ [kPa]}$$

$$\text{Equation 2-20} \quad E_K(t) = 15.3 \cdot t + 240.5 \text{ [kPa]}$$

$$\text{Equation 2-21} \quad t_r(t) = 0.39 \cdot t + 18.6 \text{ [sec]}$$

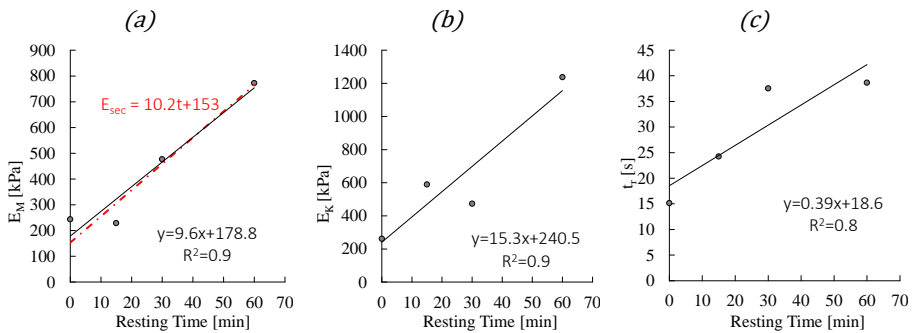


Figure 2-32: Time-dependent laws of Burgers' parameters: a) Maxwell and b) Voigt stiffness, and c) relaxation time.

The resulting analytical total strain vs time curves obtained through the Burgers' parameters are reported in Figure 2-33, along with the corresponding experimental curve.

By comparing the time-dependent law of the Maxwell stiffness $E_M(t)$ (Equation 2-19) with the time-dependent elastic secant modulus obtained from the experimental campaign carried out on the same 3D printable mortar in [76] (Equation 2-22), it was possible to observe a good matching between the corresponding total strain vs time evolution curves (see red dashed line in Figure 2-32a).

$$E_{sec}(t) = 10.2 \cdot t + 153 \text{ [kPa] from [76]}$$

Equation 2-22

It is worth noting that the former was obtained through an analytical calibration based on experimental early-age creep strain curves obtained for different resting times, whereas the latter was determined as the secant modulus achieved by uniaxial compression tests in displacement control (i.e., from stress and strain measurements). Consequently, it appears that the time evolution of the measured Young’s modulus in compression of the printable mortar roughly correspond to the elastic component of a viscoelastic system represented by the Burgers’ model and, precisely, by the Maxwell spring.

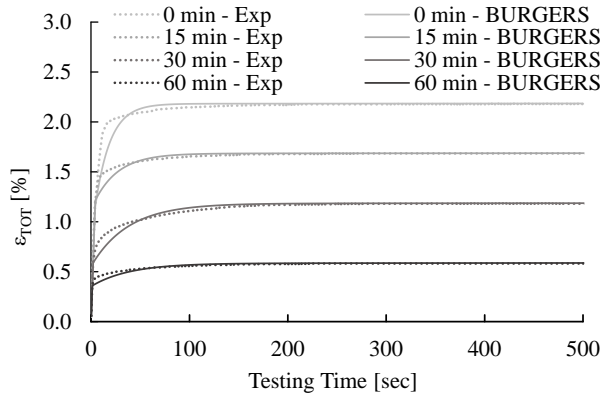


Figure 2-33: Average experimental VS analytical temporal evolution of total strain curves.

2.2.2.3 Analytical model validation

After a proper setting-up of the early-age creep testing procedure, the Burgers’ model parameters were calibrated, resulting in a good agreement between experimental average curves and the analytical strain prediction over time (Figure 2-33). The viscoelastic Burgers’ model and corresponding analytical total strain vs time curves can be used to predict the instantaneous and the viscous compressive strain of each stacked cementitious mortar layer, created during the step-by-step layered extrusion process. However, the printing parameter variability (i.e., layer height, building rate, time gap) can be significantly dependent on the geometry of the printed object as well as by the printing equipment adopted. In order to assess the robustness of the calibrated

model in terms of compression strain/displacement prediction during printing, further tests were designed and carried out experimentally to simulate the step-by-step deposition process. In particular, cylindrical specimens of dimensions 60-120 mm (diameter and height, respectively) were increasingly loaded in three different phases to simulate three stacking steps: for each increment the weight of the subsequent stacked layer acting on the first reference layer is applied and then maintained constant for 300 s in order to record creep at such stacking step, as shown in Figure 2-34.

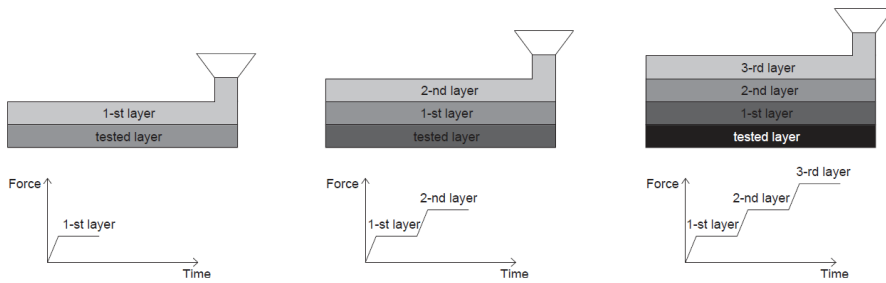


Figure 2-34: Simulation of one-, two- and three-layer stacking sequence repeated for different resting times.

The time between each loading step was fixed equal to 300 seconds. The 3D printable mortar was loaded up to the target value (i.e., 8N) with a strain-rate value of 0.025 min^{-1} . Even in these experiments, different resting time values of 0, 15, 30 and 60 minutes were investigated, and three specimens were tested for each specimen set. The corresponding analytical total strain vs time curves were generated from previously calibrated Burgers' parameters (see Equation 2-19, Equation 2-20, Equation 2-21 and Figure 2-32), as explained in Section 2.2.2.2. From those values, the analytical curve was constructed with the simple assumption that the parameters remain constant during the single-step depending only on the resting time t at which the load is applied; in that way, the total vertical strain was assessed applying the Equation 2-14:

$$\varepsilon(t) = \frac{\sigma_0}{E_M(t)} + \frac{\sigma_0}{E_K(t)} \cdot \left(1 - e^{-\frac{t}{\tau_r(t)}}\right)$$

Where σ_0 is the increment of the vertical stress at each step, and t is the testing time, which corresponds to the resting time. The comparison between

experimental average total strain vs time curves (dashed lines in Figure 2-35 including the experimental scatter as a coloured region around the average curves) and the analytical prediction according to the viscoelastic Burger’s model (continuous lines) is reported in Figure 2-35. The material loaded at 0 minutes (i.e., green curves) displays a total vertical strain at 900 seconds of 6.8 and 6.3 % (i.e., experimental and simulated values, respectively). Such values decrease with curing time, reaching 1.8 and 1.6% at 60 minutes (i.e., red curves). The maximum relative percentage error (i.e., $\frac{\epsilon_{tot}^{BURGERS} - \epsilon_{tot}^{Exp}}{\epsilon_{tot}^{Exp}} \cdot 100$ [%]) between the analytical prediction and the experimental outcomes is higher at earlier ages in correspondence with the first loading step (i.e., at 0 minutes is equal to -25%); respectively, the experimental scatter assumes the highest value that is approximately 1.47% (see the filled area around the experimental curves in Figure 2-35). The analytical model provides a good prediction on the long-term strain: the maximum relative percentage error computed at 900 s (i.e., after the three loading steps) is equal to approximately +8, -11, +4 and +8% (within the experimental scatter) at 0, 15, 30 and 60 minutes, respectively. Experimental scatter and the relative percentage error could be reduced by adopting a more accurate system measurement of the vertical deformation, as already done in other experimental investigations [20, 45, 78].

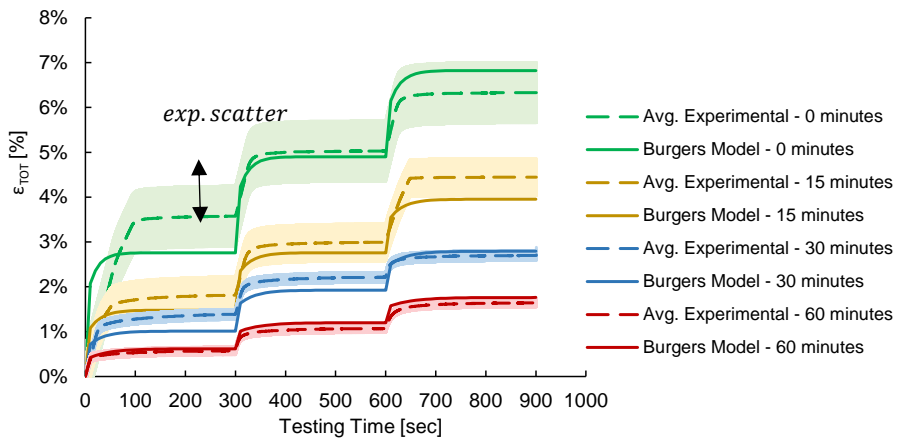


Figure 2-35: Simulation of the stacking process: Experimental VS Analytical total strain vs time curves.

Based on the satisfactory agreement obtained in Figure 2-35, the Burgers' model was further exploited to predict the total vertical displacement of printed filaments during a simulated case study based on the layered extrusion process. In detail, the total vertical displacement was additively computed from the analytical assessment of the vertical strain under the self-weight of the progressively deposited concrete layers. In the simulated case study, the layer height, h_{layer} , was fixed equal to 10 mm, therefore the increment of vertical compressive stress $\Delta\sigma$ at each deposition step acting on the first layer was:

$$\Delta\sigma = \rho \cdot g \cdot h_{layer}$$

where ρ is the material density (2411 kg/m³), and g is the acceleration of gravity. Said “-i” the generic deposition step, the resting time of the j-th stacked-layer (i.e., t_j^i) is:

$$t_j^i = (i - j) \cdot t_{time\ gap} \quad \text{with } i \geq j$$

where $t_{time\ gap}$ is the time gap between two consecutive layers. The total strain of the j-th stacked layer due to the self-weight of the i-th deposited filament, i.e., ε_j^i , was calculated through Equation 2-14. The only contribution of Maxwell and Kelvin-Voigt springs was considered in order to assess the final value of the total strain (rather its evolution), i.e., the summation of the instantaneous and creep strain:

$$\varepsilon_j^i(t_j^i) = \frac{\sigma_0}{E_M(t_j^i)} + \frac{\sigma_0}{E_K(t_j^i)}$$

in which $\sigma_0 = \Delta\sigma = 0.219\ kPa$ is a constant value, and the Burgers' parameters were assessed according to Equation 2-19 and Equation 2-20 at $t = t_j^i$. Once the vertical strain of each j-th filament for each deposition step is assessed, employing the superposition principle, it is possible to calculate the accumulated vertical displacement of a printed element with the following double summation (Equation 2-23).

$$d = \sum_{i=1}^n \sum_{j=1}^n \varepsilon_j^i(t_j^i) \cdot h_j^i$$

Equation 2-23

Where $\varepsilon_j^i(t_j^i)$ is the total vertical strain of j-th filament at i-th deposition step, and h_j^i is the updated value of the layer height, taking into account the increasing value of the deformation.

The vertical displacement depends on several technological parameters as well as the material properties, the stress imposed by a single stacked filament and the total height of the object. Assuming a straight 3D printed wall composed of 50 layers, 500 mm high, the total vertical displacement computed on the whole element was assessed by varying the time gap between subsequent layers and the material stiffnesses, trying to take into account different practical scenarios. In detail, according to current researches [21, 51, 81, 82], time gap values of 30, 120, 300 and 900 seconds and an increment of material axial stiffness of 25, 50 and 100% (i.e., E_M and E_K) at time 0 minutes were considered.

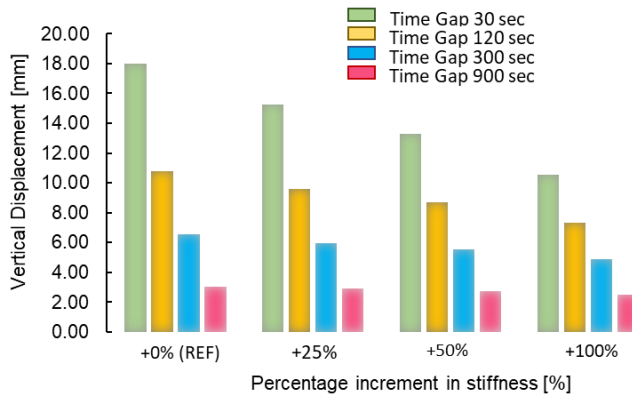


Figure 2-36: Vertical displacement prediction – Burgers’ Model.

Figure 2-36 summarises the analytical results of the vertical displacement prediction employing the Burgers’ model. It is worth highlighting that for the material under investigation, the main parameter that influences the vertical displacement is the time gap; indeed, the displacement of the reference mix (i.e., +0% (REF) in Figure 2-36) is equal to 20.1 mm for the lowest value of

time gap (30 s) and drops to 3.4 mm when the time gap is 900 s (i.e., with a reduction of about 83%). Moreover, in the case of stiffer mortars, e.g. the stiffness increment is 100%, the vertical displacement computed with a time gap of 30 s is 11.8 mm, i.e., reduction of about 41%.

2.2.3 Deformation under printing-type loading history

Section 2.2.2 explained the experimental method adopted to evaluate the early age creep effect under constant load, which reproduced the weight of deposited filaments over a fixed time interval. It highlighted the important role of the viscous behaviour of fresh printable mortar. It should be considered in the total compression strain (or displacement) resulting from the printing build-up of the filaments. Based on the evidence of delayed deformations characterising printable mortars, a more refined experimental approach was proposed for the Italcementi mortars. The final aim was to extend the applied (constant) load to more printing-oriented load history. In detail, cylindrical specimens were subjected to a wider step-wise loading history, reproducing the stress state of the first stacked layer during the printing process. Since this test can reproduce any building rate BR (by varying the increment load applied for every step and the maintaining time of such force), it is more flexible and allows replicating every printing condition (e.g. interlayer time, building rate and filament weight). The experimental outcomes were successively used to calibrate the analytical 1D visco-elastic Burgers' model (introduced in the previous section 2.2.1) through a numerical algorithm suitably developed in Matlab environment. As explained in section 2.2.1, the stress-strain relationship of the Burgers model depends on the time variable and the four-parameter values. Since the studied material hardens during the experimental procedure, the time dependency of the four parameters was assumed using linear or exponential laws with unknown constant coefficients $x(i)$. Hence, the goal is to find the coefficients $x(i)$ of the four time-dependent functions (i.e., $E_M(t)$, $E(t)$, $\eta_M(t)$ and $\eta_K(t)$) in order to obtain the minimum residual sum of squares (RSS) between the experimental and analytical Burgers' strain vs time curves. As a

result, the residual sum of squares can be seen as a function $f(\mathbf{x})$, where \mathbf{x} represents the vector with components the scalar $x(i)$. The algorithm finds the local minimum of the function $f(\mathbf{x})$, and so the provided solution \mathbf{x} strictly depends on the initial conditions (i.e. the vector \mathbf{x}_{trial}) and the boundary conditions \mathbf{bcs} (i.e. the domain of variability of the components $x(i)$).

2.2.3.1 Proposal of an experimental protocol

Using the Zwick Roell loading machine, an experimental campaign was designed to simulate the loading process during the printing phase (Figure 2-37 (a,c)) on cylindrical specimens with a diameter of 50mm and height of 35mm (Figure 2-37 (b)). Indeed, each layer is subject to an increasing load due to the weight of the filaments above it. It should be noted that the dimensions of the cylindrical specimens were reduced with respect to those of Section 2.2.2 to consider the aspect ratio of the printed filaments. This aspect is relevant, especially when triaxial stress distributions may arise from the compression of short height specimens (as the printed layers). The cylindrical specimens were prepared by casting the fresh mortar into a plastic mould. The membrane and the disarming oil were used to help the demoulding. Then the specimen was placed into the testing machine, and the test started after 5 minutes from the mixing. This time was defined to allow the specimen preparation and placing.

Considering the first stacked layer, the loading history $\sigma(t)$ depends on the mortar density ρ , the layer height h_{layer} and the waiting time or time gap t_{gap} :

$$\sigma(t) = n(t) \cdot \rho g h_{layer} \rightarrow \dot{\sigma}(t) = \frac{\rho g h_{layer}}{t_{gap}}$$

Where $n(t) = \text{int}\left(\frac{t}{t_{gap}}\right)$ is the number of stacked layer

Equation 2-24

With the aim to reproduce the printing load history, two layer height values, i.e. 10 and 20 mm, were combined with a time gap value of 17 and 65 s, respectively, resulting in a building rate of 2.1 and 1.1 m/h. As a result, two stress rates SR (Equation 2-24) were considered to carry out the printing-type

tests according to the proposed protocol: (a) 0.75 kPa/min (case _01) and (b) 0.39 kPa/min (case _02), i.e. 0.4 N maintained for 12 s (+ 5 s of loading ramp) and 0.8 N maintained for 60 s (+ 5 s of loading ramp). The loading history resulted in 80 steps simulating 80 stacked filaments. Table 2-8 summarises the testing parameters and the specimen names.

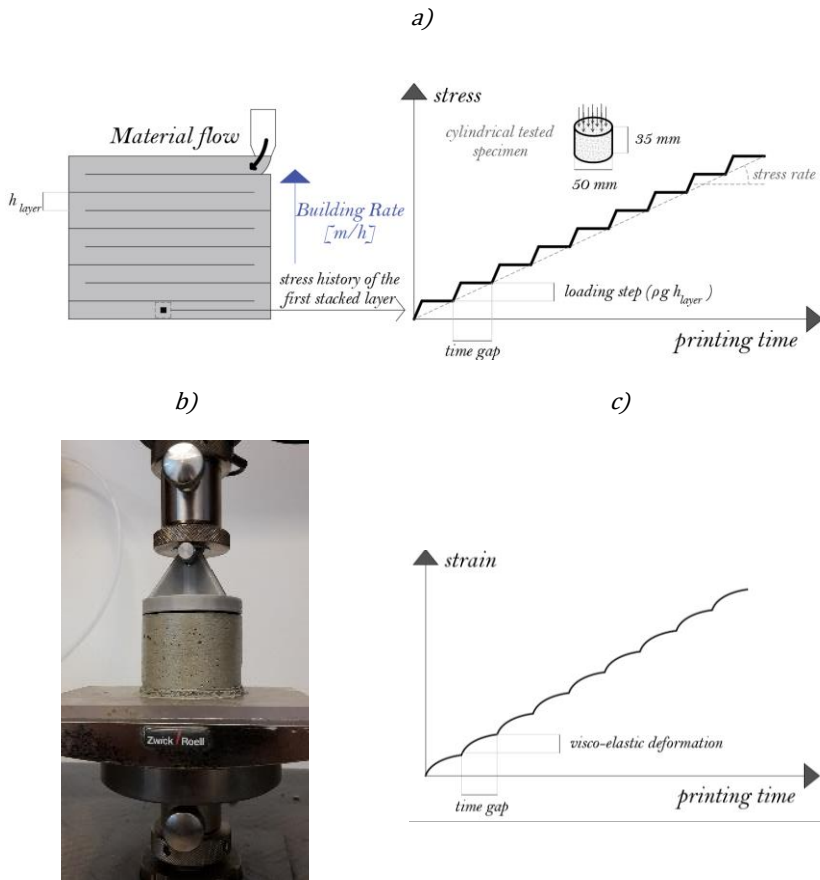


Figure 2-37: (a) Schematic representation of the stress history acting on the first layer (b) Testing set-up and (c) strain vs time visco-elastic response.

Table 2-8: Testing parameters.

Material	Specimen name	Density [kg/m ³]	Simulated printing parameters		Building Rate [m/h]	Stress Rate [KPa/min]
			h_{layer} [mm]	time gap [s]		
i.tech N	N_01	2150	10	17 (12 + 5)	2.1	0.75
	N_02	2150	20	65 (60 + 5)	1.1	0.39
i.tech NF	NF_01	2150	10	17 (12 + 5)	2.1	0.75
	NF_02	2150	20	65 (60 + 5)	1.1	0.39

The total strain ε_{exp} was obtained by dividing the displacement of the cross-head plate by the initial specimen height; whereas the vertical stress σ was obtained by dividing the recorded force F by the updated cross-sectional area, assessed according to the equation provided in Section 8 of the ASTM D2166/D2166M [77].

2.2.3.2 Experimental results and Burges' model calibration

Figure 2-38 reports the vertical strain vs time curves of two tested materials, i.tech N and NF (red and blue lines, respectively). As expected, the fresh material exhibited a viscous behaviour since the vertical deformation continued growing in the single loading step, even if the load was constant (see zoom in Figure 2-38). The two investigated materials showed a similar total vertical strain in the first 15 minutes, exhibiting an almost constant slope over time for each building rate value considered. Then, the formulation i.tech NF showed lower vertical deformations.

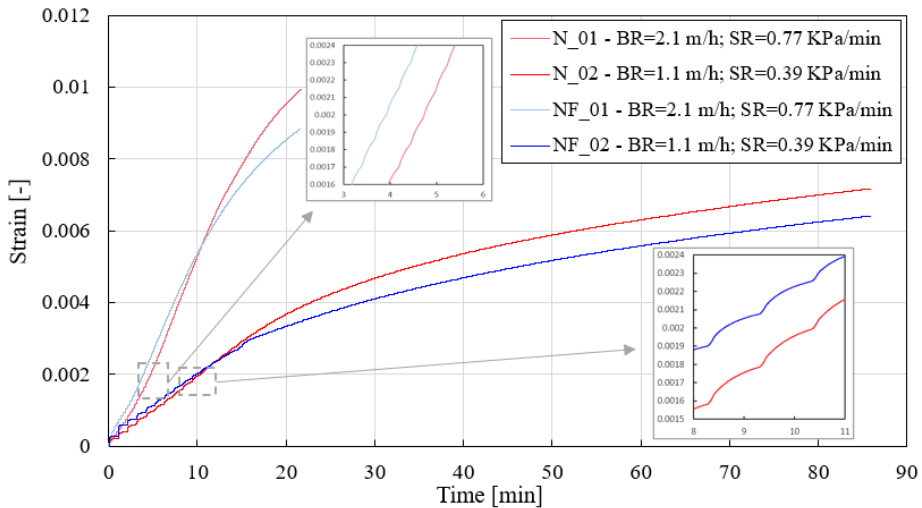


Figure 2-38: Vertical strain vs time curves for each tested specimen (*Italcementi mortars*).

Furthermore, from the global response analysis in terms of recorded compressive strain, a change in the slope after 15 minutes for both mortars and

building rates can be observed. Indeed, after this time, the strain increases at a slower rate over time. This phenomenon can be associated with the hardening initiation of the cementitious components. The final vertical strain was about 0.65 and 0.7% (with SR=0.39 kPa/min) and 0.85 and 1.1% (with SR=0.75 kPa/min), for i.tech NF and N, respectively.

From the experimental evolution over time of the compressive strain $\varepsilon_{exp}(t)$ obtained for the two printable mortar types, it was possible to calibrate the Burgers model to take into account the observed visco-elastic constitutive behaviour of the materials. The main difference with respect to the previous application of Section 2.2.2 is the history load applied: single loading step vs printing-type (multiple) step-wise load history. From the analytical point of view, the total strain over time due to the applied loading history $\sigma(t)$ can be assessed from Equation 2-11 and Equation 2-12, here reported for safe of clarity:

$$\frac{d\varepsilon}{dt} = \frac{\sigma}{\eta_M} + \frac{1}{E_M} \cdot \frac{d\sigma}{dt}$$

Equation 2-25

$$\sigma = E_K \cdot \varepsilon + \eta_K \cdot \frac{d\varepsilon}{dt}$$

Equation 2-26

Considering the evolution over time of the Burgers parameters, these equations can be rewritten as:

$$\dot{\varepsilon}_M(t) = \frac{\dot{\sigma}(t)}{E_M(t)} + \frac{\sigma(t)}{\eta_M(t)}$$

Equation 2-27

$$\sigma(t) = \varepsilon_K(t) \cdot E_K(t) + \dot{\varepsilon}_K(t) \cdot \eta_K(t)$$

Equation 2-28

The total strain of the Burgers model $\varepsilon_B(t)$ is the sum of Maxwell and Kelvin-Voigt deformation, i.e. $\varepsilon_M(t)$ and $\varepsilon_K(t)$, deriving from the above equations. The expression of $\varepsilon_B(t)$ can be evaluated through a numerical approach.

Indeed, the time derivative can be numerically assessed from the discretisation of the total time domain. If $(n - 1, n)$ is the infinitesimal interval of the continuous function $\varepsilon(t)$, the time derivative can be expressed as:

$$\dot{\varepsilon}(t) = \frac{\varepsilon(t_n) - \varepsilon(t_{n-1})}{t_n - t_{n-1}}$$

Equation 2-29

Replacing $\dot{\varepsilon}(t)$ of Equation 2-27 and Equation 2-28 with Equation 2-29, the total strain value at the time t_n is:

$$\begin{aligned} \varepsilon_B(t_n) = & \frac{\sigma_M^{spring}(t_n)}{E_M(t_n)} + \frac{\sigma_M^{damper}(t_n)}{\eta_M(t_n)} \cdot (t_n - t_{n-1}) + \varepsilon_M(t_{n-1}) + \dots \\ & + \frac{\sigma_K(t_n) - \varepsilon_K(t_n) \cdot E_K(t_n)}{\eta_K(t_n)} \cdot (t_n - t_{n-1}) + \varepsilon_K(t_{n-1}) \end{aligned}$$

Equation 2-30

Since the stress value is the same in Maxwell and Kelvin-Voigt system and assuming $\varepsilon_K(t_n) = \varepsilon_K(t_{n-1})$ (valid assumption if $t_n - t_{n-1}$ is infinitesimal), the Equation 2-30 can be rewritten as:

$$\varepsilon_B(t_n) = \frac{\sigma(t_n)}{E_M(t_n)} + \frac{\sigma(t_n)}{\eta_M(t_n)} \cdot (t_n - t_{n-1}) + \varepsilon_M(t_{n-1}) + \frac{\sigma(t_n) - \varepsilon_K(t_{n-1}) \cdot E_K(t_n)}{\eta_{KV}(t_n)} \cdot (t_n - t_{n-1}) + \varepsilon_K(t_{n-1})$$

Equation 2-31

At this point, by assigning a specific loading history $\sigma(t)$ and by means of Equation 2-31, it is possible to determine the total compressive strain of the Burgers system over time. In principle, at each time t of the printing process and for each deposited layer, the printable mortar is characterized by its own visco-elastic constitutive behaviour (with reference to the elapsed time from deposition, thus related to its hardening) and is subjected to a specific level of stress. With the aim to define the time-dependent Burgers parameters, an algorithm was developed in Matlab in order to find the four functions $E_M(t)$, $E(t)$, $\eta_M(t)$ and $\eta_K(t)$ that replaced in Equation 2-31 provide the best fitting with experimental outcomes of Figure 2-38. The function *fmincon* available in Matlab was used to minimise the residual sum of squares, which

measures the discrepancy between the experimental data and the predictive model (i.e. Burgers Model):

$$\begin{aligned}
 RSS &= \sum_{n=1}^{n_{tot}} (y_n - f(t_n))^2 = \sum_{n=1}^{n_{tot}} (\varepsilon_{exp}(t_n) - \varepsilon_B(t_n))^2 \\
 &= \sum_{n=1}^{n_{tot}} (\varepsilon_{exp}(t_n) - f(\sigma(t_n), E_M(t_n), \eta_M(t_n), E_K(t_n), \eta_K(t_n)))^2
 \end{aligned}$$

Equation 2-32

Where:

- $\varepsilon_{exp}(t_n)$ is the i^{th} value of the variable to be predicted (i.e., the experimental strain value at the time t_n);
- $\varepsilon_B(t_n)$ is the predicted value of $\varepsilon_{exp}(t_n)$, evaluated using Equation 2-31.

The minimisation problem was based on the assumption that the stiffness and viscosity of the Burgers model are linear and exponential with the time variable, respectively. The vector \mathbf{x} defines the four Burgers functions through its eight components $x(i)$, $i \in (1,8)$, as follows:

$$\begin{aligned}
 E_M(t) &= x(1) + t \cdot x(2) \\
 E_K(t) &= x(3) + t \cdot x(4) \\
 \eta_M(t) &= 10^{x(5)+t \cdot x(6)} \\
 \eta_K(t) &= 10^{x(7)+t \cdot x(8)}
 \end{aligned}$$

with $x(i)$ is the i -th components of the vector \mathbf{x}

Equation 2-33

Figure 2-39 schematically shows the Burgers calibration approach here used. Since the Burgers deformation depends on the vector \mathbf{x} , the RSS is a function of \mathbf{x} (i.e. $f(\mathbf{x})$). As a result, $f(\mathbf{x})$ is the function to minimise, and \mathbf{x} is the corresponding solution. Taking into account experimental strain vs time curves related to both stress rates, i.e. 0.75 and 0.39 KPa/min, the sum of the corresponding RSS (i.e. $RSS_{01} + RSS_{02}$) was considered for the minimisation problem.

$$f_{sum}(\mathbf{x}) = RSS_{sum} = RSS_{01} + RSS_{02}$$

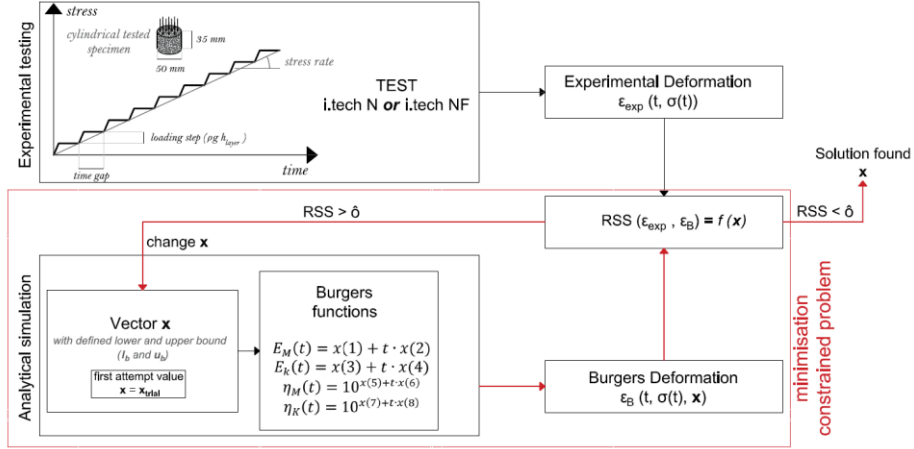


Figure 2-39: Burgers model calibration approach.

The Matlab tool *fmincon* needs to start from a user-defined first-attempt solution \mathbf{x}_{trial} . The defined vector \mathbf{x}_{trial} derived from the Burgers model calibration done for the first loading step (i.e. at $t=0$ min) of the slowest loading history (i.e. case _02 with 0.39 kPa/min). Considering the single loading step (dashed lines in Equation 2-40) belonging to the experimental compressive strain vs time curve, the constant parameters assumption is acceptable (i.e. within 65 s of time in which the material is almost unchanged from the constitutive point of view), and it is possible to estimate the value of E_M , E_K , η_M and η_K at time $t=0$ minutes (i.e. initial step). The calibration was based on similar conditions employed in section 2.2.2.2, but also considering the Maxwell damper's contribution.

$$\text{Equation 2-34} \quad \varepsilon_0 = \varepsilon(t_0) = \frac{\sigma_0}{E_M}$$

$$\text{Equation 2-35} \quad \lim_{t \rightarrow \infty} \dot{\varepsilon}(t) = \frac{\sigma_0}{\eta_M}$$

$$\text{Equation 2-36} \quad \varepsilon_K = \varepsilon_{fin} - \varepsilon_0 - \varepsilon_M = \varepsilon^{Exp}(t = t_{fin}) - \varepsilon^{Exp}(t = t_0) - \frac{\sigma_0}{\eta_M} \cdot (t_{fin} - t_0) = \frac{\sigma_0}{E_K}$$

$$\text{Equation 2-37} \quad \text{avg} \left(\frac{\varepsilon^{Exp}(t) - \varepsilon^B(t, t_\tau)}{\varepsilon^{Exp}(t)} \right) < 0,01\%$$

Equation 2-34 allows assessing the stiffness value of the Maxwell spring, with the simplified initial assumption that at time t_0 only an elastic instantaneous

strain arises, i.e., the viscous contribution is neglected. Equation 2-35 imposes that the slope of the asymptote is equal to the σ_0/η_M ratio: such a condition allows the determination of the viscosity value of the Maxwell damper η_M . Equation 2-36 allows evaluating the stiffness of the Kelvin-Voigt spring E_K . Equation 2-37 allows finding the relaxation time value t_r (expressed as the ratio η_K/E_K in the Kelvin-Voigt model) that minimises the relative error between experimental and analytical curve data.

Employing the above conditions, the Burgers model can fit the experimental curves, as shown in Figure 2-40: the average experimental curves for i.tech N (red line) and i.tech NF (blue line) are compared with the corresponding analytical Burgers curves.

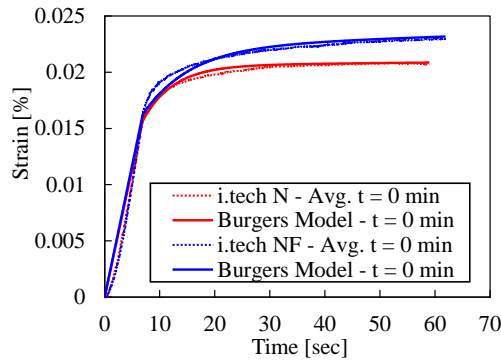


Figure 2-40: Fitting of experimental strain vs time curve for the first load step (i.e. at 0 minutes of resting time)

Table 2-9: Burgers parameters calibrated at $t=0min$

Material	E_M [Pa]	E_k [Pa]	η_M [Pa · s]	η_k [Pa · s]
<i>i.tech N</i>	$2.77 \cdot 10^6$	$8.6 \cdot 10^6$	$8.7 \cdot 10^9$	$4.7 \cdot 10^7$
<i>i.tech NF</i>	$2.69 \cdot 10^6$	$7 \cdot 10^6$	$2.64 \cdot 10^9$	$6.0 \cdot 10^7$

Table 2-9 summarises the Burgers parameters calibrated at $t=0$ min. Since these values are of the same magnitude order for both materials, the same starting point \mathbf{x}_{trial} was adopted for the optimisation.

As a result, the Burgers parameters to be used as the first attempt solution in the minimisation problem described in Figure 2-39 could be expressed as:

$$\hat{E}_M(t) = x_{trial}(1) + t \cdot x_{trial}(2)$$

$$\hat{E}_K(t) = x_{trial}(3) + t \cdot x_{trial}(4)$$

$$\hat{\eta}_M(t) = 10^{x_{trial}(5)+t \cdot x_{trial}(6)}$$

$$\hat{\eta}_K(t) = 10^{x_{trial}(7)+t \cdot x_{trial}(8)}$$

with $x_{trial}(i)$ is the i -th components of the vector \mathbf{x}_{trial}

The coefficients $x_{trial}(1)$, $x_{trial}(3)$, $x_{trial}(5)$ and $x_{trial}(7)$ define the Burgers parameters values at time $t=0$ minutes. Their values were assumed according to the magnitude order of Table 2-9. Since there is no information on the other coefficients $x_{trial}(2)$, $x_{trial}(4)$, $x_{trial}(6)$ and $x_{trial}(8)$, which define the evolution over time of the Burges parameters, a null value was assumed. Follow that the starting point \mathbf{x}_{trial} is:

$$\mathbf{x}_{trial} = [1 \cdot 10^6, 0, 1 \cdot 10^6, 0, 9, 0, 7, 0]$$

The *fmincon* also needs the boundary conditions as input, in terms of the lower bound \mathbf{l}_b and upper bound \mathbf{u}_b of each vector component $x(i)$:

$$l_b(i) \leq x(i) \leq u_b(i) \quad i \in (1, 8)$$

The adopted boundary conditions consider that the Burgers parameter values must be positive. Note that the boundary conditions adopted assumed that the Kelvin-Voigt stiffness is constant; without this hypothesis, the provided numerical optimised solution had no physical meaning since the strain decreased during the constant load phase of each step.

With these input data, the algorithm provides a solution for each material:

$$\mathbf{x}_N = [1e + 7, 1e + 2, 1e + 6, 0, 1.19e1, 7.72e - 2, 7.95, 8.58e - 2]$$

$$\mathbf{x}_{NF} = [1e + 7, 1e + 2, 1e + 6, 0, 1.19e1, 11.4e - 2, 7.87, 10.2e - 2]$$

Figure 2-41 and Figure 2-42 report (a) the Burgers functions and (b) the comparison between experimental and analytical strain vs time curves (i.e. red and black curves) for i.tech N and NF, respectively. Furthermore, the third comparison between experimental and analytical curves was reported in Figure

2-41 and Figure 2-42 (b). It is related to a further experimental test carried out with an intermediate stress rate of 0.54 kPa/min (i.e. 1.5 m/h as building rate, 0.635 N maintained for 30 s with 5s of loading ramp) used as validation of the calibrated model.

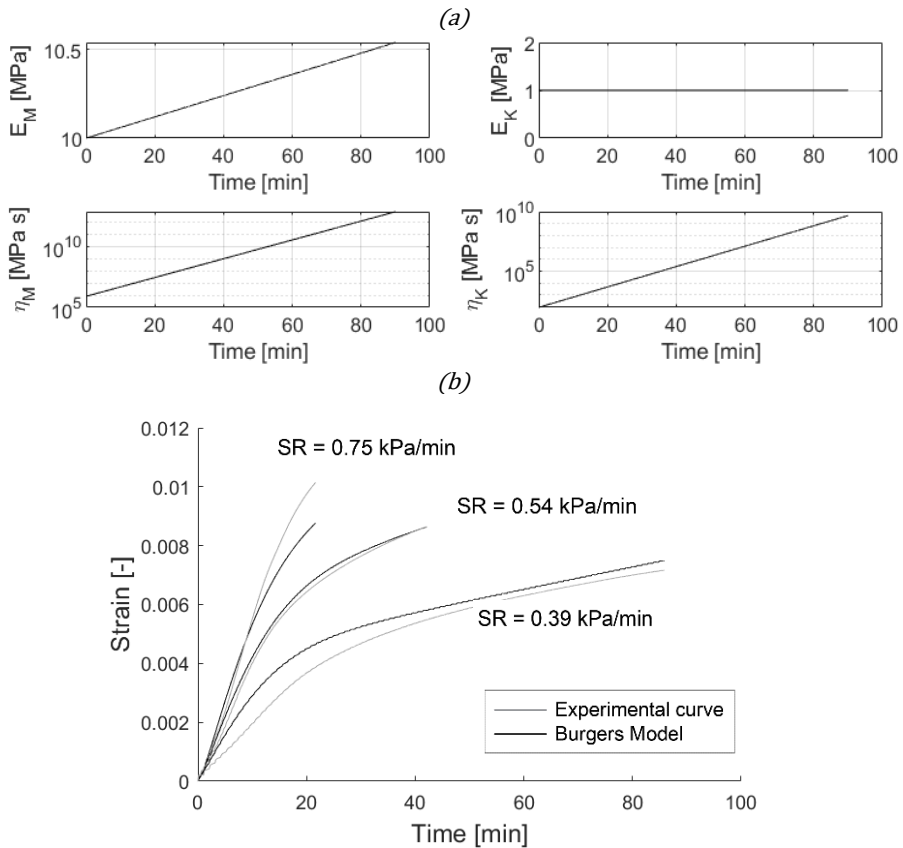
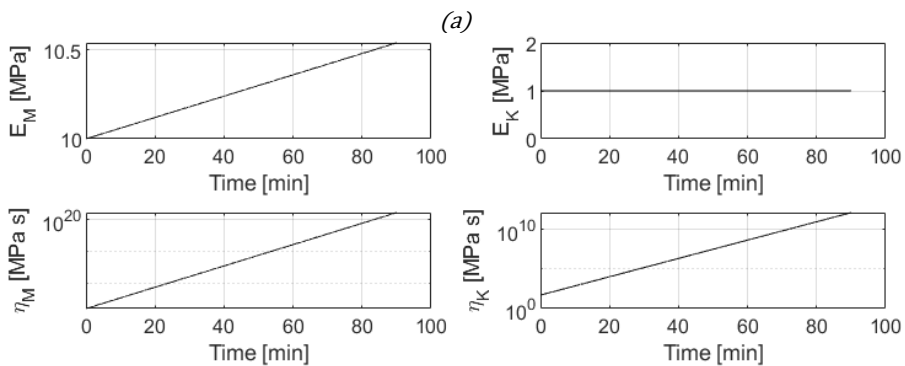


Figure 2-41: i.tech N calibration: (a) evolution of the Burgers functions and (b) Experimental vs Burgers curves ($RSS_{sum}=0.049$).



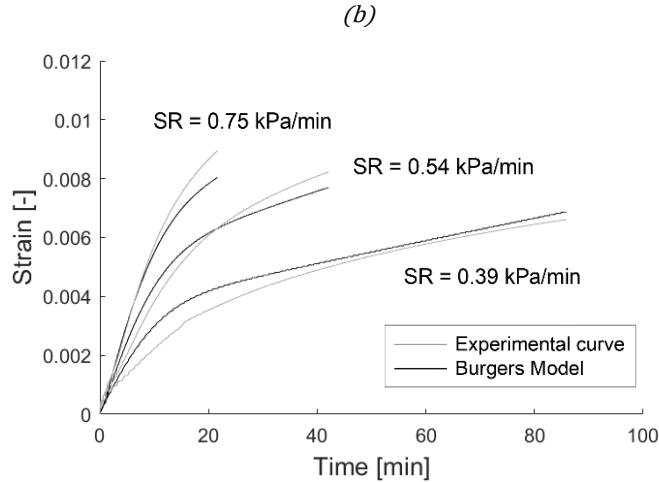


Figure 2-42: *i.tech NF calibration: (a) evolution of the Burgers functions and (b) Experimental vs Burgers curves ($RSS_{sum}=0.0211$).*

The Burgers model allowed satisfactorily predicting the cylindrical specimens' vertical strain tested with different loading histories in the investigated range ($SR \in (0.39, 0.75) \left[\frac{kPa}{min} \right]$). Figure 2-41 (b) and Figure 2-42 (b) show a good agreement of the analytical prediction with experimental data, with a final strain relative error of about -14, -2 and +4% for *i.tech N* and -10, -6 and +4% for *i.tech NF*. It is worth noting that the relative error is minimum in the intermediate case (i.e. 0.54 kPa/min), while it assumes the maximum value in extreme cases (i.e. 0.39 kPa/min and 0.75 kPa/min). On the contrary, the error is assumed to increase if the stress rate is further away from the investigated range ($SR \in (0.39, 0.75) \left[\frac{kPa}{min} \right]$). The deformation analytical prediction could probably be improved by adopting more complex Burgers functions (instead of linear and exponential laws) to better model the changes in the material properties due to curing at a very early age. Alternatively, it is possible to calibrate the Burgers parameters as both time and stress rate (SR) functions to reduce the relative error strongly. Hence, the function to minimise becomes the RSS related to the single curve and single SR value. Repeating this procedure for each experimental curve and, hence, each stress rate, three different solutions of the vector \boldsymbol{x} will be obtained (Table 2-10).

Table 2-10: Solution of vector x as a function of the stress rate.

	h_{layer} [mm]	Time Gap [min]	Building rate [m/h]	Stress rate [kPa/min]	$x(1)$	$x(2)$	$x(3)$	$x(4)$	$x(5)$	$x(6)$	$x(7)$	$x(8)$
i.tech N	10.00	0.28	2.12	0.75	7.3E+06	93.8	1E+06	0	8.4	0.07	10.2	0.07
	15.00	0.58	1.54	0.54	7.8E+06	72.7	1E+06	0	8.5	0.08	8.8	0.09
	20.00	1.08	1.11	0.39	1.1E+07	87.2	1E+06	0	8.8	0.05	8.6	0.20
i.tech NF	10.00	0.28	2.12	0.75	5.1E+06	97.7	1E+06	0	9.0	0.08	8.2	0.10
	15.00	0.58	1.54	0.54	6.6E+06	98.3	1E+06	0	11.5	0.16	8.1	0.09
	20.00	1.08	1.11	0.39	1.1E+07	95.2	1E+06	0	8.2	0.20	8.9	0.05

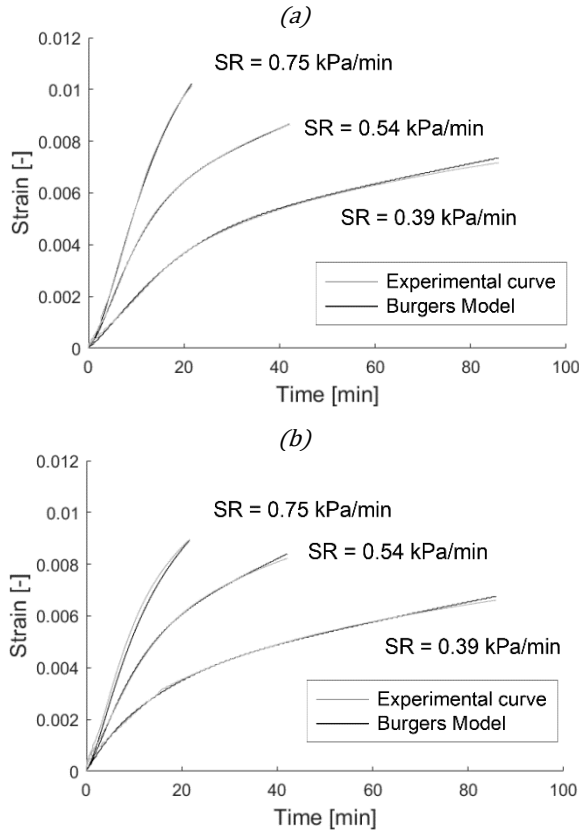


Figure 2-43: Experimental strain vs time curves fitting using a stress rate dependent Burgers model: (a) i.tech N and (b) i.tech NF.

The solutions listed in Table 2-10 provides the analytical strain vs time curves shown in Figure 2-43. As a result, it is possible to estimate the regression law of each scalar $x(i)$ as function of the stress rate SR (i.e. $x(i) = x_i(SR)$). Figure 2-44 portrays the regression of each components of the vector x . Note that the regression laws of $x(1), x(3), x(5)$ and $x(7)$ are based on the assumption that the lower bound is the corresponding rate components of the vector x_{trial} .

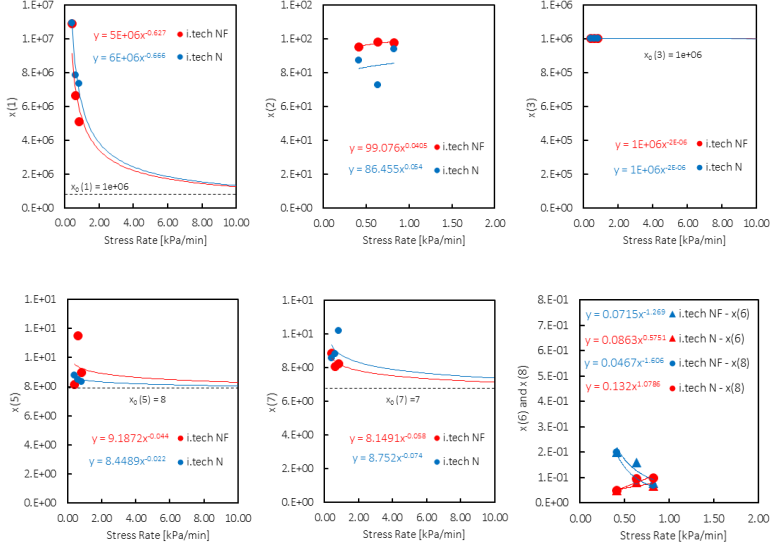


Figure 2-44: Loading-rate dependent Burgers model: LR vs vector components $x(i)$.

$$E_M = f(t, SR) = x_1(SR) + t \cdot x_2(SR)$$

$$E_K = f(t, SR) = x_3(SR) + t \cdot x_4(SR)$$

$$\eta_M = f(t, SR) = 10^{x_5(SR)+t \cdot x_6(SR)}$$

$$\eta_K = f(t, SR) = 10^{x_7(SR)+t \cdot x_8(SR)}$$

The resulting Burgers model depends on two variables: (i) the time and (ii) the stress rate. It is worth noting that such calibration is a pure-fitting of the experimental data. Still, at the same time, it allows fine reproducing the real material behaviour for every stress rate value (see Figure 2-43).

2.2.3.3 Analytical collapse prediction models and experimental validation

The main advantage of the 3D printing technology is the capability to efficiently and quickly obtain architectural and structural elements, of every shape, without formwork. Such aspect implies that the just deposited layers of fresh materials must carry their weight and those above them. So, the fresh material must have enough strength and stiffness to avoid premature collapse and excessive deformation during the production printing process. Concerning the failure, only two of the main failure modes were considered: (i) the elastic

self-buckling of the whole printed element and (ii) the plastic yielding in compression of the most loaded layer (i.e. the first layer deposited).

The following section will explain the analytical methods employed for the failure prediction. The analytical prediction will be compared with the experimental results of the buildability test performed in the 3D printing laboratory (Figure 1-2(b)). More in detail, straight walls 500 mm long were printed (Figure 2-45: P), and the width (i.e. the layer width) was varied to study the effect of the layer aspect ratio on the stability of the whole printed element. In particular, assuming a constant value of mortar flow from the nozzle, the different width value “ δ ” was ideally obtained by varying the linear printing speed and the building rate. The printing of each specimen was carried out by stacking the concrete filaments one on the other up to the failure. Table 2-11 summarises the performed buildability test and the maximum wall height record before the collapse.

Table 2-11: Buildability test matrix and results

Material	δ^{avg} [mm]	h_{layer} [mm]	Time gap [s]	Building Rate [m/h]	maximum height [mm]
i.tech N	26	10	1.43	25.2	240
	29	10	1.90	18.9	270
	39	10	2.38	15.1	380
i.tech NF	29	10	1.92	18.8	330
	42	10	2.55	14.1	225
	52	10	3.19	11.3	470



Figure 2-45: Printed specimens just before the failure.

As previously explained in section 2.1.1, a printed object can buckle due to its weight with no other forces acting on it: the failure mode is called self-buckling. The self-weight is often neglected in conventional buckling since it is much lower than the applied axial loads. However, the self-buckling cannot be neglected in 3D printing applications since the self-weight is the only acting load during the construction process, and it can lead to the collapse as the material is in the fresh state. The critical height value depends on more parameters, such as the elastic modulus, the momentum of inertia of the section and the boundary conditions. An equation for the maximum height “ H_{crit} ” assessment due to the self-buckling failure was previously introduced in section 2.1.1 and here reported for the sake of clarity:

$$H_{crit} = \left(\frac{7.83 \cdot E I_{min}}{\rho g A} \right)^{\frac{1}{3}}$$

Equation 2-38

where: E is Young’s modulus, I_{min} is the minimum moment of inertia (depending on the shape of the printed element), A is the cross-section area, and ρ is the density of the material. For the simple geometry of the straight wall, Equation 2-38 becomes:

$$H_{crit} = \left(0.65 \cdot \frac{E \delta^2}{\rho g} \right)^{\frac{1}{3}}$$

Equation 2-39

where δ is the wall width. Through Equation 2-39, it is possible to assess the critical value of the elastic modulus E_{crit} given the element height:

$$E_{crit} = 0.65^{-1} \cdot \frac{H^3 \rho g}{\delta^2}$$

Equation 2-40

These equations are based on the homogeneous material assumption. The collapse occurs if Young’s modulus is lower than the critical value of Equation 2-40. However, during the printing process, the material Young’s modulus is not constant; due to curing, the stiffness of the printing material evolves with

time, and the modulus is different for each stacked layer. In this section, two different methods will be used to predict the self-buckling collapse for the Italcementi mortar:

- A. comparing the secant modulus derived from UUCT (see 2.1.2.2) and its critical value from Equation 2-40 [as already done in literature [21]];
- B. comparing the Burgers model's equivalent elastic modulus and its critical value from Equation 2-40.

The Method A was already applied in section 2.1.1.3 to assess the collapse of 3D elements printed with the UniNa mortar. Furthermore, a more accurate analytical method based on the calibrated Burgers model will be presented (Method B). Indeed, the examined early age material showed a more complex mechanical response than an elastic one. With the aim to evaluate the self-buckling collapse, it is necessary to assess an equivalent elastic modulus to be used in Equation 2-39. The equivalent elastic modulus $E_{eq}(t)$ should be a function of the resting time and it should take into account the both instantaneous and viscous component of the deformation during the printing process. In order to obtain a more reliable failure prediction, the stress rate-dependent Burgers model was used.

The evaluation of the equivalent modulus was performed exploiting the calibrated Burgers visco-elastic model. Indeed, this model can provide the evolution over time of the vertical strain $\varepsilon(t)$, if the external load history $\sigma(t)$ is assigned (Equation 2-31). As a result, it is possible to assess the increment in vertical strain $d\varepsilon(t)$ of the printed object due to a variation of the vertical stress $d\sigma(t)$. Indeed, the printed object can be schematised as Burgers models connected in series (Figure 2-46), where each element is characterised by a different value of the resting time and, hence, a different value of four parameters.

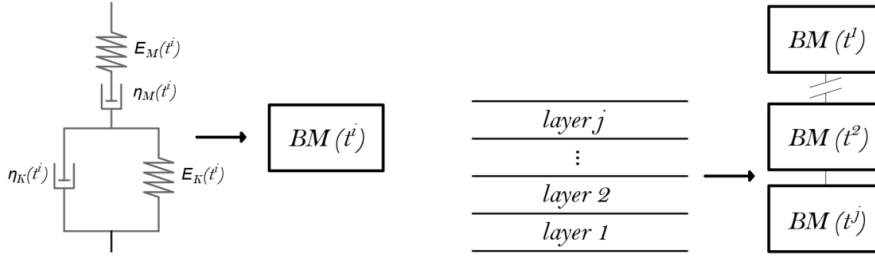


Figure 2-46: Schematisation of multiple layers through Burgers models in series.

Each layer is subject to an increasing load during the printing. Discretising the load history in small increments, the total strain of the first stacked layer $\varepsilon_{B,1}$ due to the self-weight of the deposited filaments can be assessed through Equation 2-31 (here reported for clarity).

$$\varepsilon_{B,1}(t_n) = \frac{\sigma(t_n)}{E_M(t_n, SR)} + \frac{\sigma(t_n)}{\eta_M(t_n, SR)} \cdot (t_n - t_{n-1}) + \varepsilon_M(t_{n-1}) + \frac{\sigma(t_n) - \varepsilon_{KV}(t_{n-1}) \cdot E_{KV}(t_n, SR)}{\eta_{KV}(t_n, SR)} \cdot (t_n - t_{n-1}) + \varepsilon_{KV}(t_{n-1})$$

Equation 2-41

where “n” indicates the generic increment. Note that in such equation the Burgers parameters are functions of the Stress Rate SR (or equivalently the building rate). Equation 2-41 provides the total strain of the first layer; said $\varepsilon_{B,1}(t^j)$ the strain of the first layer when the j-th filament is deposited, the deformation of the generic i-th layer $\varepsilon_{B,i}$ at the same time t^j is:

$$\varepsilon_{B,i}(t^j) = \varepsilon_{B,1}(t^{j-i})$$

Equation 2-42

Using Equation 2-41 and Equation 2-42, it is possible to assess the total strain of each layer at each deposition step. Once the vertical strain of the generic i-th filament is known, also its updated value of height is known:

$$h_i(t^j) = h_{layer} \cdot (1 - \varepsilon_{B,i}(t^j))$$

Equation 2-43

As a result, the total height $H_{tot}(t)$ of the printed object equals the sum of stacked layer heights Equation 2-44 A. Finally, the equivalent elastic modulus at the j -th deposition step equals the ratio between the increment in stress and the equivalent total strain (Equation 2-44 B).

$$H_{tot}(t_j) = \sum_{i=1}^j h_i(t^j)$$

$$E_{eq}^j(t_j) = \frac{\Delta\sigma(t_j)}{\varepsilon_{eq}(t_j)} = \frac{\sigma(t_j) - \sigma(t_{j-1})}{\frac{H_{tot}(t_{j-1}) + h_{layer} - H_{tot}(t_j)}{H_{tot}(t_{j-1}) + h_{layer}}}$$

Equation 2-44

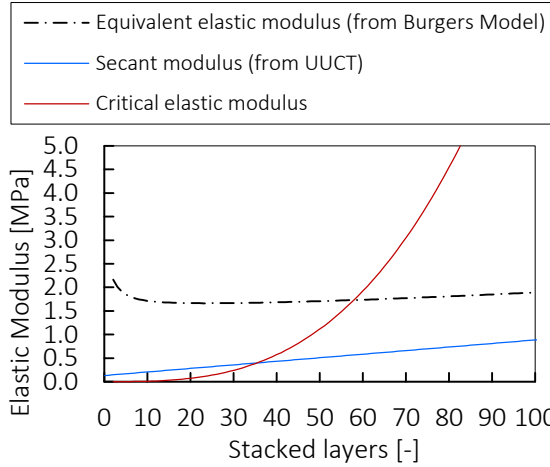


Figure 2-47: Example of self-buckling failure prevision

The stability check was conducted at each deposition step j by comparing the secant modulus $E_{sec}(t_j)$ (blue line in Figure 2-47) or the equivalent elastic modulus $E_{eq}^j(t_j)$ (black dashed line in Figure 2-47) and the critical value $E_{crit}(t)$ (red line in Figure 2-47), Method A and B respectively. The failure occurs when the stiffness of the printed element is lower than the critical value.

Concerning the plastic collapse in compression, it occurs when the vertical stress $\sigma(t)$ assessed in the most loaded layer (the first) is higher than the compressive strength $\sigma_{c,max}(t)$ (see also Equation 2-2). To this aim, the

evolution over time of the compressive strength previously assessed in section 2.1.2.2 was employed.

Experimental buildability tests (Table 2-11) were analytically reproduced to assess the maximum height. The maximum height before the compression failure of the first layer was higher than 1000 mm for each examined case. For such reason, only the self-buckling prediction will be discussed.

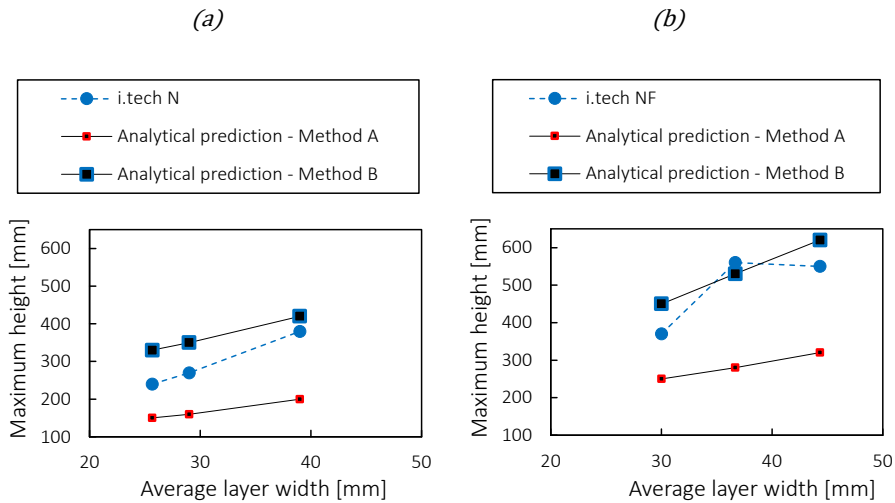


Figure 2-48: Self-buckling failure prediction: (a) i.tech N and (b) i.tech NF.

Figure 2-48 represents the analytical collapse prediction for (a) i.tech N and (b) i.tech NF provided by Method A and B. Method A underestimates the maximum height, with a maximum percentage error (i.e. $\frac{H_{max}^B - H_{max}^{exp}}{H_{max}^{exp}} \cdot 100$ [%]) of -90 and -100% for i.tech N and NF, respectively. On the contrary, Method B provides a more accurate prevision of the failure, and the percentage error is about +27 and +18%, overestimating the maximum experimental height detected. It is reasonable that the analytical prediction should overestimate the experimental data since it does not take into account the geometrical imperfection of the real printed object, which can prematurely lead to the loss of stability. With such an analytical approach for the buildability prediction, the buildability domains reported in Figure 2-49 were built for two materials. These domains could be used to predict the maximum height of a straight wall printed

with different values of the layer width and building rate. It is possible to observe that a buildability lower bound exists for the investigated materials: even if the building rate grows ($BR > 8$ m/h), the maximum reachable height does not change.

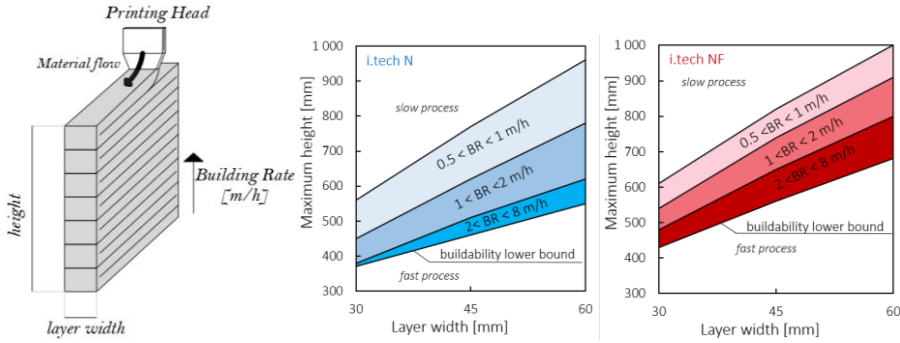


Figure 2-49: Self-buckling failure domain for *i.tech N* and *i.tech NF*.

The proposed experimental method could be used to identify the buildability properties of a generic tested material. Indeed, from the experimental strain vs time curve obtained according to the proposed protocol, the Burgers model could be calibrated and the deformation due to a stress history can be assessed with Equation 2-31. If the stress applied to the Burgers system is constant, the ratio between the strain and the applied pressure is called creep compliance CC , and it is a material property that identifies its deformability:

$$CC(t) = \frac{1}{E_M(t)} + \frac{1}{E_K(t)} \cdot \left(1 - e^{-\frac{t}{t_r(t)}}\right) + \frac{1}{\eta_M(t)} \cdot t$$

If the Burgers system is subjected to a linear loading history, it is possible to determine the equivalent material stiffness as the ratio between the stress and the strain (from Equation 2-31). As a result, each material could be characterised by a different time evolution of such stiffness. Starting from the Burgers model of *i.tech N* mortar and by only varying the value of Maxwell stiffness at time $t=0$, it is possible to create fictitious materials each of ones is identified by a stiffness vs time curve. In detail, assuming a multiplier coefficient of $E_M(t=0)$ equal to 0.30, 1.00, 1.50, 2.00 and 2.50, the master curves MC of Figure 2-50 were obtained.

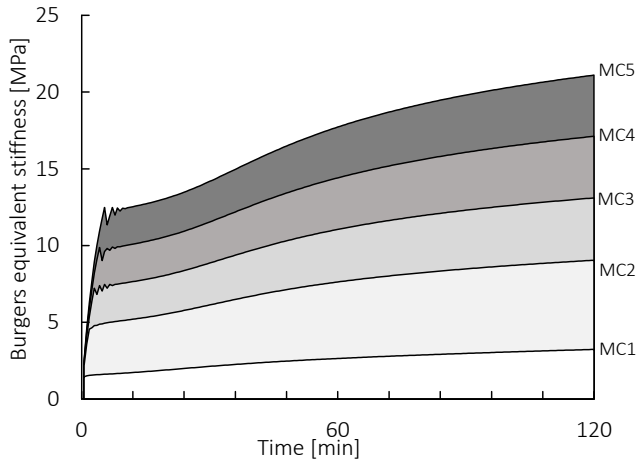


Figure 2-50: Burgers equivalent stiffness vs time curves obtained simulating material with different $E_M(t = 0)$.

Figure 2-50 could be a helpful tool to predict the buildability of a new printable mortar helping the standardisation of such requirement. Indeed, a buildability domain can be associated with each of these master curves (depending on the building rate and layer width). The buildability domains assessed for a constant layer height of 10 mm, a material density of 2150 kg/m³ and layer width values of 30, 45 and 60 mm are represented in Figure 2-51. For example, suppose the Burgers stiffness of the new tested material lies between MC1 and MC2. In that case, its buildability belongs to the corresponding light grey area in Figure 2-51.

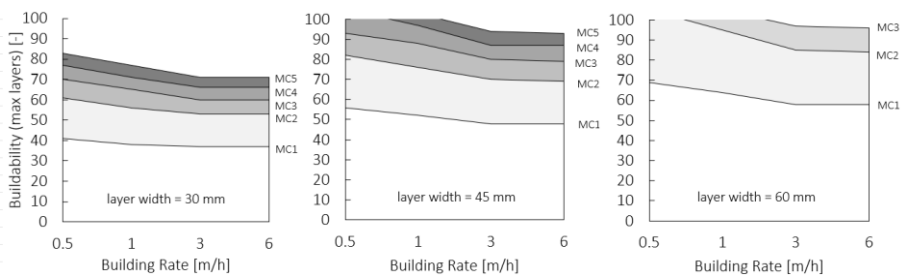


Figure 2-51: Buildability domains based on the Master Curves plotted in Figure 2-50

2.2.4 Conclusion

Printable cementitious mortars typically used in the layered extrusion process behave as viscoelastic material: generally, this means that the mechanical

response to an external stimulus (i.e., imposed strain or load) cannot be completely instantaneous, but part of it can be delayed. At each step of the deposition process, the single layer is subjected to a constant vertical stress increment. Hence, according to the theoretical creep response, the material exhibits both an instantaneous and a viscous vertical strain in its early age (which approximately corresponds to the printing time). In detail, the viscous strain component at an early age develops quickly, and it could be a significant percentage of the overall vertical strain as it accumulates over time. Consequently, for tall structures, a proper investigation of such phenomenon becomes more important, especially during the printing process. Therefore, an accurate prediction of the vertical strain is useful to calibrate the robotics motion and the dimensional/quality control.

Moreover, another critical experimental challenge is the hardening of the cement paste: it is necessary to develop a reliable viscoelastic constitutive model accounting for this phenomenon. In this context, the Burgers' model could represent a satisfactory way to model the creep strain response over time of the early-age material, considering both mechanical and viscous material properties. The Burgers' model is defined if the four corresponding parameters are known: since the material hardens at a fresh state, it is necessary to define the Burgers' parameters as a function of the resting time. A good prediction of the total strain depends on the reliability of the material mechanical model obtained by experimental data fitting over time.

Since the temporal evolution of mechanical properties is a new focus in 3DCP, in this section the early-age creep effect was studied through an experimental campaign carried out on two kinds of cementitious printable mortars:

- UniNa mortar: the creep test was carried out at different resting times (0, 15, 30 and 60 minutes). In detail, the loading history was composed of a loading ramp up to a target force value, which was maintained constant in order to record the vertical displacement due to the early-age creep effect.

The testing parameters, i.e., the displacement rate of the first loading branch and the testing duration, were chosen through an iterative process to satisfy the instantaneous load application assumption and the full development of the early-age creep strain. Experimental outcomes, i.e., total strain vs time curves at 0, 15, 30 and 60 minutes, were used to calibrate the Burgers' analytical model: a time-dependent law was achieved for each parameter. The time-dependent law of the Maxwell stiffness has a good match with the elastic secant modulus obtained in [76]. Validation of the calibrated model was achieved through further experimental tests that simulate the step-by-step deposition process: the analytical model provides a good prediction on the long-term strain, where the differences fall within the experimental scatter.

- Italcementi mortar: cylindrical specimens were subject to a step-wise loading history reproducing the stress state of the first layer during the printing. This kind of test is more flexible and allows replicating every printing condition (e.g. interlayer time and filament weight). The experimental outcomes were successively used to calibrate the analytical Burgers model through a numerical algorithm implemented in Matlab. The Burgers model allowed satisfactorily predicting the cylindrical specimens' vertical strain tested with three different loading rates. However, the error is assumed to increase if the loading rate is further away from the investigated range. In that sense, the Burger model calibration could be improved by adopting more complex functions for the four parameters. Indeed, the evolving over time of the parameters should better model the changes in the material properties due to curing at a very early age.

An SR-dependent Burgers model was also calibrated to improve the experimental data fitting strongly. This model was successively used to estimate an equivalent stiffness of elements during printing and the self-buckling collapse. Finally, the analytical failure prediction was validated through experimental buildability tests.

Based on the calculations, Burger's model tends to be a helpful tool to evaluate the overall vertical displacement of a 3D printed element. With such model it is possible to predict the self-buckling collapse during the printing. In this sense, the equivalent Burgers stiffness and the correlated buildability domains could be a helpful tool to predict the buildability of a new printable mortar helping the standardisation of such requirement. The diversification in 3D concrete printing technologies (e.g., building rates, time gap, pressure during extrusion, nozzle characteristics) has to be considered in future research: the fabrication of full-scale 3D concrete printed objects, equipping setup with optic measurement tools to improve the accuracy of the results, should provide data useful to validate the employment of the Burgers' model and the early-age creep quantification.

3. Reinforced printed elements: approach and characterisation

3DCP offers the advantages of eliminating the necessity of formworks to produce structural and non-structural elements bringing several advantages. However, this technology must face some challenges, mainly linked to the limited knowledge in areas such as incorporating reinforcement in structural concrete members.

Cementitious materials have a quasi-brittle mechanical response and low tensile strength. Therefore, these materials are traditionally combined with reinforcement resisting the tensile forces to produce load-bearing structures showing a ductile response. However, for 3DCP, this inclusion of reinforcement is not straightforward due to the layered manufacturing process. A wide range of reinforcement strategies for DFC has been developed and explored over the recent years [1, 26–28], but in 3DCP, two types of reinforcement are typically adopted: conventional reinforcing bars (e.g. [30]) and flexible filaments, such as carbon filaments [83] or steel wires [84]. The mechanical performance of this reinforcement depends on the amount of reinforcement added to the element and the bond between the reinforcement and the surrounding concrete.

Pull-out tests are the most frequent method to assess the bond strength of bars in conventionally cast concrete. Those tests usually follow the RILEM recommendation [85], consisting of a single bar pulled from an uncracked cubic concrete specimen (for bars of at least 10 mm, the embedment and side lengths are five and twenty times the diameter of the bar, respectively). Such tests provide a result of the bond strength under standard conditions that allows

comparing concrete and reinforcement with different mechanical properties, bars with varying rib geometries and different levels of compaction.

The evaluation and standardisation of the bond behaviour pose many challenges in 3DCP since it is necessary to consider the particularities induced by this novel fabrication method. Indeed, there are many differences with respect to conventional concrete that may affect the resulting bond performances: (i) composition of the printable cementitious materials usually employed (which are characterised by the small aggregate and admixtures to ensure the printability requirement), (ii) anisotropy (due to the concrete layer interfaces which could represent a source of weakness depending on the time gap), (iii) specific printing parameters adopted (e.g. nozzle speed, material flow), (iii) used reinforcement which could differ from the traditional one to meet the specific requirement of the 3D printing process.

For interlayer reinforcement with conventional reinforcing bars manually placed between adjacent layers, Baz et al. [86, 87] performed various pull-out tests on reinforcing bars with a diameter of 8 mm with different material and printing parameters. They investigated the effect of varying workability (i.e. change in superplasticiser content and water to binder ratio) and the fabrication method (i.e. casting, parallel and perpendicular printing). For the pull-out tests, small samples were printed, and later, another mortar was cast around the specimens as confinement to produce the testing cubes. The bars were pulled out with an embedment length of 8 cm [86] or 4 cm [87]. In the first study [86], no influence on the bond behaviour by the workability or production method was found. However, in the second [87], a slight decrease in the bond strength from 18.7 MPa for cast specimens to 16.2 MPa (i.e. 13%) for parallel printed and to 14.5 MPa (i.e. 22 %) for perpendicular printed specimens could be observed.

The bond behaviour between steel bars (with a diameter of 10 mm) and 3D printed concrete was also studied by Ding et al. [88]. The research focuses on

the effect of the fabrication method (i.e. casting, parallel and perpendicular printing), steel bar anchorage length (four, six and eight times the bar diameter), and incorporation of recycled sand and fibres. In this study, the specimens were fully printed, and the reinforcement was manually placed. Before the test, the loading surface of the specimens was levelled with high-strength gypsum to ensure a uniform stress distribution. The experimental outcomes showed that the bond strength of the 3D printed specimen was lower than that of the mould-cast specimen, especially for the specimen the reinforcing bar placed perpendicular to the printing path. Additionally, this study reveals that if a sufficient anchorage length is ensured, its increase does not significantly improve the pull-out load for the 3D printed concrete specimens.

A further study on the pull-out behaviour of such a reinforcement approach was performed by Sun et al. [89]. They investigated the pull-out behaviour of BFRP bars placed between the printed concrete layers in different directions. They also observed the degradation of the bond due to printing.

In the mentioned studies [86–89], the bond behaviour of reinforcing bars in 3D printed specimens was investigated through pull-out tests. The authors first faced difficulty getting representative 3D printed specimens. The pull-out samples were partially printed in [86, 87] and successively confined with an additional mortar casting to ensure good confinement of the printed segment and favour pull-out failure of the bar to exclusively quantify the bond (avoiding the splitting collapse of the concrete cube). Instead, the specimens were fully printed in [88] and successively levelled with the gypsum to ensure flat loading surfaces. Another solution was presented in [89], in which the specimens were entirely printed and successively cut into cubes. Another critical aspect is the time gap to place reinforcement and print above it. In [86, 87], the reinforcement was placed within the time gap between two consecutive layers, while there are no details on this aspect in [88, 89]. An important aspect that should also be addressed in the literature is the influence of the chosen printing strategy. Generally, two approaches exist for 3DCP: (i) the use of a high yield

stress mortar and (ii) a set on-demand system with accelerated hydration. The influence of these two approaches on the bond strength is therefore investigated in the presented study. Since there are not yet standardised procedures in the 3DCP production process, the entire evaluation of the bond behaviour, including the specimen preparation and the reinforcement incorporation, is strongly influenced by the printing parameters (printing setup, material, print path, print speed, print geometry etc.). In this framework, interlaboratory studies are needed to investigate such influence, comparing the experimental outcomes with the aim to help the standardisation of testing procedures.

3.1 Interlaboratory study: UniNa and ETHZ

Existing research on the bond behaviour of 3DCP is limited. Moreover, the influence of the printing system is unknown since previous studies used different reinforcements and testing procedures for the same printing set-up. This Chapter discusses the results of an interlaboratory study on the bond behaviour of steel reinforcing bar embedded between 3DCP mortar layers using two different printing systems. The bond behaviour when using a printing system with a stiff and thixotropic mortar (at the Department of Structures for Engineering and Architecture at the University of Naples Federico II in Italy, UniNa) is compared to the one using a set on-demand system [90] (at the Institute of Structural Engineering at ETH Zurich in Switzerland, ETHZ). Three fabrication methods were studied at each institution: casting, parallel and perpendicular printing. Identical reinforcement, printing parameters and testing procedures were employed to ensure consistency among the two institutions. The testing consisted of pull-out tests following the RILEM recommendations [19]. The printed specimens were 3D printed inside formworks to ensure planar surfaces. In contrast to previous studies [86–88], each specimen was entirely produced with the same method and material to capture the splitting behaviour of the printed concrete.

This interlaboratory study provides insights into the opportunities and challenges of standardising methods to measure the bond strength for reinforcement placed between the layers and addresses various critical points for a successful implementation of interlaboratory studies in the field of 3DCP.

3.2 Materials and Methods

Overview

The experimental campaign consisted of 30 pull-out tests (15 tests in each institute) performed by varying (i) the specimen fabrication method (cast (C) and 3D printing (3D).) and (ii) the relative orientation between the printed layer and the reinforcement (parallel and perpendicular). Each pull-out specimen was prepared according to the RILEM recommendations [85]. However, the specimens' size and the bonded length value was slightly adapted (i.e. reduced bond length for the reinforcing bars). In detail, the specimens had a cubic shape with a side length of 200 mm. As mentioned above, two different types of printable cementitious materials were used. A reinforcing bar with a diameter of 8 mm was placed in the centre of the cube with a bonded length l_b of four times the diameter. The embedment length of the bar was selected sufficiently large to have representative results, but its value was limited to avoid the reinforcement yielding:

$$l_b \leq \frac{f_{i,y} \cdot A_i}{\tau_b \cdot \pi \cdot \Phi_i} = \frac{f_{i,y} \cdot \Phi_i}{4 \cdot \tau_b}$$

Equation 45

where $f_{i,y}$ is the yielding stress of the reinforcement i , A_i is the cross-sectional area, τ_b is the value of the bond strength and Φ_i is the diameter. Since the bond strength was unknown at this stage, its estimation was achieved through a pilot-testing series. The reinforcement material was shipped from one institute to the other to ensure consistency.

Reference cast specimens were prepared by filling a mould with the material coming off the nozzle. Printing inside a formwork was employed to prepare 3DCP pull-out specimens: this allowed smooth surfaces for testing and controlled sizes and geometries. For the 3DCP specimens, two reinforcement configurations were adopted: (i) in the parallel configuration (3D \parallel), the reinforcement was aligned with the printing direction, whereas (ii) for the perpendicular configuration (3D \perp), the reinforcement was placed perpendicular to the printing direction. For each fabrication method, five specimens were produced to provide a representative set. A total of fifteen cubic specimens for each institute were prepared in a single printing session. For the printing material characterisation, six cylinders were filled during the printing session, with the extruded mortar and without applying any compaction and tested under compression and indirect tension. The tests were performed after 28 days and for each specimen, the force and slip were recorded. From one of the five tested specimens for each fabrication method, small prisms (4x4x16 cm) were cut out to perform additional material characterisations, including the layering effect. For these tests, two additional specimens of both 3D printed configurations with reinforcing bars were produced to compare the results between tested and untested specimens. Furthermore, some specimens with reinforcing bars were cut along the bar and through the cross-section to visually inspect the interface between steel and concrete. An overview of the test matrix is given in Table 3-1.

Table 3-1: Test matrix

Institute	Reinforcement	Fabrication	Layer orientation	Nomenclature	# Pull out specimens	# Prisms cut out from	
						tested specimens	untested specimens
N	R	C	-	N-R-C	5	3	-
Z				Z-R-C	5	3	-
N		3D	Parallel	N-R-3D \parallel	5	3	3
Z				Z-R-3D \parallel	5	3	3
N		3D	Perpendicular	N-R-3D \perp	5	3	3
Z				Z-R-3D \perp	5	-	3

Printable cementitious mortars

A cement-based material should satisfy pumpability, extrudability and buildability requirements to meet the critical prerequisites of a freeform construction process [46]. The mix design in the 3DCP application is outlined to obtain a cementitious mortar characterised by specific mechanical and rheological parameters [49, 91]. There are two kinds of cementitious materials usually adopted in 3DCP applications: mortars with low or high initial yield stress. A set on-demand [90] process is characterised by the use of a material with a low initial yield strength facilitating extrudability and pumpability but limiting buildability. Therefore, the concrete is usually mixed with an accelerator agent right before the extrusion. As a result, the setting and hardening of a retarded batch are accelerated and controlled by adjusting the admixture amount. The other material approach is designed with a sufficient yield strength to ensure a high enough buildability without additional admixtures, but not too high to simultaneously guarantee a good pumpability and extrudability.

The cementitious mortars employed in this experimental campaign were developed by Italcementi-HeidelbergCement for UniNa and internally developed at ETHZ, satisfying all printability requirements. The UniNa cement-based material is a high yield stress mortar, whereas the ETHZ mortar is controlled by set on-demand. More in detail, the material used at University of Naples is the i.tech NF mortar, already introduced in the previous chapter. In this chapter, such material will be denoted as *UniNa NF*.

The printable material's hardened properties were measured through three uniaxial compressive tests (EN 12390-3:2009) and three splitting tests (ASTM C 496-96, Brazilian tests) after 28 days. Therefore, six cylinders with a diameter of 150 mm and a height of 300 mm were cast with the extruded material for each printing session (see Table 3-2) without applying any compaction. Table 3-2 illustrates the average values of the compressive f_c and tensile f_{ct} strength of

the printing materials adopted in this study. Note that the ETHZ mortar showed higher compressive strength value. Such difference has to be taken into account for the pull-out test results interpretation since the compressive strength affect the bond resistant mechanism [92].

Table 3-2: Overview of the mechanical characterisation at 28 days of the two mortars.

Laboratory	f_c [MPa] (dev.st)	f_{ct} [MPa] (dev.st)
UniNa	40.1 (4.5)	2.9 (0.5)
ETHZ	56.3 (1.2)	2.7 (0.7)

In addition to the concrete material tests on the hardened printable material on cast cylinders, small prisms (4x4x16 cm) were cut from tested and untested pull-out specimens. These tests allow studying the influence of the layered production on the mechanical properties of the mortar. The cut prisms are shown in Figure 3-1.a for a 3D printed specimen. Three-point bending and compression tests [93] were carried out on the prisms to quantify the flexural and compressive strength (Figure 3-1.b). The bending tests of printed specimens were tested with the loading direction parallel to layer interfaces (as shown in Figure 3-1.b), with the interface with the longest interval time (i.e. where the reinforcement was placed) being located at midspan. Therefore, the resultant flexural strength is representative of the middle section of the specimen, which is assumed to be the weakest one.

In addition to extracting samples from tested pull-out specimens, a set of 3D printed pull-out specimens with reinforcing bars was prepared and reserved to cut samples without testing. This set of specimens was used to evaluate the influence of the pull-out testing on the middle interface and study the steel-concrete interface in an undamaged state. The comparison between tested and untested samples investigated whether the reduced bending strength in the middle interface was due to its longest time gap or due to possible cracking developed during the pull-out test.

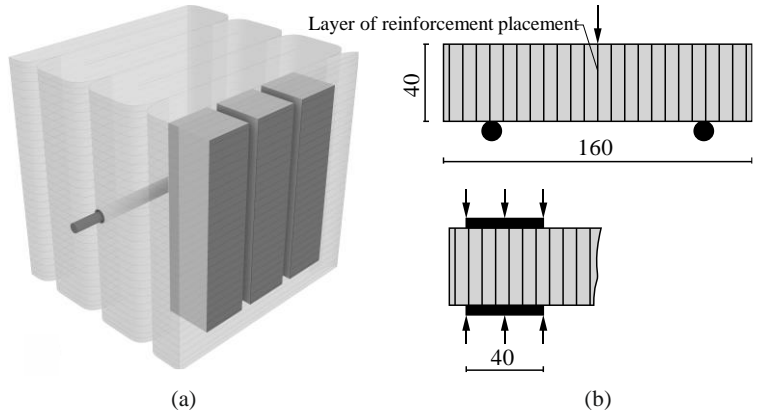


Figure 3-1: Prisms for material tests cut from the specimens: (a) illustration of three prisms cut out of one specimen (exemplary for the parallel printing configuration); (b) testing set up ("EN 196-1" 2016).

Steel reinforcement

Steel reinforcing bars were employed to reinforce the specimens between printed concrete layers. The steel bars had a diameter of 8 mm and a relative rib area (i.e. rib index) of 0.078. The reinforcing bars had a thread at the end to allow anchorage for the pull-out process. The reinforcement properties were obtained by direct tension tests on three samples, and the resulting stress-strain curves and values are shown in Figure 3-2. For the reinforcing bar, the dynamic yield stress ($f_{s,y}$) was 529 MPa with a yielding strain ($\epsilon_{s,y}$) of 2.8 ‰. On average, the ultimate stress ($f_{s,u}$) of 634 MPa was reached at a strain ($\epsilon_{s,u}$) of 79.8 ‰.

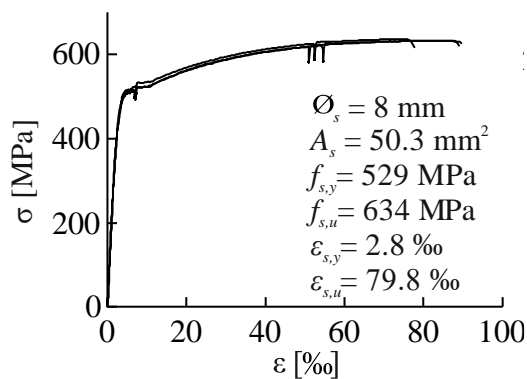


Figure 3-2: Stress-strain relationship of the steel bar.

3.3 Specimens layout and production

Following the RILEM guidelines [85], part of the reinforcement was isolated to ensure bond only over a specific length. In detail, pipes with an outer diameter of 12 mm and an inner diameter of 10 mm were used. The bond length was set at 32 mm (i.e., four times the diameter). In the RILEM recommendation, a length of five times the diameter is proposed. However, a pilot test series has shown that with five diameters, the reinforcing bars yield before being pulled out.

Two types of printing systems were used to produce the pull-out specimens. At ETHZ, a continuous mixer premixed the material to pump it until the nozzle attached to an ABB robotic arm. The accelerator was added to the mortar at the nozzle (see Figure 3-3.a). A scheme of the 3DCP production area can be found in [94]. The system at UniNa consisted of an "m-tec duo mix 2000" pump with integrated mixing. From this pump, the material was delivered to the nozzle and extruded. As a printing platform, an ABB robotic arm was used (see Figure 3-3.b). At both institutes, the length of the nozzle was larger than 200 mm to allow printing inside the formwork.

(a)



(b)



Figure 3-3: 3D concrete printing setups including the pumping system: (a) ETHZ; (b) UniNa

Two fabrication methods (i.e., casting and parallel/perpendicular printing) were used to fabricate the specimens. For the cast specimens, the reinforcement and the isolation were arranged inside formwork before pouring the material coming from the nozzle.

For the printed specimens, the sequence of production and the printing paths can be seen in Figure 3-4 and Figure 3-5. A different value of the linear printing speed was adopted at ETHZ and at UniNa (i.e. on average 80 mm/s and 240 mm/s, respectively) due to the different pumping systems and flow rates. After 10 cm, the printing was stopped, and the reinforcement was manually added (Figure 3-4.b). The formworks had large holes on both sides, with the lower edge of the holes ensuring that the reinforcement would be placed at the centre of the cubes. These holes ensured that the reinforcement could be added with minimal interference with the concrete, ensuring a horizontal and correct reinforcement position. The time to place the reinforcement was set as 5.5

minutes for both institutes. This time interval was chosen to allow enough time to place the reinforcement and simulate the fabrication of a larger structure. After the reinforcement was placed, the next 10 cm were printed to reach the final height of 20 cm. Small gaps between the formwork on the sides allowed to cut the printed object into cubes right after production (Figure 3-4.c). It was necessary to perform multiple cuts during the printing for the accelerated mix due to the fast-hardening material. The specimens were covered with a plastic sheet and left for curing and tested after 28 days.

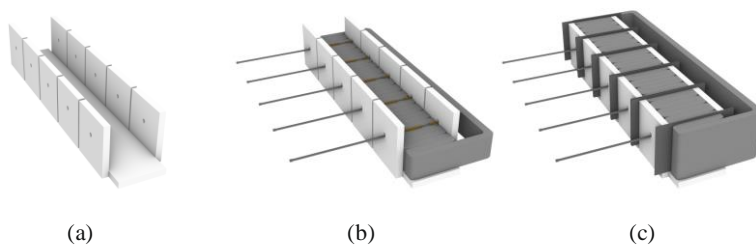


Figure 3-4: Specimen preparation for the parallel printing configuration with reinforcing bars: (a) Placement of the formwork; (b) Printing of the first 10 cm and placement of the reinforcing bars; (c) Printing of the remaining 10 cm and cutting of the specimens and cutting.

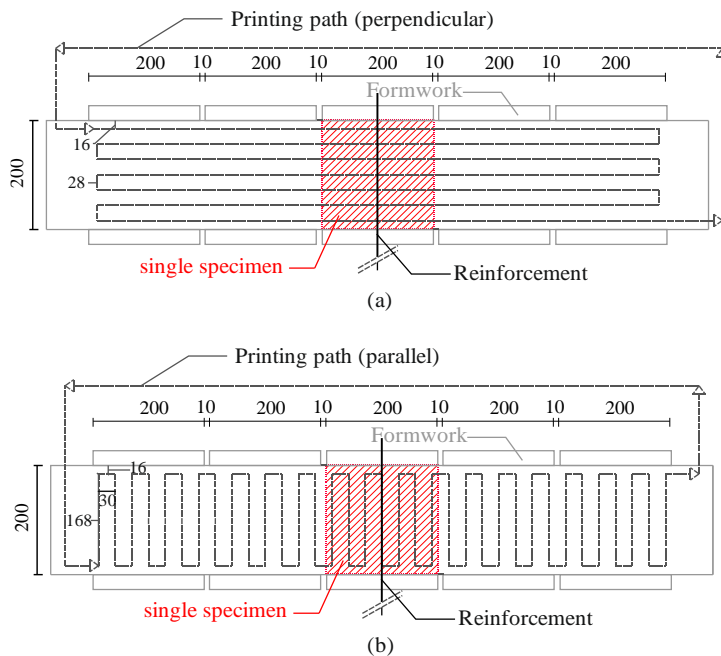


Figure 3-5: Printing path of the various configurations: (a) parallel printing path; (b) perpendicular printing path

In Figure 3-6, the printing process for all configurations after the reinforcement placement can be seen. Minor variations in the material consistency and, hence, the flow rate, together with the formwork restrains, produced some material accumulation.

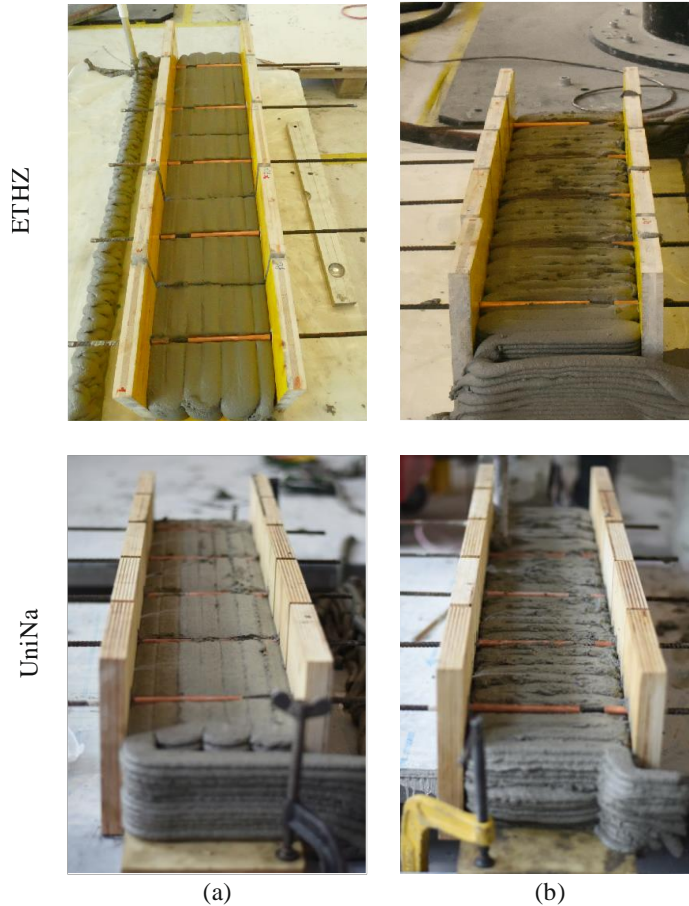


Figure 3-6: Images from the production of the samples: (a) Printing of specimens with reinforcing bars with the perpendicular configuration; (b) Printing of specimens with reinforcing bars with the parallel configuration.

3.4 Pull-out Testing

Pull-out tests were carried out on printed and cast specimens after 28 days from production in both laboratories. Figure 3-7 shows the scheme of the testing setup and the corresponding pictures from both institutes. A neoprene layer

At ETHZ, pull-out tests were carried out with a "Zwick Roell 1484" electromechanical universal testing machine with a 200kN capacity in a displacement-control condition. At UniNa, a universal testing machine, "MTS 810", with a capacity of 500 kN, was used. In both laboratories, a displacement rate of 0.6 mm/min was adopted. The bond stress was evaluated as the ratio between the pull-out force F and the nominal contact surface.

3.5 Results and Discussion

3.5.1 Overview

Table 3-3 and Figure 3-8 give an overview of the pull-out test results with the average maximum values ($\tau_{b,max}$, F_{max} and the coefficient of variation (CoV)).

Table 3-3: Overview of pull-out testing results.

Codification	N-R-C	Z-R-C	N-R-3D	Z-R-3D	N-R-3D⊥	Z-R-3D⊥
$\tau_{b,max}$ [MPa]	19.3	29.7	15.4	30.0	18.8	30.6
(CoV)	(12%)	(4%)	(31%)	(15%)	(13%)	(7%)

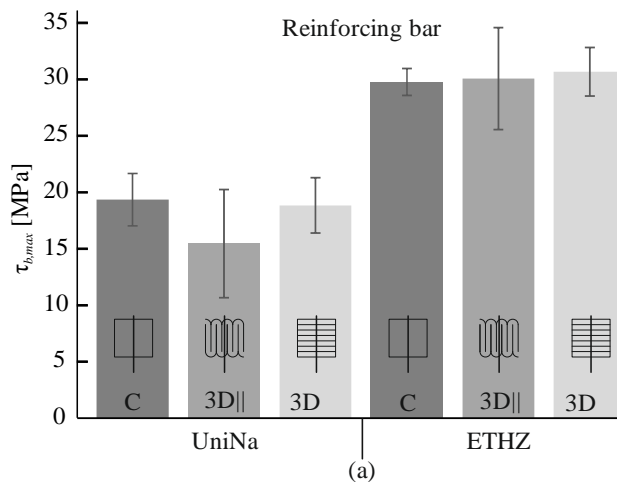


Figure 3-8: Bar plot showing all max stresses of all tests next to each other

The average bond strength ranged from 29.7 to 30.6 MPa and from 15.4 to 19.3 MPa, for the ETHZ and UniNa printing system/material, respectively. More in

detail, at ETHZ, the difference in the bond strength between cast and printed (in both configurations) specimens was contained in the experimental scatter. At UniNa, a reduction of bond strength of approximately 25% was detected between cast and parallel printed specimens. However, such a reduction might be attributed to the higher experimental scatter in the parallel printed set (i.e. CoV=31%). Whereas in the perpendicular configuration, this reduction drops to a negligible value of around 2%.

3.5.2 Bond-slip behaviour

Figure 3-9 illustrates the slip vs bond stress response for each configuration of the pull-out specimens. The black curves show the average result, while the light grey curves depict the outcome of each sample. All configurations exhibited the same overall behaviour characteristic of pull-out tests: an initial activation phase with a minimal slip until the peak bond stress is reached, followed by a phase in which the bar is pulled out from the surrounding mortar with increasing slip and decreasing resistance (i.e. softening).

There seems to be no influence of the fabrication method on the overall pull-out behaviour. However, the scatter of the samples produced by 3D printing was higher than for the cast specimens, particularly when the reinforcement was provided parallel to the printing direction.

One important factor influencing the scatter might be correlated to the manual placing of the reinforcing bar during the printing process. Furthermore, the effective contact surface between the bar and the surrounding mortar could be different, especially for the UniNa material characterised by initial higher yield stress which could reduce the reinforcement covering. On the contrary the high fluidity of the set on-demand ETHZ material probably helped the more homogeneous reinforcing bar covering. This material property seems to have more influence in the parallel configuration, for which the UniNa outcomes revealed the higher scatter.

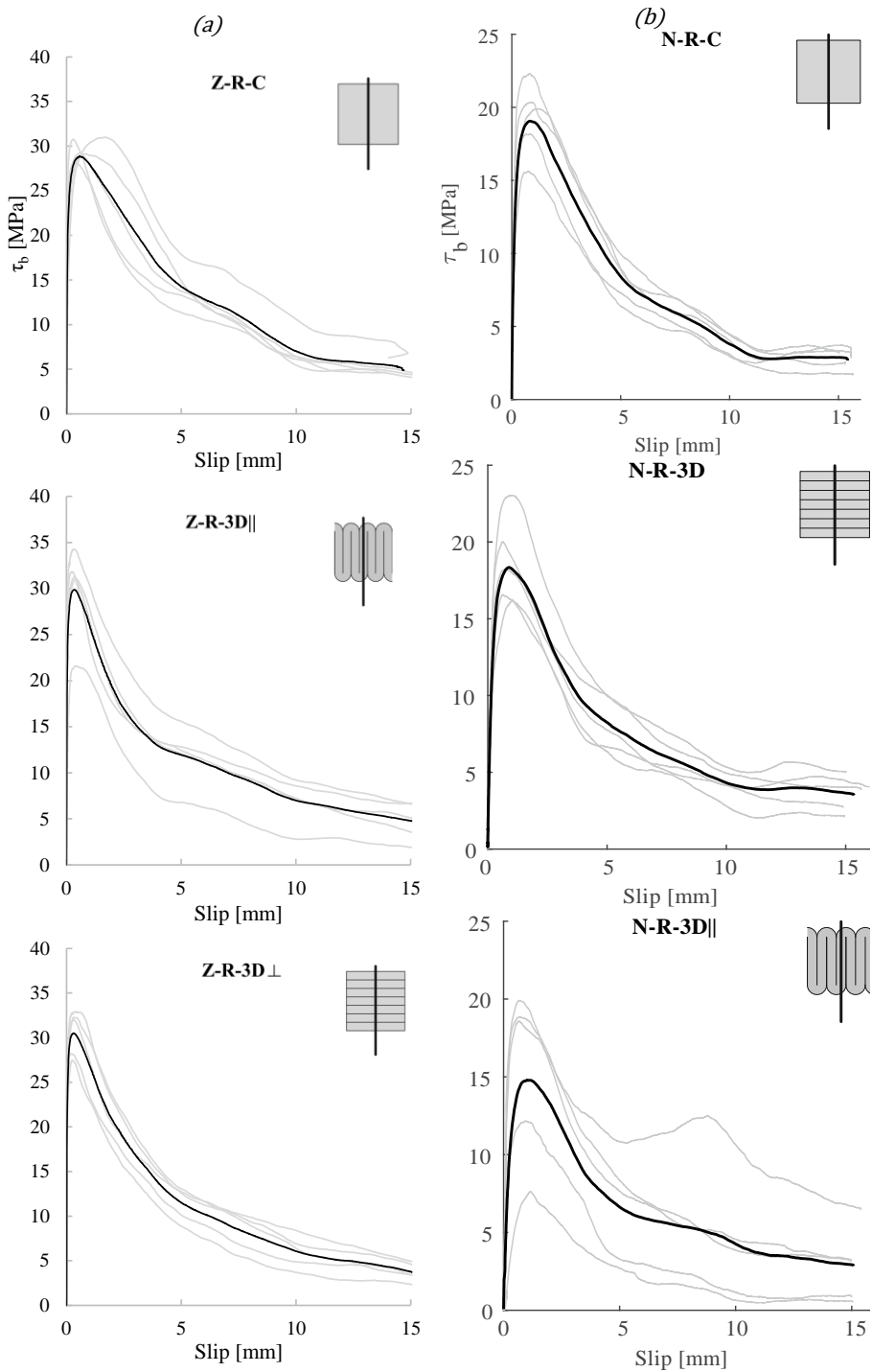


Figure 3-9: Pull-out behaviour: (a) Cast specimens; (b) 3D printed specimens with the perpendicular configuration; (c) 3D printed specimens with the parallel configuration.

A visual inspection of the interface between the concrete and the reinforcing bar was achieved by cutting through the untested specimens (i.e., longitudinal section I and transversal section II in Figure 3-10). The contact surface between the steel and the mortar is detectable in Figure 3-10: in both parallel and perpendicular configuration, the printing process ensures a good interface for the bond performance since there are no visible voids or defects.

Moreover, the cut along the reinforcing bar in tested specimens reported in Figure 3-11) allowed observing the pull-out failure: the system failed by shearing along the surface at the top of the ribs. Indeed, in tested specimens, the slip is almost entirely due to crushing or shearing of the mortar at the ribs (Figure 3-11). Furthermore, the ultimate tensile stress was not exceeded by the splitting stress generated by the bond since there are no internal cracks, contrary to the observations in available experimental studies performed on traditional reinforced concrete [95].

The local failure of the bond with no cracking of the surrounding concrete indicates that the observed pull-out behaviour might be mainly traced back to the composition of the concrete and the reinforcing bar size. Dominant factors for this behaviour might be the maximum aggregate size and the chosen reinforcing bar diameter. For mortars, generally used for 3D concrete printing, the maximum aggregate size is typically smaller or equal to 2 mm, and the used reinforcing bars during the printing process have a small diameter. Therefore, the small aggregates in combination with small rib heights might facilitate the observed shearing behaviour. A similar situation was observed by Bazant and Sener [36] in a study on size effect. For the smallest reinforcing bar diameter of 2.9 mm, shearing was observed, while for diameters 6.4 and 12.7 mm, splitting of the sample occurred for concrete with a maximum aggregate size of 3.35 mm.

This influence of the aggregate size and reinforcing bar diameter in combination with the limited influence of the fabrication method indicates that

the bonding behaviour and failure mode of reinforcing bars for 3D concrete printed elements might be determined by the material behaviour, maximum aggregate size and reinforcing bar diameter and not the production method. Further testing would be necessary to verify this observation.

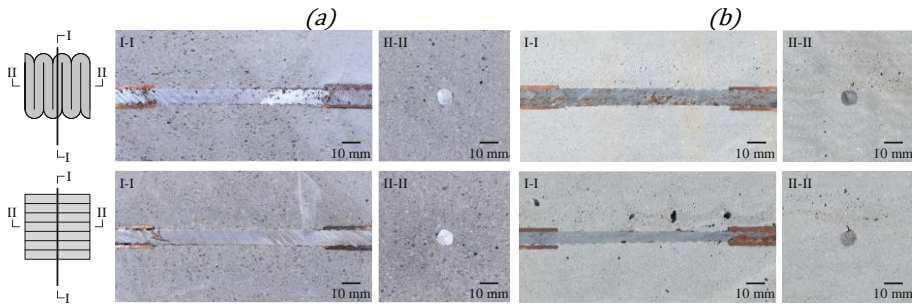


Figure 3-10: Sections through the reinforcing bar in untested specimens (top: parallel configuration; bottom: perpendicular configuration): (a) UniNa; (b) ETHZ

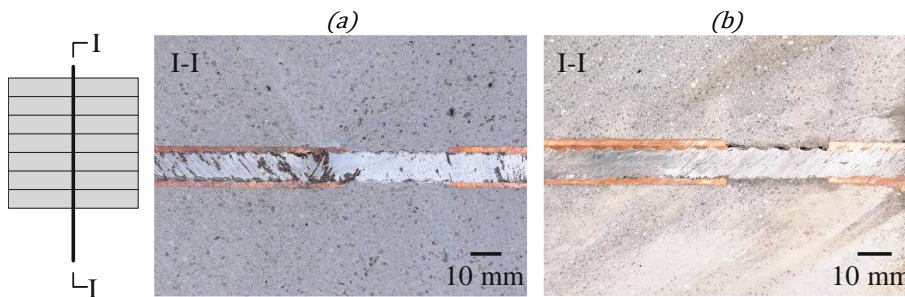


Figure 3-11: Sections through the reinforcing bar in tested specimens (perpendicular configuration): (a) UniNa; (b) ETHZ.

3.5.3 Comparison with Model Code 2010 and existing literature

The prediction of the steel-concrete bond behaviour is essential to design the bar anchorage length and overlapping of reinforcing bars in the structural elements [96, 97]. For traditional reinforced structures, many experimental data and bond models are available in the existing literature [96–98].

The bond stress design value τ_{bd} is usually estimated by means of equation provided in EN 1992 and Model Code 2010 [92, 96]. With the aim of comparing the bond behaviour of traditional reinforced concrete and the reinforced printable mortars, the average stress-slip relationship experimentally obtained

in this study for the two materials investigated in the two institutions (continuous black curves in Figure 3-12) was compared with the analytical laws provided in the *fib* Model Code 2010 [92] for good bond condition and pull-out failure (red continuous curves in Figure 3-12).

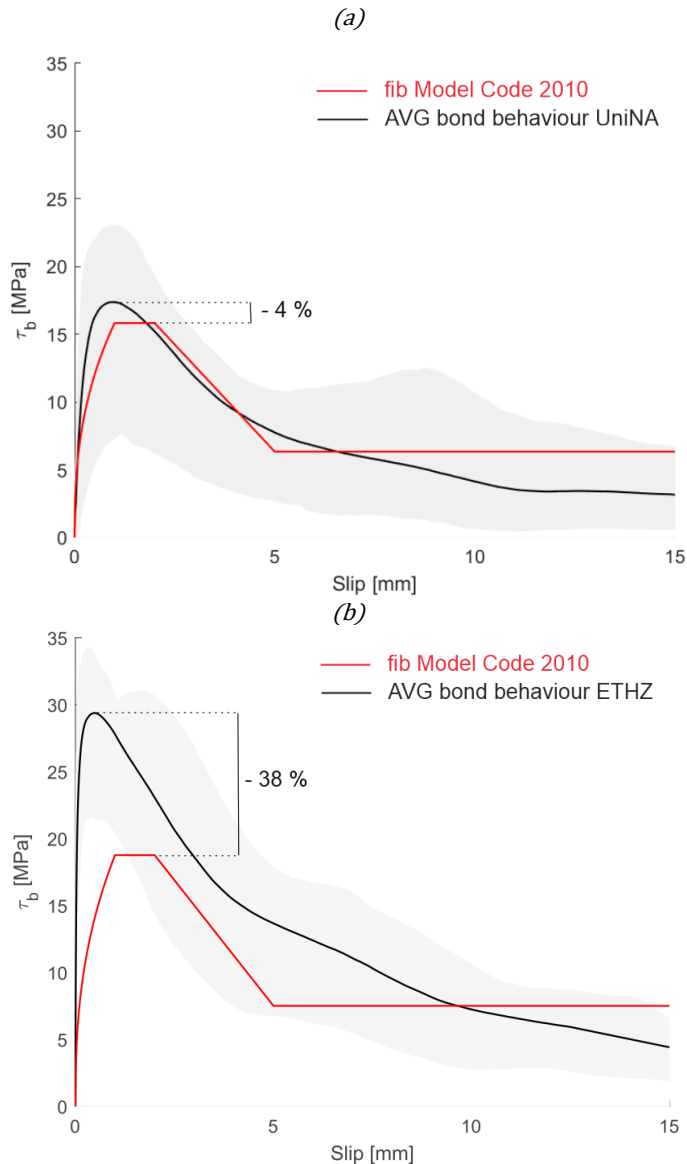


Figure 3-12: Analytical [92] vs experimental bond stress-slip relationship: (a) UniNa and (b) ETHZ.

The *fib* Model Code provides a reasonable estimation of the bond strength for UniNa, with a percentage difference of 4% of the maximum bond strength;

additionally, the analytical law is contained in the experimental scatter (see the grey area in Figure 3-12.a). On the contrary, the Model Code strongly underestimates the bond strength for ETHZ by 38%. From the phenomenological point of view, as also previously discussed, the higher bond strength observed at ETHZ compared to the value of UniNa was probably and mostly due to the higher compressive strength of the 3D printable mortar adopted. For such reason, the empirical correlation between the bond and the compressive strength of both ETHZ and UniNa is compared in Figure 3-13 with to the experimental pull-out testing results discussed in [99, 100] and [88] (for conventional concrete and 3D printable mortar, respectively) to investigate such dependency better. Furthermore, the compressive strength influence is well-documented in the available literature [92] since the maximum bond stress depends on the square root of the characteristic value of the cylindrical compressive strength (see Table 6.1-2 in [92]). Hence, Figure 3-13 also portrays the analytical laws suggested by the Model Code 2010 (in good and all other bond conditions) that correctly predict the maximum bond stress observed in [99] and [100] for conventional concrete. It is possible to observe that the analytical relation proposed in the Model Code 2010 (red dashed lines in Figure 3-13) underestimates the maximum bond stress related to the 3D printable mortar for both cast and printed specimens (see the square and cross markers in Figure 3-13, respectively). This finding means that such underestimation is probably linked to (i) the difference in the cementitious formulation of printable materials with respect to the conventional concrete (e.g. aggregate size, cement content) and (ii) the small bar diameter employment, rather than the fabrication method itself (cast vs 3D printed). It is worth noting that the inverse correlation between the bond strength and the bar diameter (point (ii) above) complies with the code [101] and experimental data discussed by Arel et al. [100]. Some additional positive effects could also be related to the lower viscosity of the ETHZ accelerated mix, which more homogeneously surrounds the bar.

The comparison between bond strength in 3D printing application and conventional concrete demonstrates that the bond developed by placing reinforcement bars between the layers of printed concrete results in a better bond than conventional reinforced concrete. A possible correlation between the maximum bond stress and the compressive strength is represented in Figure 3-13 (see black dashed line). However, for larger slip values, the residual bond strength of the printed systems is overestimated by the analytical model (see Figure 3-12) and should be addressed by further research.

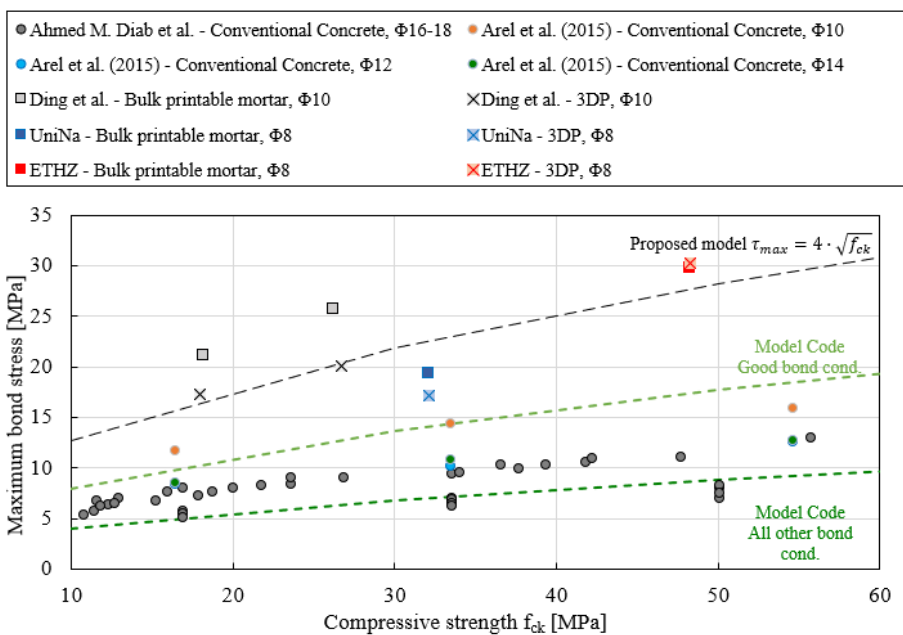


Figure 3-13: Experimental correlations between compressive and bond strength and estimated values from the codes [97].

3.5.4 Hardened properties from cut printed samples

The experimental results are shown in Table 3-4 . In some cases, the pull-out tested specimen cracked before or during the cutting and no specimens were obtained (i.e. Z-R-3D⊥ of Table 3-4). From Table 3-4, it is possible to observe that ETHZ mortar provided higher compressive as well as flexural strength, confirming the experimental results on cast cylinders previously discussed (see Table 3-2). Both at UniNa and ETHZ, the difference in flexural strength

between tested and untested specimens can be considered negligible. Hence, the activation of the bond between the reinforcing bar and the concrete does not seem to influence the tensile strength between layers. On the contrary, a not negligible percentage reduction of 32% and 37% (at UniNa and ETHZ) was assessed in printed specimens compared to the cast ones. The average flexural tensile strength of the specimens from UniNa and ETHZ was 4.5 MPa and 5.9 MPa, respectively.

For the compressive strength, no significant influence of neither printing nor testing could be observed as the differences in strength are contained in the experimental scatter. This observed behaviour of the hardened printed material follows the observations made by other authors [50]. Compared to the cast cylinders the compressive strength increased by 19% at UniNa and 11% at ETHZ, which is in the order of the expected scatter.

Table 3-4: Results of the flexural strength of the prisms cut from the specimens. $f_{ct,fl}$: Tensile strength of the concrete determined with flexural tests, f_c : compressive strength of the concrete

Codification	$f_{ct,fl}$ [MPa]	$f_{ct,fl}$ [MPa]	f_c [MPa]	f_c [MPa]
	(CoV)	(CoV)	(CoV)	(CoV)
Configuration	Tested	Untested	Tested	Untested
N-R-C	4.7	-	51.6	-
	(6%)	-	(5%)	-
Z-R-C	7.9	-	63.1	-
	(16%)	-	(5%)	-
N-R-3D	3.5	4.0	54.5	47.9
	(18%)	(7%)	(4%)	(10%)
Z-R-3D	5.0	6.7	62.2	61.8
	(13%)	(12%)	(8%)	(6%)
N-R-3D⊥	4.1	4.5	53.3	49.2
	(5%)	(6%)	(7%)	(8%)
Z-R-3D⊥	cracked	6.1	cracked	61.6
		(24%)		(3%)

3.6 Proposal for standardisation

This study shows an attempt to standardise a testing method between two institutes to determine the bond strength between 3D concrete printing and reinforcement manually placed between the printed layers.

One decisive factor for the standardisation between both institutes was to print the samples inside a formwork. This approach had the advantages to (i) control the geometry of the specimens and ensure straight surfaces for the load introduction, (ii) control precisely the location of the reinforcement by placing it in a hole in the formwork, (iii) cut the specimen in a fresh state if a small spacing between consecutive formworks is provided and (iv) enable direct comparability between institutes and between printed and cast specimens without factors. However, this formwork also introduced some limitations. For one, the final position of the reinforcement relative to the concrete depended on the material accumulation during printing (see Section 3.3). Furthermore, this approach is limited to the use of non-rotation nozzles with a symmetric opening. For rotating nozzles, the space between the formwork might not be sufficient to fill the formwork properly.

Another aspect of the standardisation relates to the used reinforcement diameter and isolation elements. The RILEM recommendation for pull-out tests [85] prescribes an isolation element with 1 mm tolerance around the bar and a thickness of less than 2 mm only on the side where the bar is pulled. However, for 3D concrete printing, the height of the reinforcing bar and the isolation element that can stand out of the lower printed layer is limited by the chosen layer height and material consistency. Assuming that half of the reinforcement is embedded in the bottom layer, the total diameter of the reinforcing bar and isolation is limited by double the layer height to avoid a collision. For stiffer printable materials, it is difficult to achieve high printing qualities for low layer heights (i.e. below 5 mm), while a larger layer height (i.e. 10 mm and more) is challenging with fluid set-on demand materials. In this study, the layer height

was chosen at 7 mm to allow a high printing quality at both institutes. This layer height limits the reinforcing bar diameter to 8 mm when using an isolation pipe of 2 mm thickness with 1 mm tolerance. The study of the bond behaviour of reinforcing bars of larger diameters would require adjusting the printing parameters. This adjustment might, in turn, affect the bond behaviour, making each experimental campaign's representability difficult.

A final remark should be made about the representability of such a study for automated production. This standardisation allows achieving clear and comparable results. However, for future applications on a large scale, the placement of the reinforcement bars should also be automated. Therefore, it would need to be ensured that the quality of the automated placement is high enough to ensure the same mechanical response as the standardised tests. For this matter, additional tests should be performed to ensure that the standardised specimens correlate with the printed ones.

3.7 Conclusion

An identical experimental campaign was planned and performed in two different laboratories (UniNa and ETHZ) with the aim to investigate the bond behaviour of steel reinforcement in 3D printed concrete elements. In the innovative field of digital fabrication with concrete, interlaboratory studies can be useful in the standardization of the testing procedures, highlighting difficulties, challenges and possible solutions to define a simple and reliable experimental method.

In total, 30 cubic pull-out test specimens reinforced with steel bar (8 mm) were tested in each institute according to the RILEM standard test. Mechanical performances of printed specimens (with different reinforcement orientations) were compared with cast ones. The adopted procedure to prepare specimens (e.g., nozzle shape and size, time gap, printing path, etc.) and the testing method were established as similar as possible in both institutes. To this aim, it was

useful to print entire specimens inside formworks to control shape and size with high precision.

Furthermore, the influence on the bonding effectiveness of the material rheology was analysed. High yield strength mortar was employed at UniNa (i.e. UniNa NF mortar), whereas a set-on-demand cementitious formulation with a significantly lower yield strength was used at ETHZ (i.e. ETHZ mortar).

Testing results showed that the use of reinforcing bars in 3D printing application could be a reliable strategy as reinforcement between the printed layers: at ETHZ, a negligible difference between cast and printed specimens was recorded, while at UniNa, a reduction of approximately 20% was detected between cast and parallel printed specimens. Therefore, the bond strength is high, and its value has a limited influence on the fabrication method (i.e. printing vs cast). The ETHZ specimens generally provided higher bond strength than the UniNa ones, and this is mainly linked to the higher compressive strength and lower viscosity of the set-on-demand mortar employed at ETHZ. The correlation between the bond and compressive strength is widely investigated in literature and in available codes. The correlation experienced at UniNa and ETHZ was compared to the experimental data available in the literature for conventional concrete, resulting in better performances related to 3DCP pull-out testing results. This is probably linked to (i) the difference in the cementitious formulation of printable materials with respect to the conventional concrete (e.g. aggregate size, cement content) and (ii) the small bar diameter employment, rather than the fabrication method itself (cast vs 3D printed).

Furthermore, the bond strength laws provided for conventional concrete by Model Code 2010 underestimate the bonding performance in reinforced printable mortars. Regarding this aspect, a new expression for the bond strength assessment was proposed in this section, modifying the existing one provided by the code.

4. Topology optimised beams

The 3D Concrete Printing (3DCP) technology allows high shape flexibility in structural and architectural elements design. Such an innovative technology makes it possible to reduce the amount of material used [102] by implementing the Topology Optimisation (TO) concept, which could lead to material saving, and then resources, up to 50-60% in the fabrication of structural elements [103, 104]. TO technique can reduce the amount of concrete material by locating it only in the most loaded area of the element and improving the shape effectiveness. As a result, if the boundary conditions (i.e. external loads and constraints) and material mechanical properties are known, the element's topology optimised shape could be adopted to maintain structural requirements.

Several research groups started to work on this topic in the last decade, developing different analytical solutions for the problem and adopting various approaches. Several projects were finalised, demonstrating the feasibility and effectiveness of TO implemented in digitally fabricated concrete structures. For example, a post-tensioned girder (4 m span) was fabricated at Ghent University in 2019 [36]. This project demonstrated the potentiality of the topological design in combination with 3DCP, allowing the creation of efficient structures. TO analysis was also employed by Kinomura et al. [105]. 44 segments with complex shapes were designed to fabricate a reduced scale pedestrian bridge. The elements were separately printed and successively assembled as a compression loaded structure through prestressed external reinforcement.

In this framework, the present chapter contains the experimental application of the TO approach proposed by Pastore et al. [106] (2019, 2021), i.e. by using a curve-based Biased Random-Key Genetic Algorithm that optimises stress-constrained structures and generates topologies that can be implemented without post-processing operations. For more details about the methodological approach of the TO applied to the DFC, please refer to the mentioned works.

The topology optimised concrete beam solutions are obtained starting from a simply supported solid concrete beam loaded in the mid-span. Furthermore, once the printability of the optimised beam was verified, the inclusion of steel bars as reinforcement was also considered. Indeed, in Chapter 3, the effectiveness of small diameter bars in 3D printed cubic specimens was verified through the experimental campaign of pull-out tests. As a result, the same reinforcement strategy was planned for the 3D printed optimised beams. In this way, both unreinforced and reinforced digitally fabricated beams were tested, and their mechanical response is herein discussed.

4.1.1 Theoretical framework and optimisation algorithm

The topology optimisation algorithm was employed to design 3DCP beams with the Italcementi printable mortars i.tech N and NF. Since these materials result in different mechanical properties from the technical data sheet provided by the company, two different optimised shapes will be obtained.

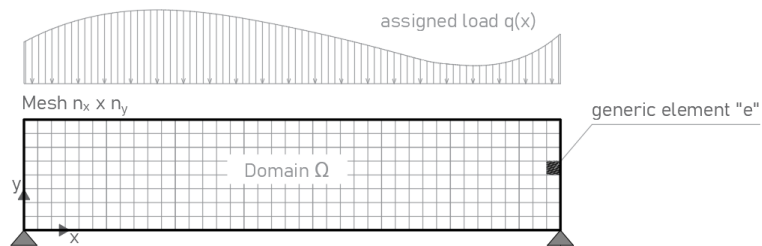


Figure 4-1: Beam domain: representation of the mesh.

According to the approach proposed by Pastore et al. [106], the structural element to optimise can be considered as a domain Ω characterised by a mesh M composed by $n_x \times n_y$ elements; the design variable x_e (as shown in Figure 4-1) represents the density of each element e of the mesh, thus requiring $0 \leq x_e \leq 1$. In this way, the element contributes to the mechanical response if the corresponding value of x_e is equal to 1. On the contrary, when the value is 0 the element is unresponsive.

A finite element analysis provides the global stress tensor expressed in terms of principal stresses with assigned boundary conditions and loads. Two separate bounds are considered for the maximum and minimum values of the principal stresses. In this way, it is possible to control the stresses asymmetrically either in the case of compression (bound on the minimum value) or traction (bound on the maximum value). The topology optimisation approach proposed in [106] minimises the average density of the whole element, taking into account the material compatibility (Equation 4-1).

$$\text{minimisation of the average density} \rightarrow \min \frac{\sum x_E}{N}$$

$$\text{material compatibility} \rightarrow \begin{cases} \sigma_- \leq \sigma_1^e \leq \sigma_+ \\ \sigma_- \leq \sigma_2^e \leq \sigma_+ \end{cases}$$

Equation 4-1

The solution obtained from Equation 4-1 only considers local information without considering the printing path and without ensuring feasibility for a layered extrusion printing process. Consequently, intending to achieve a more technology-ready solution, the used approach (Pastore 2021) was further enhanced and based on curve-based global decision variables. The above optimisation approach includes both mechanical and technological constraints:

- Mechanical constraint (C1): the stress values measured at each element point do not exceed the pre-defined limit associated with the material.
- Two of the leading fabrication limitations related to the specific DFC process here studied (i.e. layered extrusion). The former is the path-continuity constraint that ensures the continuity of the concrete filament (C2). The latter is the size of the nozzle that restrains the extruded layer width to a limited set of values (C3).

The algorithm provides an optimised solution that concatenates a set of Bezier curves compatible with a printing path. Bezier curves are a well-known family of parametric curves; more in detail, given a set of points $P_0 \dots P_n$ (where “n” is the order of the curve, as in Figure 4-2) the corresponding Bezier curve is:

$$\beta(s) = \sum_{i=0}^n \binom{n}{i} \cdot (1-s)^{n-i} \cdot s^i \cdot P_i \quad \text{with } s \in [0,1]$$

Equation 4-2

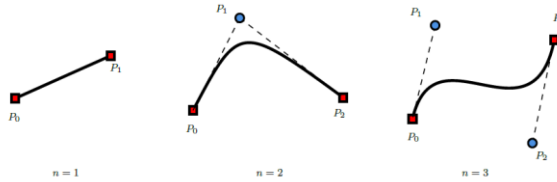


Figure 4-2: Examples of Bezier curves: a) linear; b) quadratic; c) cubic. End-points are denoted as red squares, while control points are blue circles.

Where s is an intrinsic parameter of the curve. The end-points of the curve P_0 and P_n can be obtained for $s = 0$ and $s = 1$, whereas the control points $P_1 \dots P_{n-1}$ do not lie on the curve. Furthermore, the algorithm finds the solution considering the Eulerian Path Problem (EPP) so that the printing path can be drawn tracing each edge only one time (to fulfil the constrain C2). In order to satisfy the constrain C3, each Bezier curve $\beta(s)$ composing the optimised solution is associated with a fixed width δ_i that belongs to a set of the possible diameters of the printing nozzle used for the 3DCP.

Given the solid concrete domain Ω , the kinematic boundary conditions bc and applied loads f , the Bezier based theoretical TO framework is integrated within a problem-specific Biased Random Key Genetic Algorithm (BRKGA) as schematically described in Figure 4-3. More in detail, the BRKGA, initially proposed in [107], is an extension of the Random-Key Genetic Algorithm (RKGA) [108] that uses genetic operators to improve a set of candidate solutions iteratively.

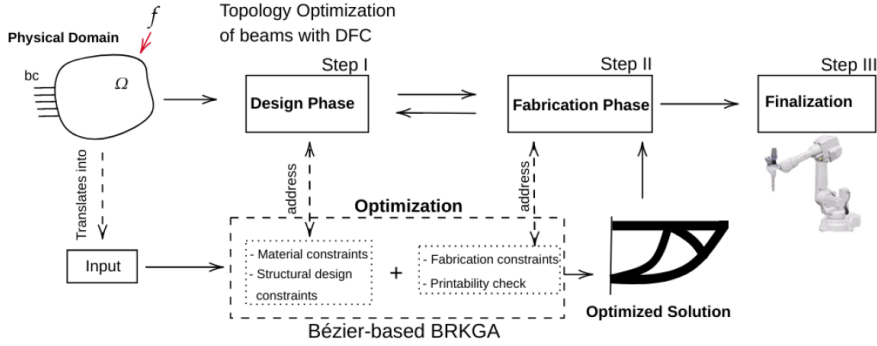


Figure 4-3: General depiction of the solution framework [109]

4.1.2 Beam layout and printing production

The Bézier curves-based approach was employed to optimise a simply-supported reference beam with a rectangular cross-section of 200x300 mm and span length of 1.8 m (Figure 4-4). Once the load was fixed, the algorithm provided an optimised beam shape depending on the material mechanical properties. Indeed, as previously explained, the solution consists of a set of Bézier curves such that the stress is lower than the limit value (i.e. material strength in compression and traction) in each point.

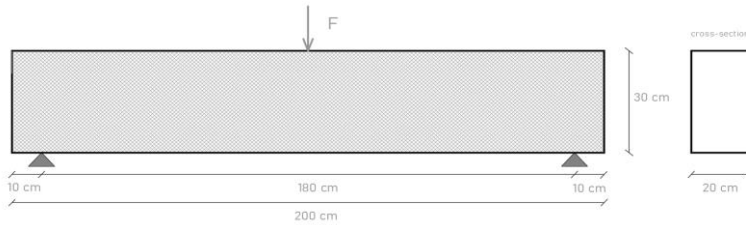


Figure 4-4: Simply-supported reference beam.

The reference (design) load value F , assumed as a vertical force in the midspan, was assessed by imposing the achievement of the limit tensile stress value $\sigma_{lim} = 0.5 \cdot \sigma_{fcm}$ in the most loaded solid concrete cross-section. Hence, the vertical force derives from Navier's formula replacing the stress with its maximum (allowable) value:

$$\sigma = \frac{M}{W} = \sigma_{lim} \quad \text{with } M = \frac{FL}{4} \text{ and } W = \frac{bh^2}{6}$$

$$F = \frac{2 \sigma_{lim} \cdot b h^2}{3 L}$$

Equation 4-3

Depending on the material flexural strength, a different value of the vertical force was defined as input data in the TO algorithm. According to the technical data sheet of the printable mortars adopted, the corresponding flexural strength is 8 MPa and 10 MPa for i.tech N and i.tech NF. Equation 6-3 provides the design vertical load of 26kN and 33 kN for such values.

The algorithm provided two different optimised beam solutions for two investigated printable materials as a set of second-order Bezier curves in compliance with the path-continuity constraint. Note that the layer width was assumed equal to 4 cm. The parametric equation of the i-th curve can be derived from Equation 4-2 for n=2:

$$\beta^i(s) = (1 - s)^2 \cdot P_0^i + 2s \cdot (1 - s) \cdot P_1^i + s^2 \cdot P_2^i \quad \text{with } s \in [0,1]$$

Equation 4-4

Once obtained the optimised shape of each beam, connecting points of the curve were slightly modified to avoid excessive concrete material accumulation during printing (P_2^1 and P_2^3 were shifted 3 cm up). Figure 4-5 represents the solutions and the final printing path adopted for the production phase. Note that the control points of the curve β^3 were imposed collinear in the algorithm. As expected, the optimisation tool gives a shape reproducing the stress flow within the element, i.e. the isostatic curve in compression and tensile stress state. The solution is a kind of “Fink truss”, a basic webbed truss design that provides the most economical roof solution. The optimisation tool saved about 61.5 and 64% of the concrete material for i.tech N and i.tech NF, respectively.

(a)

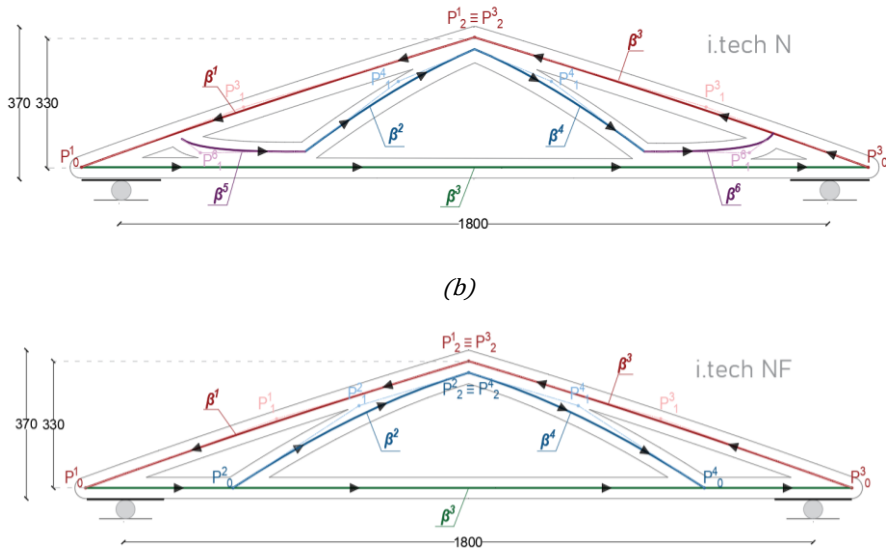


Figure 4-5: Bezier curves solution and printing path definition for (a) i.tech N and (b) i.tech NF.

The vertical force induces in the midspan of the reference beam a bending moment of 11.7 and 14.8 kNm, resulting in maximum tensile stress equal to the limit value imposed (i.e. 4MPa and 5MPa). The same force induces maximum tensile stress (σ_1 in Figure 4-6) approximately equal to 3.7 MPa and 5.1 MPa for i.tech N and i.tech NF, respectively.

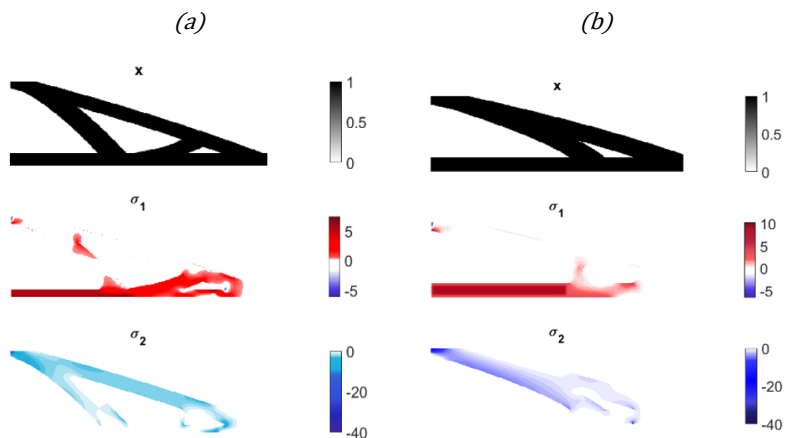


Figure 4-6: Principal stress in the optimised solution (a) i.tech N and (b) i.tech NF.

The Bezier curves were successively transformed in *RAPID codes* (in the ABB environment) for the printing session, according to the continuous paths shown in Figure 4-5. The elements were realised by stacking 20 layers of 10 mm height. Figure 4-7 shows a picture of the i.tech NF beams printing.



Figure 4-7: Printing session for the production of the specimen NF_01 and NF_02.

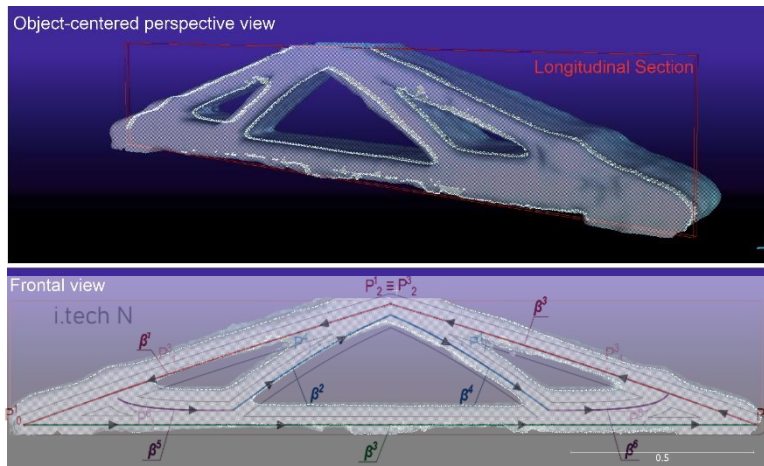


Figure 4-8: Point cloud acquisition and comparison with the Bezier parametric curves (specimen N_01).

Two specimens for each cementitious material were printed: N_01, N_02, NF_01 and NF_02. The front side of the beam was scanned using a mobile structure sensor, developed by Occipital Inc, to compare the printed geometry with the 3D designed model. Figure 4-8 shows the compliance between the

designed shape and the point cloud for the specimen N_01. However, a variable layer width was observed during the printing due to a slight variation in material consistency (Figure 4-9).

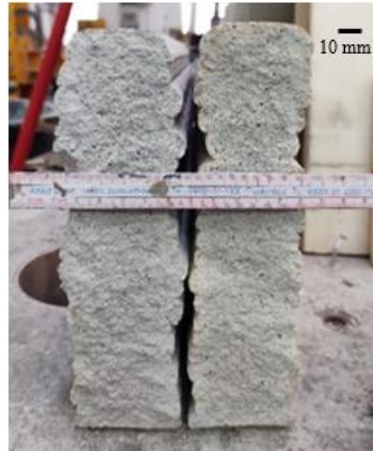


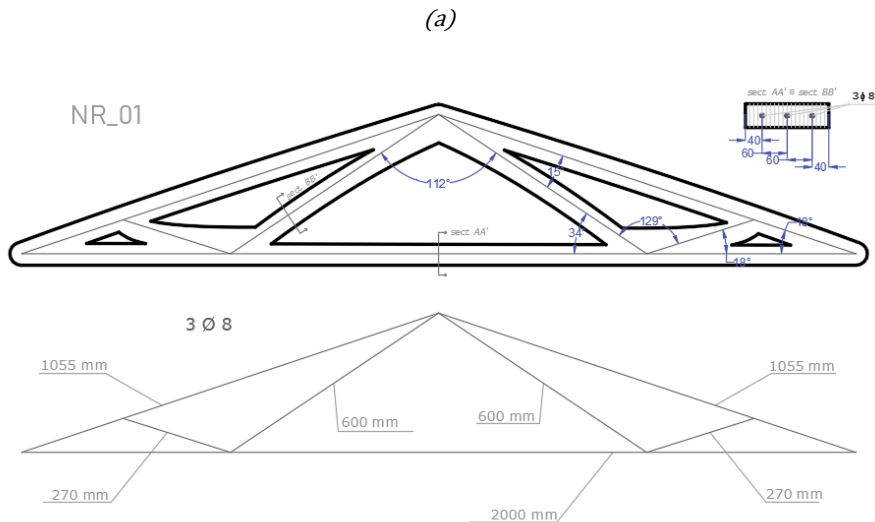
Figure 4-9: Example of the geometrical imperfection in the 3D printed elements.

This issue could be overcome by using a more uniform packaging solution, such as the “big bag”, and printing nozzles with increased shape control [110]. Through the laser scanning acquisition, it was possible to estimate the average width for each beam, resulting in 42, 45, 50 and 48 mm for N_01, N02, NF_01 and NF_02.

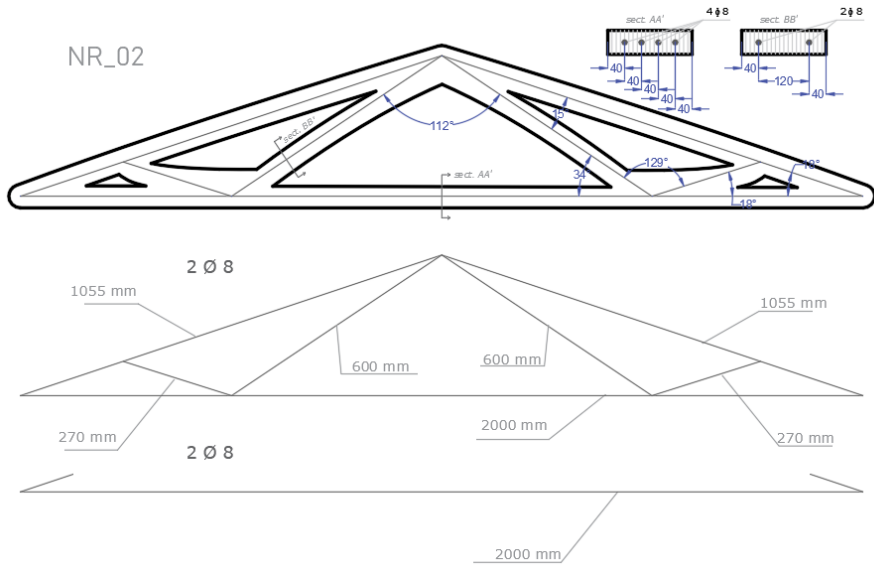
4.1.3 Steel reinforced topology optimised beams fabrication

Steel reinforced printed beams were additionally fabricated employing the same optimised shapes. The reinforcement strategy consisted of small diameter bars (i.e. 8mm) placed between consecutive layers during the printing. More in detail, two geometrical percentages of steel reinforcement ρ (i.e. 1.9 and 2.5%, expressed as the ratio between steel area and concrete area in the cross-section of truss element 200x40 mm) was included in the element. The lower percentage (from now on referred to as R_01) consists of three reinforcement layers, i.e. three identical layers of small bars welded in the ends (Figure 4-10 (a) and (c)). The higher percentage of reinforcement (from now on referred to as R_02) consists of two of the above layers and two straight bars placed in the

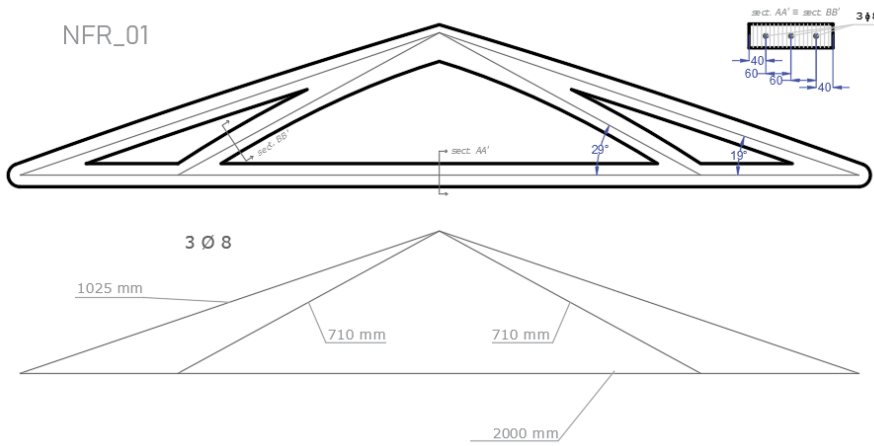
most loaded element (in the tensile state) of the beam, i.e. the bottom chord (Figure 4-10 (b) and (d)). The above reinforcement percentage values derive from geometrical constraints; indeed, the bars were included in the element during the printing between two consecutive layers, and their manual placement induces a slight disturbance. In order to ensure the correct effectiveness of the steel reinforcement, a minimum number of four cementitious filaments was guaranteed between two consecutive bars (as shown in Figure 4-10), resulting in $\rho = 2.5\%$. Note that $\rho = 2.5\%$ (in the solution R_02) refers to the reinforcement included in the bottom chord. The other beam elements were characterised by $\rho = 1.3\%$ (i.e. two bars placed in the cross section) having an optimised use of the steel amount. Furthermore, a lower percentage (i.e. $\rho = 1.9\%$) was also employed to assess the effect of steel reinforcement amount on the global resistant mechanism. The reinforcement properties were obtained by direct tension tests on three samples; the average yield stress ($f_{s,y}$) was 500 MPa. Even in this case, through the laser scanning acquisition, it was possible to estimate the average width for each beam, resulting in 68, 60, 55 and 62 mm for NR_01, NR_02, NFR_01 and NFR_02 , respectively.



(b)



(c)



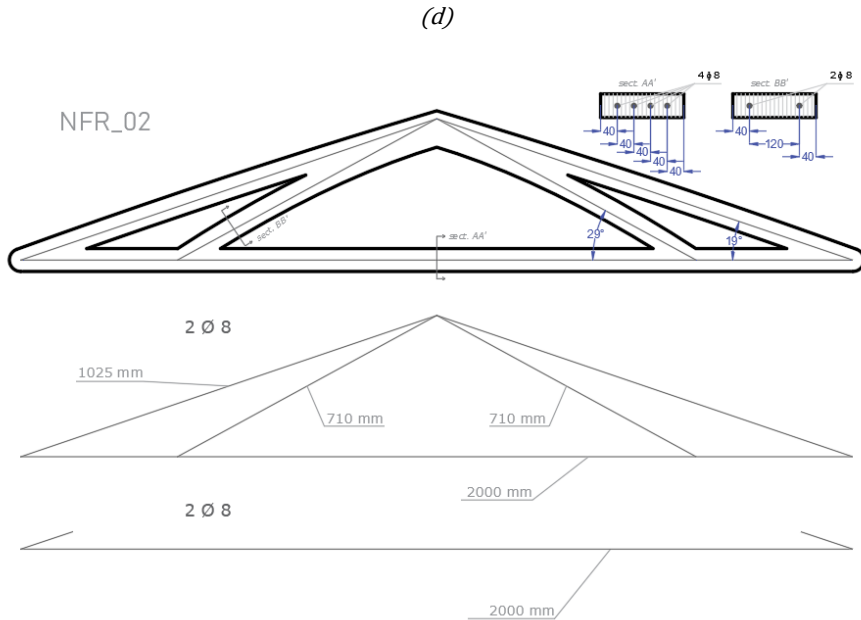
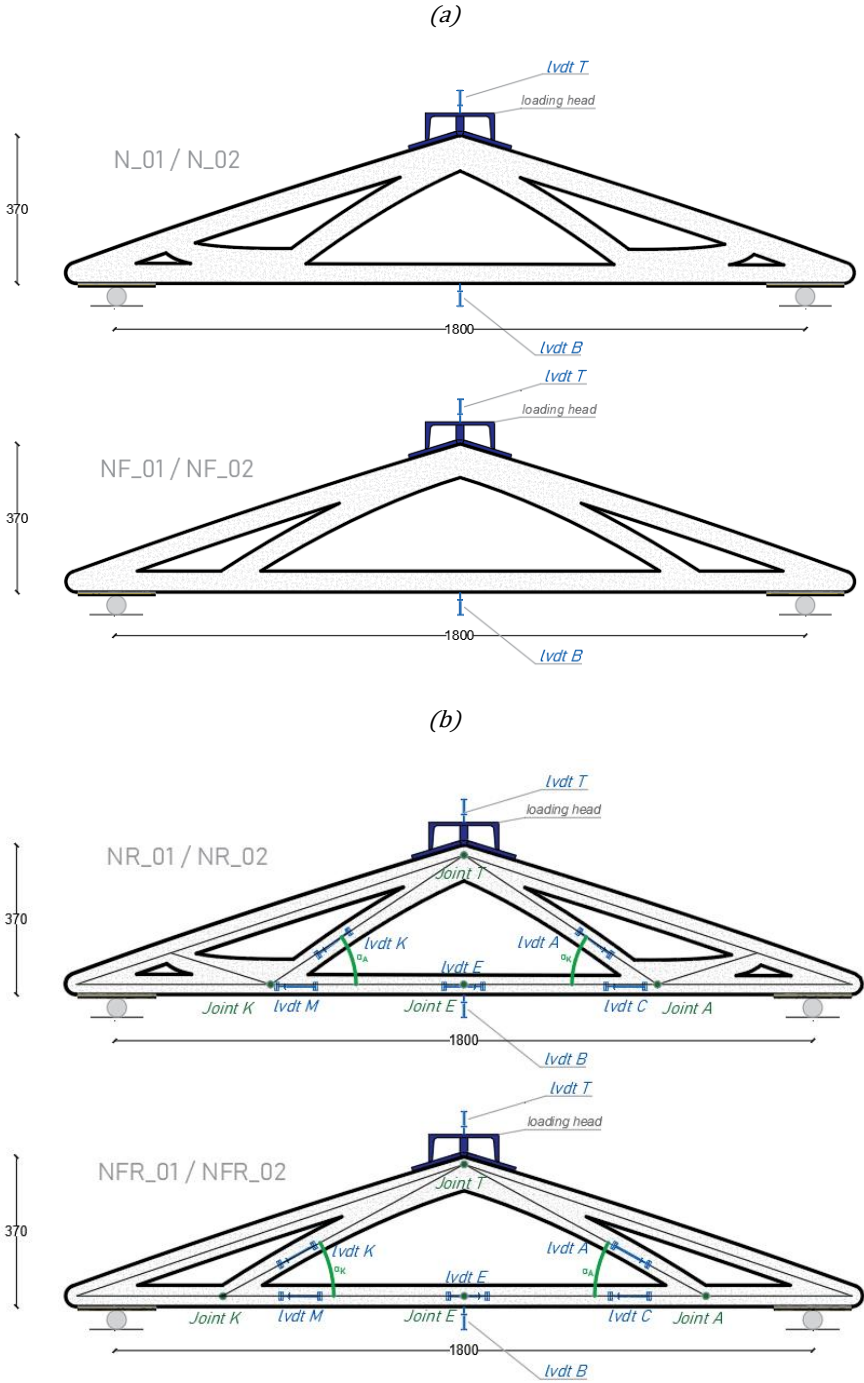


Figure 4-10: Steel reinforcement detailing (a) NR_01, (b) NR_02, (c) NFR_01 and (d) NFR_02.

4.1.4 Testing method

The mechanical performances of the optimised concrete beams were evaluated through the three-point bending test. The static scheme of the experimental test reproduces the adopted boundary conditions in the algorithm. Figure 4-11 (a) and (b) represent the testing set-up for unreinforced and reinforced beams, whereas Figure 4-11 (c) shows the details of the support zone. In particular, a layer of cementitious mortar was prepared in the support zone to smooth the 3D printed surface and ensure a uniform stress distribution together with the bearing steel plate and the layer of neoprene. The beams were tested in the displacement control condition (i.e. 0.005 mm/s) using an Italsigma universal machine equipped with a 100 kN load cell. Two LVDT sensors referred to as “T” and “B” in Figure 4-11 measured the vertical displacement in the mid-span of the beam. Additionally, the reinforced beams were equipped with other LVDT sensors called “M, E, C, K, A”, allowing the strain measurement of the diagonal elements and the bottom chord.



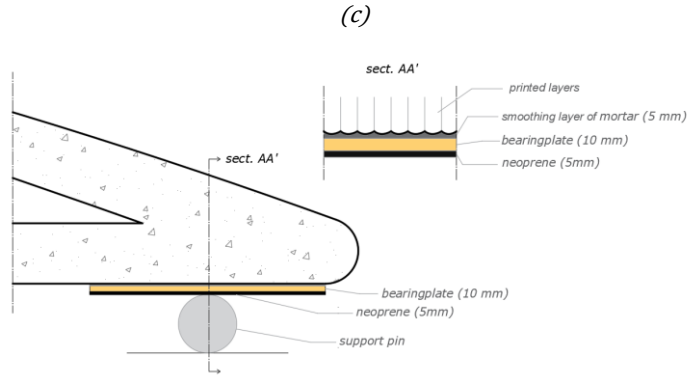


Figure 4-11: Testing set-up and instrumentation: (a) not reinforced and (b) reinforced beam with (c) the support details.

Note that a specific loading head reproducing the top beam profile was designed to avoid local stress concentration during the test; it was in contact with an additional mortar layer to have a smooth surface to load.

4.1.5 Experimental results and discussion

This section will discuss the experimental results obtained for both unreinforced and reinforced beams. Figure 4-12 shows the outcomes for each tested specimen regarding the force vs deflection diagram. The black cross in the figures indicates the loss of bearing capacity and the structural element failures.

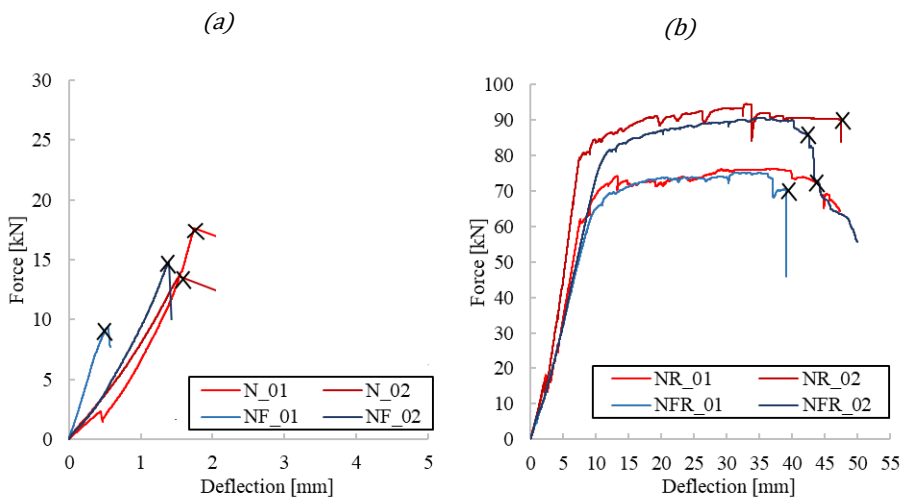
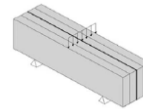


Figure 4-12: Force vs Deflection curves.

As expected, not reinforced beams showed a brittle failure when the tensile strength of cementitious mortar was reached in the most loaded element (i.e. bottom chord). The maximum vertical force values were 17.9, 13.8, 9.5 and 14.9 kN (Figure 4-12 (a)) for N_01, N_02, NF_01 and NF_02, respectively. The load value resulting from the flexural test was lower than the design force F derived from Equation 6-3. This discrepancy was attributed to the printed material's lower mechanical strengths than the cast counterpart, as experienced in other experimental work in literature [50]. Indeed, as a further verification, 4x4x16 cm specimens were cut from a straight wall (printed just after the beam production) and tested through a 3-points bending configuration at 28 days (orientation II), according to UNI EN 196-1: 2016. The average compressive and flexural strength, R_{cm} and σ_{cfm} , are reported in Table 4-1. The cylindrical compressive strength f_{cm} and the tensile strength f_{ctm} were obtained according to codes [NTC2018].

Table 4-1: Results of 3-points bending test performed on printed specimens

<i>according to UNI EN 196-1: 2016</i>				
Material	R_{cm} [MPa]	f_{cm} [MPa]	σ_{cfm} [MPa]	f_{ctm} [MPa]
i.tech N	44.2	36.6	4.5	3.8
i.tech NF	45.6	37.8	6.0	5.0



The flexural strength was 4.5 MPa and 6.0 MPa, lower than 8 MPa and 10 MPa used in the design phase (for i.tech N and i.tech NF, respectively). This finding highlights the need for adequate mechanical characterisation of the printed material since the different mixing procedure and the material preparation affects the mechanical response. The design force becomes 15 and 20 kN (instead of 26 and 33kN) if the values of Table 4-1 are assumed in Equation 4-3. There is a good agreement with the i.tech N beams (15kN vs the experimental 17.9 and 13.8 kN), whereas there is a load overestimation for i.tech NF (20kN vs the experimental 9.5 and 14.9 kN). Such behaviour is probably due to the lower filling degree of the i.tech NF beam, which causes a more significant geometrical imperfection influence on the global mechanical

response. It is worth noting that for the not reinforced beam, the failure load is low, and there is a not negligible influence of the slight geometry variation (Figure 4-9), and experimental scatter in mechanical strength. For i.tech NF beams, this aspect is more relevant because the diagonal webs are missing, resulting in a less robust and stiff configuration. Indeed, one of two tested i.tech NF specimens prematurely collapsed at 9 kN (i.e. NF_01) with a different position of the failure crack (as visible in Figure 4-16 (b)).

(a)



(b)

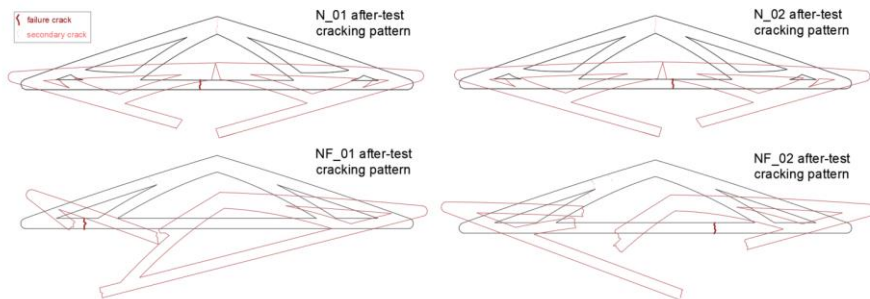


Figure 4-13: Not reinforced beam failure mechanisms: (a) picture before and after failure (specimen N_02) and (b) schematic representation of the failure mechanism.

Concerning the reinforced beams, Figure 4-14 portray the corresponding picture during the test execution.

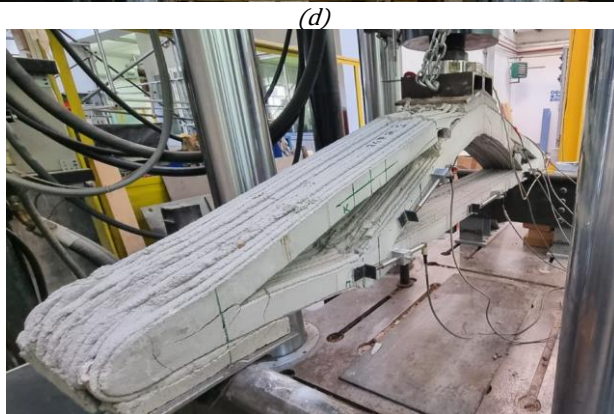
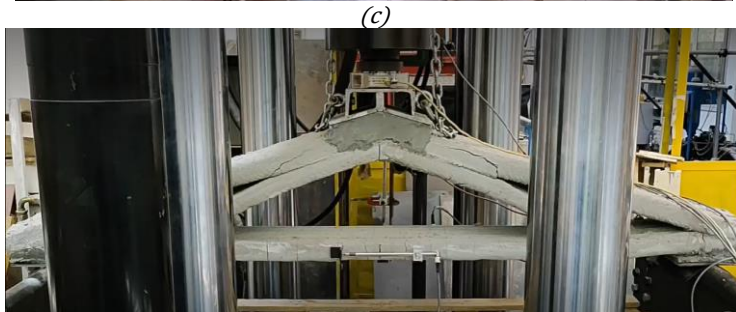
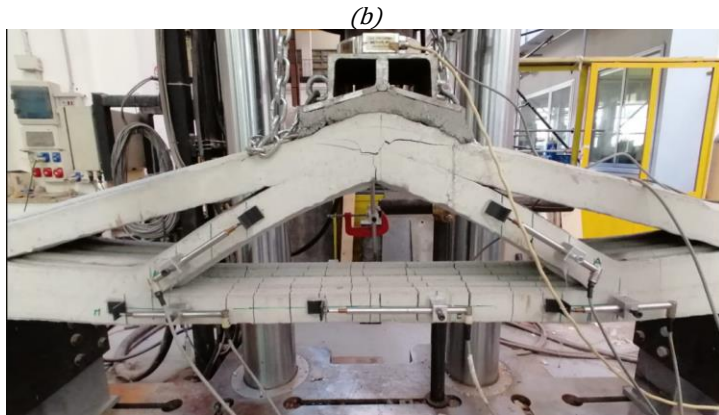
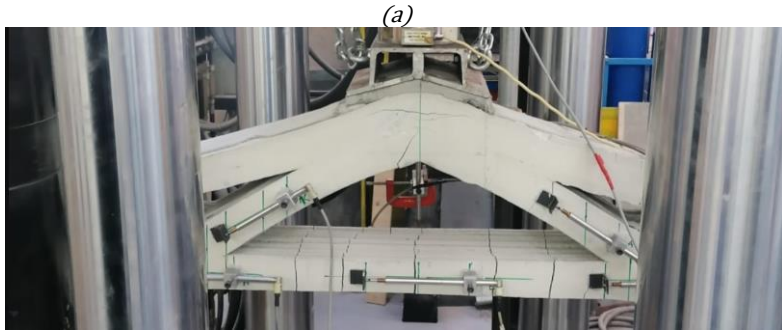


Figure 4-14: Pictures of the beams during the test execution: (a) NR_01, (b) NR_02, (c) NFR_01 and (d) NFR_02.

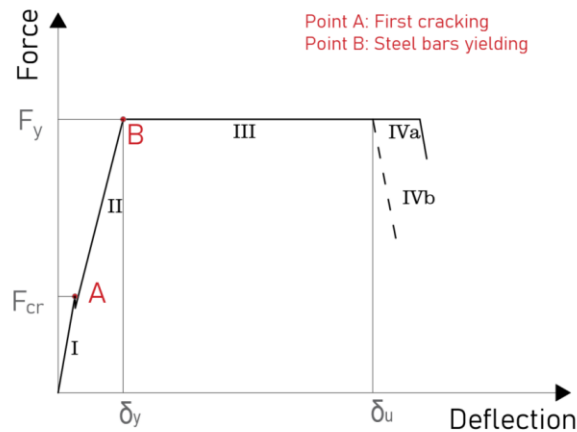


Figure 4-15: Typical mechanical response of 3DCP reinforced optimised beam

Figure 4-15 schematically represents the observed mechanical behaviour of the steel reinforced optimised beams (Figure 4-10). The first linear branch refers to the uncracked response: after a slight drop in the vertical force (point “A”), the reinforcement allowed redistribution of stresses, and the load continued to linearly grow until the steel yielding (point “B”). The corresponding force value F_y defines the deviation from linear behaviour, and its value grows with the percentage of reinforcement. Then the structural element showed a ductile response (thanks to the yielding of bars in the bottom chord) since it continued to deform at the same loading level (III branch in Figure 4-15). Finally, the beams continued to exhibit plastic deformation of steel and fail due to the crushing in compression of the top joint (Iva, beams NR_01 and NR_02) or collapse due to local instability (IVb, beams NFR_01 and NFR_02).

The slope of the force vs deflection curve indicates beam stiffness during the evolution of the test: before and after the cracking load (Point “A”), such stiffness did not significantly change. This aspect means that the stiffness is mainly correlated to the truss frame and it is not influenced by the bottom chord cracking, even considering that the cross section of each beam element is small compared to a solid beam.

For the four tested reinforced beams, the recorded yielding load was 62, 79, 60 and 76 kN for NR_01, NR_02, NFR_01 and NFR_02, respectively; after yielding, the maximum load achieved (due to kinematic hardening) was 76, 94, 74 and 91 for NR_01, NR_02, NFR_01 and NFR_02, respectively. It is worth noting that the difference between i.tech N and i.tech NF was negligible in terms of yielding load. Indeed, the two different optimised beams exhibited the same bearing capacity if the steel reinforcement is the same. The increment of reinforcement percentage (from 1.9% to 2.5%) provides a similar increment in the bearing capacity for both i.tech N and NF beams. Indeed, there is an increment of about 27%, passing from solution with 1.5 to 2.0% reinforcement percentage in both cases.

The yielding deflection δ_y was 8.26, 8.51, 8.53 and 11mm for NR_01, NR_02, NFR_01 and NFR_02, respectively.

Figure 4-16 shows pictures of the beams after the test. The i.tech N reinforced beams (Figure 4-16(a) and (b)) showed a uniform cracking distribution in the bottom chord and the crushing in compression of the top joint (see the red dashed circle in Figure 4-16(a) and (b)). Such a response complies with the force-deflection curve in which the element bearing capacity gradually decreases up to the ultimate failure. On the contrary, i.tech NF reinforced beams (Figure 4-16(c) and (d)) completely lose the bearing capacity (case IVb of Figure 4-15) before the attainment of the upper concrete crushing, showing a local rebar buckling mechanism in the lateral chord of the beam (see the red dashed circle in Figure 4-16(c) and (d)). In such a case, this premature collapse was probably due to the higher free length of the top chord elements. This collapse is visible in the global mechanical response of Figure 4-12 (b) where it is also possible to observe a sudden drop in the vertical force for both i.tech NF beams. As a result, the i.tech N beams showed a more ductile response, which can be quantified as the ratio between the deflection at failure load to that at yielding (i.e. ductility index). The ductility index is about 3.2 and 4.3 for

NFR_01 and NFR_02, respectively. The ductility index is higher for i.tech N, resulting in 5.2 and 5.6 for NR_01 and NR_02.

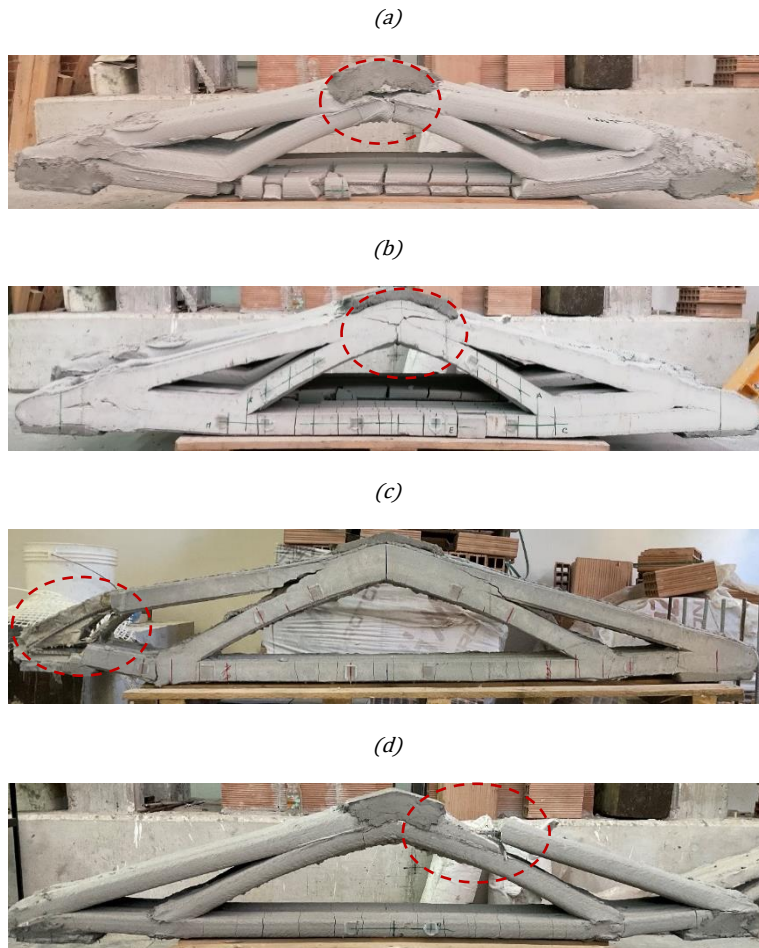


Figure 4-16: Beams after test: (a) NR_01, (b) NR_02, (c) NFR_01 and (d) NFR_02.

The mechanical response is also correlated to the joint stiffness characterization. Indeed, the joints can be schematized as fixed or hinge, depending on the possibility to transfer the bending moment. As a result, the joint behaviour definition is significant for the design purpose. For such reason, the rotations at joints A and K of Figure 4-11(b) were assessed using the generalised Pitagora theorem. This theorem provides the angle value of a triangle with known edges: in the specific case, the edges are the lines joining

“A”, “E” and “T” (or equivalently “K”, “E” and “T”) of Figure 4-11(b). Figure 4-17 portrays the percentage variation of the above angle (namely α) with the beam deflection (i.e. $\Delta\alpha$).

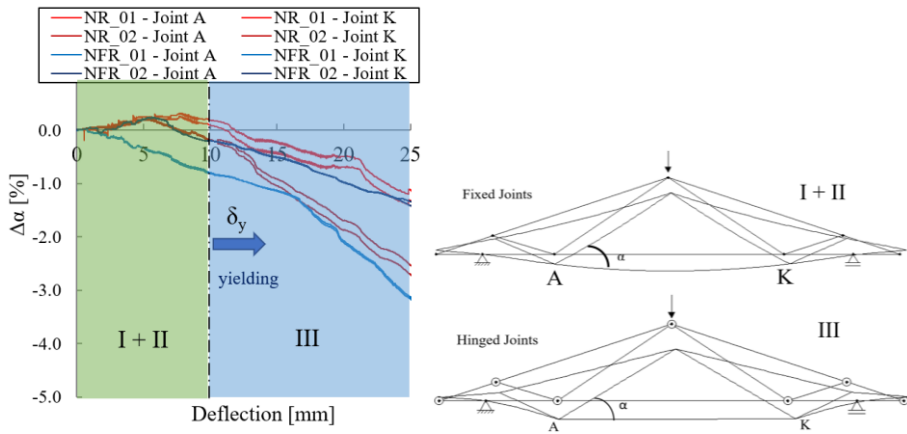


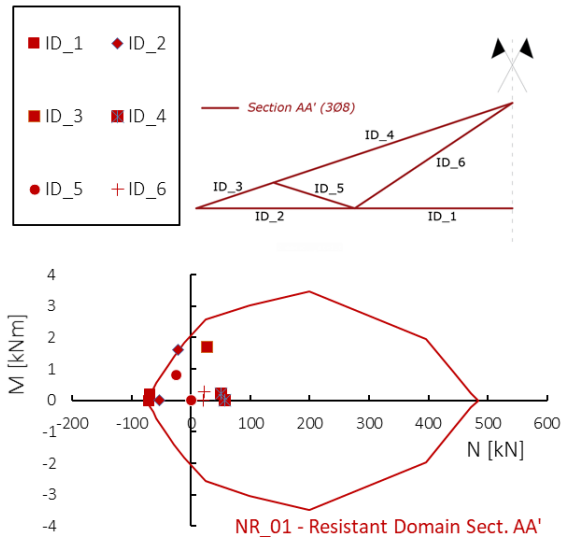
Figure 4-17: Percentage angle variation at Joint A and K.

It is possible to observe that the $\Delta\alpha$ assumes low values up to 10 mm (which approximately corresponds to the yielding visible in Figure 4-12(b)), after which the rotation starts to grow in absolute value. Therefore, the rotational stiffness of the joint tends to decrease with the steel yielding. The percentage variation reaches a maximum absolute value of about 1.3% for NR_01 and NFR_02, 2.6% for NR_02 and 3.1% for NFR_01. Such difference is probably due to the layer width: the beam with the highest layer width values showed a stiffer response.

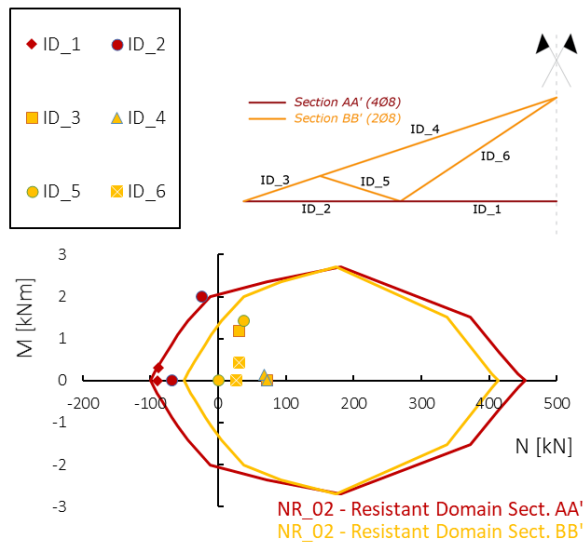
Figure 4-18 portrays the resistant M-N domain (built according to the material properties of Table 4-1 and assessed for the section AA' and BB' of Figure 4-10) with the points representing the stress state (i.e. normal force and bending moment) of the most critical section when on the beam is subject to a vertical load equal to the yielding force F_y (i.e. 62, 79, 60 and 76 kN for NR_01, NR_02, NFR_01 and NFR_02, respectively). Note that the stress state was computed in the assumption of both (i) fixed and (ii) hinged joint configuration. In Figure

4-18, the points lying on the horizontal axis are related to the configuration (ii), since, in this configuration, each element is only subject to the normal force.

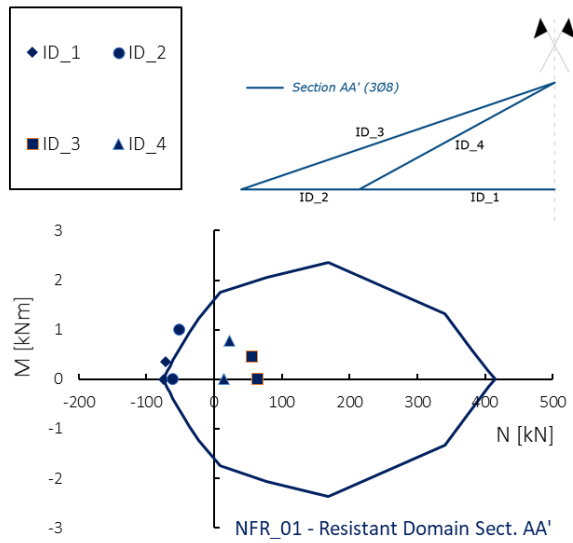
(a)



(b)



(c)



(d)

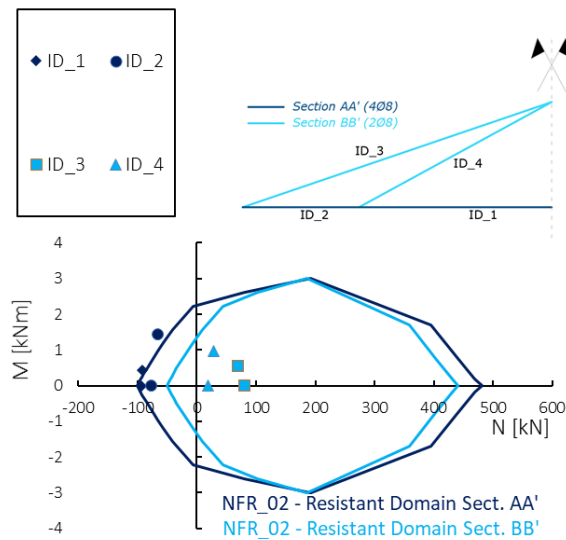


Figure 4-18: M-N resistant domain for (a) NR_01, (b) NR_02, (c) NFR_01 and (d) NFR_02.

In each case, the point on the resistant domain is related to the bottom chord (i.e. ID_1 and ID_2 reach the collapse), resulting in the most critical element for the examined beams. Indeed, the stress state of the compressed elements (i.e. ID_3, ID_4 and ID_5) are far from the resistant domain.

Furthermore, there is a different value of mean crack distance (in accordance with the structural behaviour of traditional RC elements) depending on the amount of reinforcement. As expected, increasing the reinforcement percentage, the mean distance between two consecutive cracks decreases as well as the crack opening.

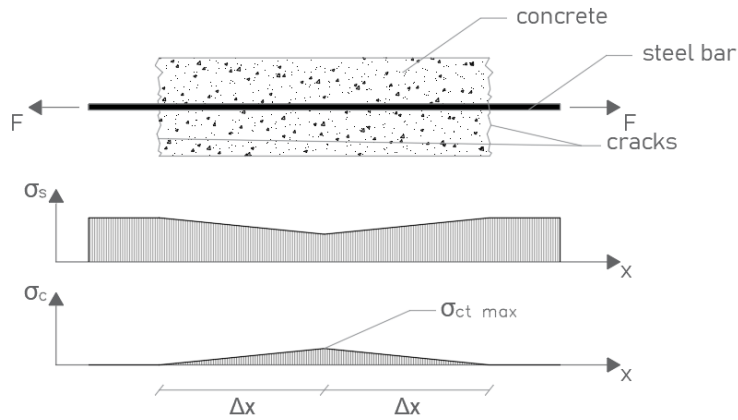


Figure 4-19: Stress state in concrete and steel bar between two consecutive cracks

The average cracking space s_c^{exp} was measured for each beam (Figure 4-16), resulting in 130, 80, 74 and 72 mm, for NR_01, NR_02, NFR_01 and NFR_02, respectively. These values result proportional to the effective reinforcement percentage (i.e. ratio between the reinforcement area and the effective cross-section area) of 1.1, 1.7% for NR_01 and NR_02, and 1.4, 1.6% for NFR_01 and NFR_02.

Considering the bond stress transfer mechanism (schematically represented in Figure 4-19), the concrete surrounding the bar cracks when the stress is equal to the tensile strength:

$$\sigma_{ct} \cdot A_{ct} = \tau_b \cdot \pi \phi \cdot \Delta x \cdot n_b$$

Equation 4-5

Where A_{ct} is the concrete area in the tensile state, τ_b is the bond stress at the bar-concrete interface, ϕ is the bar diameter, n_b is the number of bars in the

cross-section and Δx is the length in which the bar transfers stress equal to tensile strength to the mortar (see Figure 4-19). Hence, the cracking space can be assessed as:

$$s_c = 2 \cdot \Delta x = 2 \cdot \frac{\sigma_{ct} \cdot A_{ct}}{n_b \cdot \tau_b \cdot \pi \phi}$$

Equation 4-6

Assuming A_{ct} equal to the cross-section area (during the test, the whole section area cracked) and τ_b equal to bond strength measured in the pull-out test campaign with i.tech NF (for the parallel configuration), Equation 4-6 provides 95 and 80 mm as cracking space in the bottom chord of NFR_01 and NFR_02, against the experimental 74 and 72 mm. It is worth noting that Equation 4-6 derives from theoretical forces equilibrium without considering empirical reduction factors as required by codes [NTC 2018]. Indeed, if the mean cracking distance is assessed according to the technical code, the resulting values grow to 250, 180, 225 and 184 mm.

With the aim to quantify the advantage in the amount of construction used materials exploiting the topology optimisation in the 3DCP field, a traditional cast (TC) beam was designed (according to NTC2018) to have a bearing capacity of 60 and 80 kN, i.e. similar values to those experimentally obtained. For a more reliable comparison, the TC simply-supported beams were designed assuming unitary partial safety coefficients (i.e. the average values of mechanical properties were considered). Furthermore, two solutions were supposed to increase the flexural capacity from 60 to 80 kN: increment in cross-section area, i.e. beam height, or increment in the percentage of steel reinforcement.

Figure 4-20 represents the amount of concrete and steel reinforcement for both fabrication methods (filled circles for 3DCP and black squares for cast beam). It is possible to observe that 3DCP optimised investigated beams have similar structural performances to the cast ones, saving up to 25% and 26% in concrete and steel reinforcement weight, respectively. Such result implies the

environmental benefits of 3DCP technology over conventional methods, as already assessed in more accurate analyses available in the literature [111].

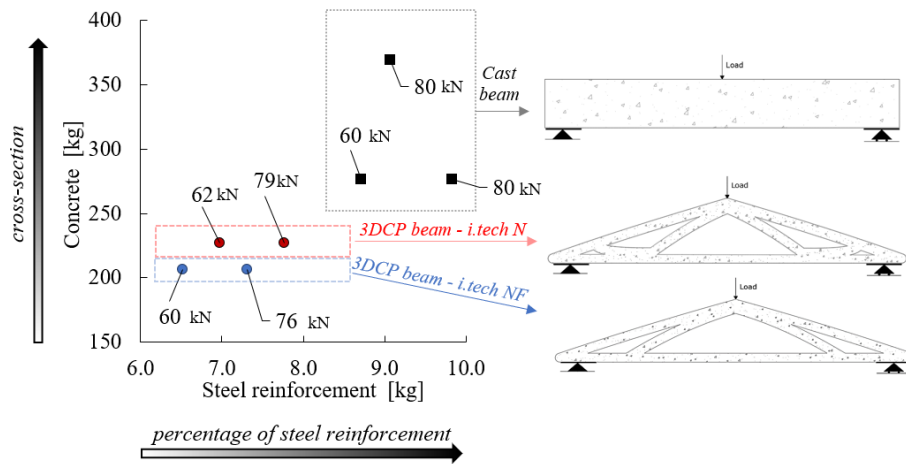


Figure 4-20: Comparison in bearing capacity between experimentally 3DCP beams (*i.tech N* and *i.tech NF*) and traditional cast beams (designed according to [NTC2018]).

4.1.6 Conclusion

Topology optimised beams were designed and produced with 3DCP technology. The optimisation algorithm provided a feasibility solution in compliance with the mechanical and technological constraints, allowing to obtain the beam shape as a set of parametric curves (i.e. Bezier curves). Two different solutions were obtained for two cementitious materials employed, allowed saving saved about 61.5 and 64% of mortar. A total number of four beams (two specimens for each set) were printed and tested in order to verify the solution's feasibility and investigate the bearing capacity.

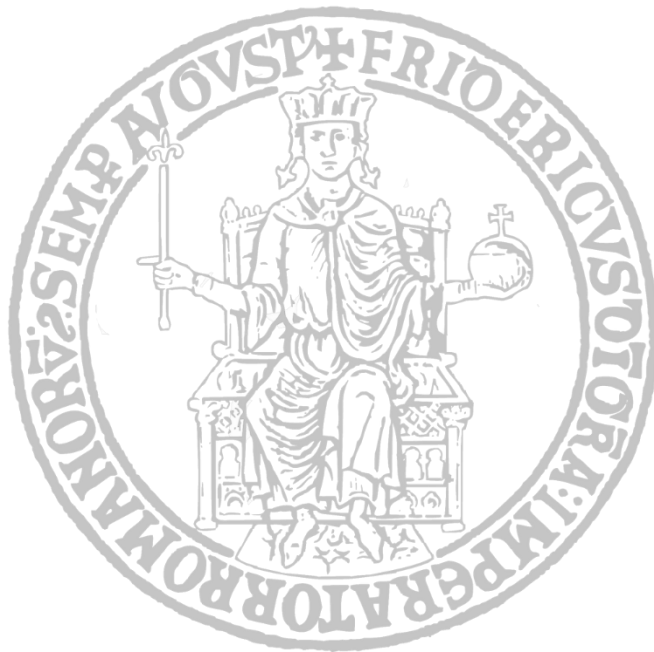
The experimental cracking load was lower than the values assumed in the optimisation; such difference was due to (i) the lower mechanical properties of printed specimens than the design values and (ii) the geometry variability of the cross-section. The first issue could be overcome by defining a reliable testing method for the characterisation at the hardened state of printed elements, including the effect of the layer orientation on the mechanical performances. The second one could be fixed by using a printing nozzle with higher shape

control and avoiding changes in material consistency during the entire printing session.

Additionally, steel-reinforced beams were fabricated employing the same optimised shapes. The reinforcement strategy consisted of small diameter bars placed between consecutive layers during the printing process. The aim was to study the effectiveness of this reinforcement strategy and the mechanical response under monotonic load (e.g. global stiffness, local failures, cracking pattern, joints characterisation). More in detail, two geometrical percentages of steel reinforcement were included in the structural elements to assess the effect on the global resistant mechanism.

Experimental tests performed on the reinforced beams demonstrated good mechanical performance of these structural elements with high bearing capacity and ductile behaviour. The bars in the bottom chord yielded in both reinforcement solutions so that the bearing capacity strongly depended on the reinforcement percentage.

Due to local failure mechanisms, beams collapsed after a constant bearing capacity branch: crushing in compression of the loaded area (for i.tech N) or diagonal element buckling (for i.tech NF). Furthermore, the LVDT recording permitted the joint rotation evaluation. Indeed, the mechanical response is also correlated to the joint stiffness characterization since it can be schematized as fixed or hinge, depending on the possibility to transfer the bending moment. In the specific case, the behaviour can be assumed as hinged after yielding.



5. Conclusion

The main objective of the thesis work was to introduce a comprehensive experimental-numerical approach for the digital fabrication of reinforced concrete elements. The research activities were divided into three parts focused on different but strictly correlated topics:

- (i) experimental testing and analytical modelling of fresh 3D printable mortars;
- (ii) study of the reinforcement strategies' effectiveness in 3D printed elements and investigation of the printing system/material influence;
- (iii) design and testing of digitally fabricated optimised beams, with and without steel reinforcement.

In *Part I*, the experimental characterization was focused on the early-age compressive response of two types of printable mortar: UniNa and Italcementi (i.tech N and NF) mortar.

The main critical aspects of the characterization of fresh mortars, i.e., specimen preparation and testing parameters, were highlighted through the experimental campaigns of UUCT. The specimen preparation appeared to be difficult since the material was fresh. Indeed, with the aim to characterize the material under conditions as close as possible to those of the newly extruded material from the print head, the preparation should avoid any disturbance and must be quick. Furthermore, the fresh material hardens during the testing execution due to cement hydration. Therefore, the main parameter of the UUCT, i.e. the displacement rate, must be adequately chosen. The displacement rate should be high enough to avoid the material curing during the test execution but sufficiently low to avoid viscous effects (such as the rate sensitivity of the compressive strength). The stress-strain laws derived from UUCT performed at a different resting time allowed the compressive strength and stiffness

evaluation. These properties and their evolution with the curing are necessary to predict the mechanical response of printed objects during the production process (e.g. vertical deformation and buildability requirement assessment). Experimental results provided the values of strength and stiffness for different printable mortar. In detail, it was observed that the elastic modulus at time $t=0$ min (time of extrusion) ranged from 170 and 210 kPa and from 170 to 490 kPa for the UniNa and Italcementi mortar (depending on the displacement rate value adopted during the test), respectively. The compressive strength varied from 8 to 11 kPa and from 23 to 45 kPa, for UniNa and Italcementi material.

Early age creep tests were additionally performed to study the visco-elastic response of printable cementitious mortars. Indeed, the mechanical response of such materials to an external stimulus (i.e., imposed strain or load) could not be completely instantaneous, but part of it can be delayed. In detail, two types of tests were carried out to evaluate (a) the deformation under constant load (for UniNa mortar) and (b) deformation under printing-type loading history (for Italcementi i.tech N and NF mortar).

- (a) Even in this case, the testing procedure was carefully defined. The testing parameters were chosen through an iterative process to satisfy the instantaneous load application assumption and the full development of the early-age creep strain. Experimental results confirmed the viscous response of such material, since they revealed that the early-age creep strain represented a pronounced amount of the total vertical deformation, with a value of 1.1% and 0.2% at 0 and 60 minutes, respectively (vs 1.15% and 0.35% of elastic strain values). Experimental outcomes, i.e., total strain vs time curves at 0, 15, 30 and 60 minutes, were used to calibrate the visco-elastic Burgers model. To also consider the curing process of the material, the Burgers parameters were calibrated as time-dependent.
- (b) The testing method consisted of a step-wise loading history reproducing the stress state of the first layer during the printing. This

test is more flexible and allows replicating different building rates (or stress rates). The experimental outcomes were successively used to calibrate the analytical time-dependent Burgers model. Such model allowed satisfactorily simulate the experimental mechanical response in the range of the stress rate investigated. With such model it is possible to predict the self-buckling collapse during the printing. In this sense, the equivalent Burgers stiffness and the correlated buildability domains could be a helpful tool to predict the buildability of a new printable mortar helping the standardisation of such requirement.

In *Part II*, the result of an interlaboratory study with the foreign ETHZ university on incorporating steel reinforcement into 3DCP concrete elements was presented and discussed. Interlaboratory studies can be helpful in the standardization of the testing procedures, highlighting difficulties, challenges and possible solutions to define a simple and reliable experimental method.

An identical experimental campaign of pull-out tests was performed in two different laboratories (UniNa and ETHZ) to understand the feasibility of including steel reinforcement into printed layers and the influence of different printing setups and materials on the steel-concrete bond. In detail, two different 3D printable mortars were employed: the i.tech NF high yield stress mortar developed by Italcementi (UniNa NF mortar) and a set-on-demand cementitious formulation (ETHZ mortar).

Testing results showed that using steel bars in 3D printing applications could be a reliable reinforcement strategy. Indeed, the recorded bond strength (ranged from 29.7 to 30.6 MPa and from 15.4 to 19.3 MPa, for the ETHZ and UniNa printing system/material) was high, and its value had a limited fabrication method influence (i.e. printing vs cast). The ETHZ specimens generally provided higher bond strength than the UniNa NF ones, and this is mainly linked to the higher compressive strength and lower viscosity of the set-on-demand mortar employed at ETHZ. The correlation between the bond and

compressive strength is widely investigated in literature and in available codes. The correlation experienced at UniNa and ETHZ was also compared to the experimental data available in the literature for conventional concrete, resulting in better performances related to 3DCP pull-out testing results. This is probably associated with (i) the difference in the cementitious formulation of printable materials with respect to the conventional concrete (e.g. aggregate size, cement content) and (ii) the small bar diameter employment, rather than the fabrication method itself (cast vs 3D printed). Furthermore, the bond strength laws provided for conventional concrete by Model Code 2010 underestimate the bonding performance in reinforced printable mortars. Regarding this aspect, a new expression for the bond strength assessment was proposed, slightly modifying the existing one provided by the code.

This interlaboratory study showed the importance of collaborative research for 3D concrete printing. The structural behaviour of the produced elements depends not only on the chosen concrete quality but also on the applied production and testing strategy. This dependence requires further attention since it is important to understand these influences for designing possible standards and codes.

In *Part III*, the design and testing of topology optimised digitally fabricated concrete beams was described as a conclusive part of the research activities.

Topology optimised beams were produced with and without steel reinforcement to verify the solution's feasibility and investigate their load-bearing capacity, along with the definition of proper analytical models helpful in interpreting the structural behaviour. The optimised shapes of the fabricated element were derived from a TO algorithm which provided the solution as a set of Bezier curves. The approach considered both mechanical and technological constraints. Two different solutions were obtained for two cementitious materials employed (i.e. Italcementi i.tech N and i.tech NF), saving about 61.5 and 64% of mortar.

Four unreinforced beams were printed and tested in order to verify their printability. The elements were then tested adopting the same configuration (i.e. boundary conditions) used in the optimisation algorithm. The recorded cracking/failure loads (i.e. 17.9, 13.8, 9.5 and 14.9 kN) were lower than the expected values deriving from the optimisation algorithm due to (i) the lower mechanical properties of printed specimens than the design values and (ii) the geometry variability of the cross-section. As a result, the experimental outcomes highlighted the need to verify the hardened properties of the printed elements, for example producing straight walls to extract samples to test.

Furthermore, the geometrical imperfections (layer width variation along the cross-section) were controlled through laser scanning acquisitions to evaluate the average layer width value. These imperfections should be avoided during the printing, and in that sense, this issue could be overcome by using a more uniform packaging solution, such as the “big bag”, and printing nozzles with increased shape control.

Additionally, steel-reinforced beams were fabricated employing the same optimised shapes. The adopted reinforcement strategy was the same developed and assessed in Part II. Therefore, small diameter bars were placed between consecutive layers during the printing process, and two reinforcement percentages were employed. The aim was to study the effectiveness of this reinforcement strategy on the global mechanical response of digitally fabricated elements.

Experimental outcomes demonstrated good mechanical performance of these structural elements with high bearing capacity (depending on the reinforcement amount) and ductile behaviour. The recorded yielding load ranged between 62 to 79 kN and from 60 and 76 kN, for i.tech N and i.tech NF. There was a bearing capacity increment of 27% passing from 1.9% to 2.5% in terms of geometrical reinforcement percentage in both cases.

All beams collapsed after a constant bearing capacity branch due to local failure mechanisms (i.e. crushing in compression or diagonal element buckling).

The bearing capacity of this type of structural element was also assessed using M-N domain. Indeed, the resistant domain was evaluated for each element of truss beams and compared with the corresponding stress (evaluated for a vertical load equal to the yielding force experimentally recorded). Such elaborations confirmed that the most critical element was the bottom chord in all cases.

As a result, the M-N domain could be used for the design purpose of 3D printed truss beams, considering the stress state in both fixed and hinged configurations for conservative purposes.

Furthermore, a comparison of bearing capacity between the investigated 3DCP beams and the cast ones traditionally designed was performed, highlighting the environmental benefits of 3DCP technology over conventional methods. Maintaining the same bearing capacity, the 3D optimised beams allowed saving up to 25% and 26% in concrete and steel reinforcement weight, respectively, with respect to cast beams designed according to the code.

Including steel reinforcement in 3D printed structural elements is crucial in this emerging field since 3DCP technology employs cementitious materials known to be highly brittle. The adopted strategy allows high flexibility in the bar placing, with a procedure automatically implementable using a second robotic arm working in parallel.

The thesis addressed different but strictly correlated topics of the 3DCP technology concerning the design, production and testing of the structural elements; the presented experimental activities resulted in helpful data toward the standardisation of the testing procedures for the material characterisation and design-to-fabrication approaches in the 3DCP field.

Bibliography

1. Menna C, Mata-Falcón J, Bos FP, et al (2020) Opportunities and challenges for structural engineering of digitally fabricated concrete. *Cement and Concrete Research* 133:106079. <https://doi.org/10.1016/j.cemconres.2020.106079>
2. De Schutter G, Lesage K, Mechtcherine V, et al (2018) Vision of 3D printing with concrete — Technical, economic and environmental potentials. *Cement and Concrete Research* 112:25–36. <https://doi.org/10.1016/j.cemconres.2018.06.001>
3. Complex concrete structures: Merging existing casting techniques with digital fabrication - ScienceDirect. <https://www.sciencedirect.com/science/article/pii/S001044851400044X?via%3Dihub>. Accessed 9 Jan 2022
4. The Instant House: A Model of Design Production with Digital Fabrication - Lawrence Sass, Marcel Botha, 2006. <https://journals.sagepub.com/doi/10.1260/147807706779399015>. Accessed 9 Jan 2022
5. Wangler T, Roussel N, Bos FP, et al (2019) Digital Concrete: A Review. *Cement and Concrete Research* 123:105780. <https://doi.org/10.1016/j.cemconres.2019.105780>
6. Gibson I, Rosen DW, Stucker B (2010) *Additive Manufacturing Technologies*. Springer US, Boston, MA
7. Agustí-Juan I (2018) *Sustainability Assessment and Development of Guidelines for Digital Fabrication in Construction*. Doctoral Thesis, ETH Zurich
8. Ortiz O, Castells F, Sonnemann G (2009) Sustainability in the construction industry: A review of recent developments based on LCA. *Construction and Building Materials* 23:28–39. <https://doi.org/10.1016/j.conbuildmat.2007.11.012>
9. Buswell RA, da Silva WRL, Bos FP, et al (2020) A process classification framework for defining and describing Digital Fabrication with Concrete. *Cement and Concrete Research* 134:106068. <https://doi.org/10.1016/j.cemconres.2020.106068>

10. Tay YWD, Panda B, Paul SC, et al (2017) 3D printing trends in building and construction industry: a review. *Virtual and Physical Prototyping* 12:261–276. <https://doi.org/10.1080/17452759.2017.1326724>
11. Khoshnevis B (2004) Automated construction by contour crafting—related robotics and information technologies. *Automation in Construction* 13:5–19. <https://doi.org/10.1016/j.autcon.2003.08.012>
12. Mechtcherine V, Nerella VN, Will F, et al (2019) Large-scale digital concrete construction – CONPrint3D concept for on-site, monolithic 3D-printing. *Automation in Construction* 107:102933. <https://doi.org/10.1016/j.autcon.2019.102933>
13. Large-scale 3D printing of ultra-high performance concrete – a new processing route for architects and builders - ScienceDirect. <https://www.sciencedirect.com/science/article/abs/pii/S0264127516303811>. Accessed 18 Jan 2022
14. Buswell R, de Silva WRL, Jones SZ, Dirrenberger J (2018) 3D printing using concrete extrusion: a roadmap for research. <https://doi.org/10.1016/j.cemconres.2018.05.006>]
15. Gaudillière N, Duballet R, Bouyssou C, et al (2019) Chapter 3 - Building Applications Using Lost Formworks Obtained Through Large-Scale Additive Manufacturing of Ultra-High-Performance Concrete. In: Sanjayan JG, Nazari A, Nematollahi B (eds) *3D Concrete Printing Technology*. Butterworth-Heinemann, pp 37–58
16. Popescu M, Reiter L, Liew A, et al (2018) Building in Concrete with an Ultra-lightweight Knitted Stay-in-place Formwork: Prototype of a Concrete Shell Bridge. *Structures* 14:322–332. <https://doi.org/10.1016/j.istruc.2018.03.001>
17. Lowke D, Dini E, Perrot A, et al (2018) Particle-bed 3D printing in concrete construction – Possibilities and challenges. *Cement and Concrete Research* 112:50–65. <https://doi.org/10.1016/j.cemconres.2018.05.018>
18. Paul SC, van Zijl GPAG, Tan MJ, Gibson I (2018) A review of 3D concrete printing systems and materials properties: current status and future research prospects. *Rapid Prototyping Journal* 24:784–798. <https://doi.org/10.1108/RPJ-09-2016-0154>

19. Khan MS, Sanchez F, Zhou H (2020) 3-D printing of concrete: Beyond horizons. *Cement and Concrete Research* 133:106070. <https://doi.org/10.1016/j.cemconres.2020.106070>
20. Wolfs RJM, Bos FP, Salet TAM (2018) Early age mechanical behaviour of 3D printed concrete: Numerical modelling and experimental testing. *Cement and Concrete Research* 106:103–116. <https://doi.org/10.1016/j.cemconres.2018.02.001>
21. Roussel N (2018) Rheological requirements for printable concretes. *Cement and Concrete Research* 112:.. <https://doi.org/10.1016/j.cemconres.2018.04.005>
22. Nerella VN, Krause M, Mechtcherine V (2018) Practice-Oriented Buildability Criteria for Developing 3D-Printable Concretes in the Context of Digital Construction
23. A critical review of preparation design and workability measurement of concrete material for largescale 3D printing — the UWA Profiles and Research Repository. <https://research-repository.uwa.edu.au/en/publications/a-critical-review-of-preparation-design-and-workability-measureme>. Accessed 14 Jan 2022
24. Kruger J, Zeranka S, van Zijl G (2019) Quantifying constructability performance of 3D concrete printing via rheology-based analytical models
25. Chen Y, He S, Zhang Y, et al (2021) 3D printing of calcined clay-limestone-based cementitious materials. *Cement and Concrete Research* 149:106553. <https://doi.org/10.1016/j.cemconres.2021.106553>
26. Mechtcherine V, Buswell R, Kloft H, et al (2021) Integrating reinforcement in digital fabrication with concrete: A review and classification framework. *Cement and Concrete Composites* 103964. <https://doi.org/10.1016/j.cemconcomp.2021.103964>
27. Asprone D, Menna C, Bos FP, et al (2018) Rethinking reinforcement for digital fabrication with concrete. *Cement and Concrete Research* 112:111–121. <https://doi.org/10.1016/j.cemconres.2018.05.020>

28. Kloft H, Empelmann M, Hack N, et al (2020) Reinforcement strategies for 3D-concrete-printing. *Civil Engineering Design* 2:131–139. <https://doi.org/10.1002/cend.202000022>
29. Doris (2016) V2 Vesta Beton-3D-Drucker baut kleines Haus. In: 3Druck.com - The Independent AM Magazine. <https://3druck.com/drucker-und-produkte/v2-vesta-beton-3d-drucker-baut-kleines-haus-2846225/>. Accessed 14 Jan 2022
30. Alawneh M, Matarneh M, El-Ashri S (2018) THE WORLD'S FIRST 3D-PRINTED OFFICE BUILDING IN DUBAI. 19
31. Mechtcherine V, Grafe J, Nerella VN, et al (2018) 3D-printed steel reinforcement for digital concrete construction – Manufacture, mechanical properties and bond behaviour. *Construction and Building Materials* 179:125–137. <https://doi.org/10.1016/j.conbuildmat.2018.05.202>
32. Asprone D, Auricchio F, Menna C, Mercuri V (2018) 3D printing of reinforced concrete elements: Technology and design approach. *Construction and Building Materials* 165:218–231. <https://doi.org/10.1016/j.conbuildmat.2018.01.018>
33. Bos FP, Ahmed ZY, Wolfs RJM, Salet TAM (2017) 3D printing concrete with reinforcement: 2017 fib Symposium, June 12–14, 2017, Maastricht, The Netherlands. *High Tech Concrete: where technology and engineering meet* 2484–2493. https://doi.org/10.1007/978-3-319-59471-2_283
34. Bos FP, Ahmed ZY, Jutinov ER, Salet TAM (2017) Experimental Exploration of Metal Cable as Reinforcement in 3D Printed Concrete. *Materials* 10:1314. <https://doi.org/10.3390/ma10111314>
35. Salet T, Ahmed Z, Bos F, Laagland H (2018) Design of a 3D printed concrete bridge by testing. *Virtual and Physical Prototyping* 13:1–15. <https://doi.org/10.1080/17452759.2018.1476064>
36. Vantygheem G, De Corte W, Shakour E, Amir O (2020) 3D printing of a post-tensioned concrete girder designed by topology optimization. *Automation in Construction* 112:103084. <https://doi.org/10.1016/j.autcon.2020.103084>

37. Amir O, Shakour E (2018) Simultaneous shape and topology optimization of prestressed concrete beams. *Structural and Multidisciplinary Optimization* 57:1-8. <https://doi.org/10.1007/s00158-017-1855-5>
38. Kinomura K, Murata S, Yamamoto Y, et al (2020) Application of 3D Printed Segments Designed by Topology Optimization Analysis to a Practical Scale Prestressed Pedestrian Bridge. pp 658–668
39. Perrot A, Rangeard D, Pierre A (2015) Structural built-up of cement-based materials used for 3D-printing extrusion techniques. *Materials and Structures* 49:1–8. <https://doi.org/10.1617/s11527-015-0571-0>
40. Kruger J, Zeranka S, van Zijl G (2019) 3D concrete printing: A lower bound analytical model for buildability performance quantification. *Automation in Construction* 106:102904. <https://doi.org/10.1016/j.autcon.2019.102904>
41. Reiter L, Wangler T, Anton A, Flatt RJ (2020) Setting on demand for digital concrete – Principles, measurements, chemistry, validation. *Cement and Concrete Research* 132:106047. <https://doi.org/10.1016/j.cemconres.2020.106047>
42. Mettler LK, Wittel FK, Flatt RJ, Herrmann HJ (2016) Evolution of strength and failure of SCC during early hydration. *Cement and Concrete Research* 89:288–296. <https://doi.org/10.1016/j.cemconres.2016.09.004>
43. Wolfs RJM, Bos FP, Salet TAM (2019) Triaxial compression testing on early age concrete for numerical analysis of 3D concrete printing. *Cement and Concrete Composites* 104:103344. <https://doi.org/10.1016/j.cemconcomp.2019.103344>
44. EN 12390-3:2019 - Testing hardened concrete - Part 3: Compressive strength of test specimens. In: iTeh Standards Store. <https://standards.iteh.ai/catalog/standards/cen/7eb738ef-44af-436c-ab8e-e6561571302c/en-12390-3-2019>. Accessed 21 May 2021
45. Panda B, Lim JH, Tan MJ (2019) Mechanical properties and deformation behaviour of early age concrete in the context of digital construction. *Composites Part B: Engineering* 165:563–571. <https://doi.org/10.1016/j.compositesb.2019.02.040>

46. Le TT, Austin SA, Lim S, et al (2012) Mix design and fresh properties for high-performance printing concrete. *Mater Struct* 45:1221–1232. <https://doi.org/10.1617/s11527-012-9828-z>
47. Kazemian A, Yuan X, Cochran E, Khoshnevis B (2017) Cementitious materials for construction-scale 3D printing: Laboratory testing of fresh printing mixture. *Construction and Building Materials* 145:639–647. <https://doi.org/10.1016/j.conbuildmat.2017.04.015>
48. Wolfs RJM, Suiker ASJ (2019) Structural failure during extrusion-based 3D printing processes. *Int J Adv Manuf Technol* 104:565–584. <https://doi.org/10.1007/s00170-019-03844-6>
49. Paul S, Wei Y, Tay YWD, et al (2017) Fresh and hardened properties of 3D printable cementitious materials for building and construction. *Archives of Civil and Mechanical Engineering* 18:. <https://doi.org/10.1016/j.acme.2017.02.008>
50. Wolfs RJM, Bos FP, Salet TAM (2019) Hardened properties of 3D printed concrete: The influence of process parameters on interlayer adhesion. *Cement and Concrete Research* 119:132–140. <https://doi.org/10.1016/j.cemconres.2019.02.017>
51. Le T, Austin S, Lim S, et al (2012) Hardened properties of high-performance printing concrete. *Cement and Concrete Research* 42:558–566. <https://doi.org/10.1016/j.cemconres.2011.12.003>
52. Mechanical properties of structures 3D printed with cementitious powders - ScienceDirect. <https://www.sciencedirect.com/science/article/abs/pii/S095006181500690X>. Accessed 11 Jan 2022
53. Thomas RJ, Sorensen AD (2017) Review of strain rate effects for UHPC in tension. *Construction and Building Materials* 153:846–856. <https://doi.org/10.1016/j.conbuildmat.2017.07.168>
54. Kruger J, Zeranka S, van Zijl G (2019) An ab initio approach for thixotropy characterisation of (nanoparticle-infused) 3D printable concrete. *Construction and Building Materials* 224:372–386. <https://doi.org/10.1016/j.conbuildmat.2019.07.078>

55. Greenhill (1882) A.-G. GREENHILL. - Determination of the greatest height consistent with stability that a vertical pole or mast can be made, and of the greatest height to which a tree of given proportions can grow (Hauteur maxima compatible avec la stabilité d'une tige verticale ou d'un mât. Hauteur à laquelle peut croître un arbre de proportions connues); Proc. of Camb. phil. Soc., vol. IV, Part II, 1881. J Phys Theor Appl 1:337–338. <https://doi.org/10.1051/jphysap:018820010033701>
56. Suiker ASJ (2018) Mechanical performance of wall structures in 3D printing processes: Theory, design tools and experiments. International Journal of Mechanical Sciences 137:145–170. <https://doi.org/10.1016/j.ijmecsci.2018.01.010>
57. Schuler H, Mayrhofer C, Thoma K (2006) Spall experiments for the measurement of the tensile strength and fracture energy of concrete at high strain rates. International Journal of Impact Engineering 10:1635–1650. <https://doi.org/10.1016/j.ijimpeng.2005.01.010>
58. Matsoukas A, Mitsoulis E (2003) Geometry effects in squeeze flow of Bingham plastics. Journal of Non-Newtonian Fluid Mechanics 109:231–240. [https://doi.org/10.1016/S0377-0257\(02\)00170-2](https://doi.org/10.1016/S0377-0257(02)00170-2)
59. Qian Y, Kawashima S (2016) Use of creep recovery protocol to measure static yield stress and structural rebuilding of fresh cement pastes. Cement and Concrete Research 90:73–79. <https://doi.org/10.1016/j.cemconres.2016.09.005>
60. Sun Z, Voigt T, Shah SP (2006) Rheometric and ultrasonic investigations of viscoelastic properties of fresh Portland cement pastes. Cement and Concrete Research 36:278–287. <https://doi.org/10.1016/j.cemconres.2005.08.007>
61. Grasley Z, Lange D (2007) Constitutive modeling of the aging viscoelastic properties of portland cement paste. Mechanics of Time-Dependent Materials 11:175–198. <https://doi.org/10.1007/s11043-007-9043-4>
62. Poole R (2012) The Deborah and Weissenberg numbers. The British Society of Rheology - Rheology Bulletin 53:32–39
63. Mohan MK, Rahul AV, De Schutter G, Van Tittelboom K (2021) Extrusion-based concrete 3D printing from a material perspective: A

- state-of-the-art review. *Cement and Concrete Composites* 115:103855. <https://doi.org/10.1016/j.cemconcomp.2020.103855>
64. Maia L, Figueiras J (2012) Early-age creep deformation of a high strength self-compacting concrete. *Construction and Building Materials* 34:602–610. <https://doi.org/10.1016/j.conbuildmat.2012.02.083>
65. Leemann A, Lura P, Loser R (2011) Shrinkage and creep of SCC – The influence of paste volume and binder composition. *Construction and Building Materials* 25:2283–2289. <https://doi.org/10.1016/j.conbuildmat.2010.11.019>
66. Rozière E, Granger S, Turcry Ph, Loukili A (2007) Influence of paste volume on shrinkage cracking and fracture properties of self-compacting concrete. *Cement and Concrete Composites* 29:626–636. <https://doi.org/10.1016/j.cemconcomp.2007.03.010>
67. Briffaut M, Benboudjema F, Torrenti J-M, Nahas G (2012) Concrete early age basic creep: Experiments and test of rheological modelling approaches. *Construction and Building Materials* 36:373–380. <https://doi.org/10.1016/j.conbuildmat.2012.04.101>
68. Han B, Xie H-B, Zhu L, Jiang P (2017) Nonlinear model for early age creep of concrete under compression strains. *Construction and Building Materials* 147:203–211. <https://doi.org/10.1016/j.conbuildmat.2017.04.119>
69. De Schutter G (1999) Degree of hydration based Kelvin model for the basic creep of early age concrete. *Materials and Structures* 32:260–265. <https://doi.org/10.1007/BF02479595>
70. Niyogi AK, Hsu P, Meyers BL (1973) The influence of age at time of loading on basic and drying creep. *Cement and Concrete Research* 3:633–644. [https://doi.org/10.1016/0008-8846\(73\)90100-2](https://doi.org/10.1016/0008-8846(73)90100-2)
71. Østergaard L, Lange DA, Altoubat SA, Stang H (2001) Tensile basic creep of early-age concrete under constant load. *Cement and Concrete Research* 31:1895–1899. [https://doi.org/10.1016/S0008-8846\(01\)00691-3](https://doi.org/10.1016/S0008-8846(01)00691-3)
72. Ghosh RS (1972) Creep of portland cement paste at early ages. *Mat Constr* 5:93–97. <https://doi.org/10.1007/BF02478438>

73. Bazant ZP, Chern JC (1985) Concrete creep at variable humidity: constitutive law and mechanism. *Materials and Structures* 18:1. <https://doi.org/10.1007/BF02473360>
74. Burgers JM (1935) Mechanical considerations-model systems-phenomenological theories of relaxation and of viscosity,
75. Banks HT, Hu S, Kenz ZR (2011) A Brief Review of Elasticity and Viscoelasticity for Solids. *Advances in Applied Mathematics and Mechanics* 3:1–51. <https://doi.org/10.4208/aamm.10-m1030>
76. Casagrande L, Esposito L, Menna C, et al (2020) Effect of testing procedures on buildability properties of 3D-printable concrete. *Construction and Building Materials* 245:118286. <https://doi.org/10.1016/j.conbuildmat.2020.118286>
77. D18 Committee Test Method for Unconfined Compressive Strength of Cohesive Soil. ASTM International
78. Yu K, McGee W, Ng TY, et al (2021) 3D-printable engineered cementitious composites (3DP-ECC): Fresh and hardened properties. *Cement and Concrete Research* 143:106388. <https://doi.org/10.1016/j.cemconres.2021.106388>
79. Bažant ZP (2001) Prediction of concrete creep and shrinkage: past, present and future. *Nuclear Engineering and Design* 203:27–38. [https://doi.org/10.1016/S0029-5493\(00\)00299-5](https://doi.org/10.1016/S0029-5493(00)00299-5)
80. Bažant Z (1995) Creep and shrinkage prediction model for analysis and design of concrete structures— model B3. *Materials and Structures* 28:357–365. <https://doi.org/10.1007/BF02473152>
81. Paul S, van Zijl G, Tan MJ, Gibson I (2018) A review of 3D concrete printing systems and materials properties: current status and future research prospects. *Rapid Prototyping Journal* 24:00–00. <https://doi.org/10.1108/RPJ-09-2016-0154>
82. Tay YWD, Ting GH, Qian Y, et al (2018) Time gap effect on bond strength of 3D-printed concrete. *Virtual and Physical Prototyping* 14:104–113. <https://doi.org/10.1080/17452759.2018.1500420>
83. Mechtcherine V, Michel A, Liebscher M, Schmeier T (2020) Extrusion-Based Additive Manufacturing with Carbon Reinforced

Concrete: Concept and Feasibility Study. *Materials* 13:2568.
<https://doi.org/10.3390/ma13112568>

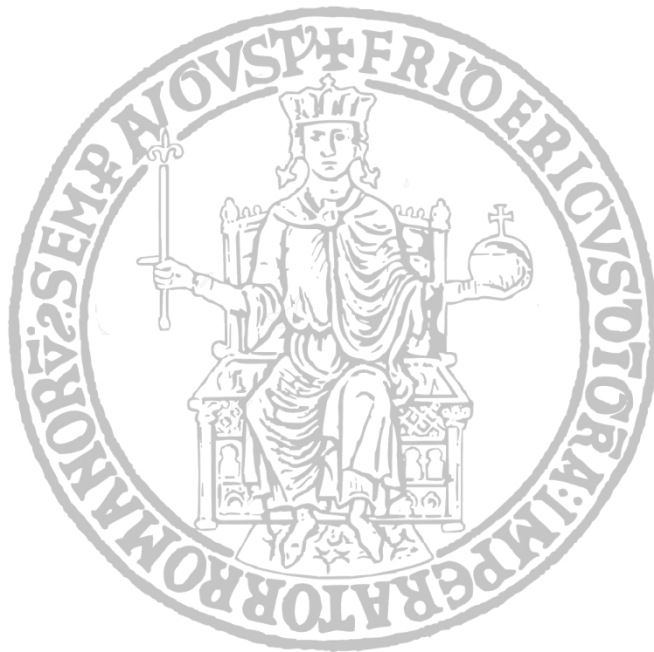
84. Bos FP, Ahmed ZY, Jutinov ER, Salet TA (2017) Experimental Exploration of Metal Cable as Reinforcement in 3D Printed Concrete. *Materials* 10:1314
85. RILEM TC (1994) RC 6 Bond test for reinforcement steel. 2. Pull-out test, 1983. In: RILEM Recommendations for the Testing and Use of Constructions Materials. E & FN Spon, London, pp 218–220
86. Baz B, Aouad G, Remond S (2020) Effect of the printing method and mortar's workability on pull-out strength of 3D printed elements. *Construction and Building Materials* 230:117002.
<https://doi.org/10.1016/j.conbuildmat.2019.117002>
87. Baz B, Aouad G, Leblond P, et al (2020) Mechanical assessment of concrete – Steel bonding in 3D printed elements. *Construction and Building Materials* 256:119457.
<https://doi.org/10.1016/j.conbuildmat.2020.119457>
88. Ding T, Qin F, Xiao J, et al (2022) Experimental study on the bond behaviour between steel bars and 3D printed concrete. *Journal of Building Engineering* 49:104105.
<https://doi.org/10.1016/j.jobee.2022.104105>
89. Sun X, Gao C, Wang H (2021) Bond performance between BFRP bars and 3D printed concrete. *Construction and Building Materials* 269:121325. <https://doi.org/10.1016/j.conbuildmat.2020.121325>
90. Reiter L, Wangler T, Anton A, Flatt RJ (2020) Setting on demand for digital concrete – Principles, measurements, chemistry, validation. *Cement and Concrete Research* 132:106047.
<https://doi.org/10.1016/j.cemconres.2020.106047>
91. Roussel N (2018) Rheological requirements for printable concretes. *Cement and Concrete Research* 112:.
<https://doi.org/10.1016/j.cemconres.2018.04.005>
92. fib Model Code 2010 (2013) fib Model Code for Concrete Structures 2010

93. (2016) EN 196-1:2016 - Methods of testing cement - Part 1: Determination of strength. Accessed 28 Jul 2021
94. Anton A, Reiter L, Wangler T, et al (2021) A 3D concrete printing prefabrication platform for bespoke columns. *Automation in Construction* 122:103467. <https://doi.org/10.1016/j.autcon.2020.103467>
95. Goto Y (1971) CRACKS FORMED IN CONCRETE AROUND DEFORMED TENSION BARS. *Am Concrete Inst Journal & Proceedings*
96. (2004) Eurocode 2: Design of concrete structures (EN 1992). <https://www.ds.dk/en/our-services/eurocodes/technical-standards/eurocode-2>. Accessed 30 Sep 2021
97. Tepfers R, Achillides Z, Azizinamini A, et al (2000) fib Bulletin 10. Bond of reinforcement in concrete. fib. The International Federation for Structural Concrete
98. Ferguson (chairman) AC 408 PM (1966) Bond Stress-The State of the Art. *JP* 63:1161–1190. <https://doi.org/10.14359/7665>
99. Diab AM, Elyamany HE, Hussein MA, Al Ashy HM (2014) Bond behavior and assessment of design ultimate bond stress of normal and high strength concrete. *Alexandria Engineering Journal* 53:355–371. <https://doi.org/10.1016/j.aej.2014.03.012>
100. Arel H, Yazıcı Ş (2015) The effect of different parameters on the concrete -bar bond. 22:
101. ACI CODE 318-08: Building Code Requirements for Structural Concrete and Commentary. https://www.concrete.org/store/productdetail.aspx?ItemID=31808&Language=English&Units=US_Units. Accessed 3 Mar 2022
102. [PDF] Topology Optimization for Additive Manufacturing | Semantic Scholar. <https://www.semanticscholar.org/paper/Topology-Optimization-for-Additive-Manufacturing-Brackett-Ashcroft/1bb56e8c9e8e5cbf8bbfcb935f1047ae42a048d9>. Accessed 10 Jan 2022

103. M SV and N (2018) Critical Reviews on Topology Optimisation of Reinforced Concrete. Trends in Civil Engineering and its Architecture 1:001–004
104. A critical evaluation of topology optimization results for strut-and-tie modeling of reinforced concrete - Xia - 2020 - Computer-Aided Civil and Infrastructure Engineering - Wiley Online Library. <https://onlinelibrary.wiley.com/doi/full/10.1111/mice.12537>. Accessed 10 Jan 2022
105. Application of 3D Printed Segments Designed by Topology Optimization Analysis to a Practical Scale Prestressed Pedestrian Bridge. In: [springerprofessional.de](https://www.springerprofessional.de). <https://www.springerprofessional.de/en/application-of-3d-printed-segments-designed-by-topology-optimiza/18155802>. Accessed 10 Jan 2022
106. Pastore T, Mercuri V, Menna C, et al (2019) Topology optimization of stress-constrained structural elements using risk-factor approach. Computers & Structures 224:. <https://doi.org/10.1016/j.compstruc.2019.106104>
107. Gonçalves JF, Resende MGC (2011) Biased random-key genetic algorithms for combinatorial optimization. J Heuristics 17:487–525. <https://doi.org/10.1007/s10732-010-9143-1>
108. Bean JC (1994) Genetic Algorithms and Random Keys for Sequencing and Optimization. ORSA Journal on Computing 6:154–160. <https://doi.org/10.1287/ijoc.6.2.154>
109. Pastore T, Menna C, Asprone D (2022) Bézier-based biased random-key genetic algorithm to address printability constraints in the topology optimization of concrete structures. Struct Multidisc Optim 65:64. <https://doi.org/10.1007/s00158-021-03119-3>
110. Design of novel nozzles for higher interlayer strength of 3D printed cement paste - ScienceDirect. <https://www.sciencedirect.com/science/article/pii/S2214860421006047>. Accessed 10 Jan 2022
111. Mohammad M, Masad E, Al-Ghamdi SG (2020) 3D Concrete Printing Sustainability: A Comparative Life Cycle Assessment of

Four Construction Method Scenarios. Buildings 10:.
<https://doi.org/10.3390/buildings10120245>

112. Mechtcherine V, Buswell R, Kloft H, et al (2021) Integrating reinforcement in digital fabrication with concrete: A review and classification framework. Cement and Concrete Composites 119:103964. <https://doi.org/10.1016/j.cemconcomp.2021.103964>



Author's publications

1. Esposito, L., Casagrande, L., Menna, C., D. Asprone, F. Auricchio. Early-age creep behaviour of 3D printable mortars: Experimental characterisation and analytical modelling. *Mater Struct* 54, 207 (2021). <https://doi.org/10.1617/s11527-021-01800-z>
2. Asprone D. et al. (2022) Structural Design and Testing of Digitally Manufactured Concrete Structures. In: Roussel N., Lowke D. (eds) *Digital Fabrication with Cement-Based Materials*. RILEM State-of-the-Art Reports, vol 36. Springer, Cham. https://doi.org/10.1007/978-3-030-90535-4_6
3. L. Casagrande, L. Esposito, C. Menna, D. Asprone, F. Auricchio (2019). Effect of testing procedures on buildability properties of 3D-printable concrete. *Construction and building material*, Elsevier. <https://doi.org/10.1016/j.conbuildmat.2020.118286>.
4. Bilotta, A. Compagnone, L. Esposito and E. Nigro (2019). Structural behaviour of steel and FRP reinforced concrete slabs in fire. *Engineering Structure*, Elsevier. <https://doi.org/10.1016/j.engstruct.2020.111058>
5. Laura Esposito, Marta Fioretti, Francesco Lo Monte, Costantino Menna, Domenico Asprone, Liberato Ferrara. Experimental investigation on mechanical behaviour of fiber reinforced mortar used in 3D concrete printing. *Italian Concrete Days 2021* (online conference).
6. L. Esposito, M. Fioretti, M. Cucchi, F. Lo Monte, C. Menna, S. Moro, D. Asprone, and L. Ferrara (2019). Early age fracture performance of 3D printable fiber reinforced cementitious composites. *The New Boundaries of Structural Concrete 2019*, ACI Italy Chapter.
7. Bilotta, A. Compagnone, L. Esposito and E. Nigro (2019). Reinforced Concrete Slabs in Fire: Effect of Reinforcement Type and Static Scheme. *The New Boundaries of Structural Concrete 2019*, ACI Italy Chapter.
8. Bilotta, A. Compagnone, L. Esposito and E. Nigro (2019). Numerical analyses of the structural behaviour of steel and FRP reinforced slabs in fire. *Applications of Structural Fire Engineering*, 13-14 June 2019, Singapore.
9. Bilotta, A. Compagnone, L. Esposito and E. Nigro (2019). Effect of the static scheme on the behaviour of FRP reinforced concrete slabs in fire. *IFireSS 2019 – 3rd International Fire Safety Symposium Ottawa, Ontario, Canada, June 5-7, 2019*.
10. L. Casagrande, L. Esposito, C. Menna, D. Asprone, F. Auricchio. (2020). Mechanical Characterization of Cement-Based Mortar Used in 3DCP Including Early-Age Creep Effects. *Digital Concrete 2020* (online conference) 10.1007/978-3-030-49916-7_42.
11. M. Fioretti, S. Kompella, F. Lo Monte, L. Esposito, C. Menna, S. Moro, D. Asprone, L. Ferrara. (2020). Experimental Investigation on the Early Age Tensile Strength of Fiber Reinforced Mortar Used in 3D Concrete Printing. *Digital Concrete 2020* (online conference). 10.1007/978-3-030-49916-7_26.
12. L. Esposito, C. Menna, D. Asprone, C. Rossino, M. Marchi. (2020). An Experimental Testing Procedure to Assess the Buildability Performance of 3D Printed Concrete Elements. *Digital Concrete 2020* (online conference). 10.1007/978-3-030-49916-7_24.

13. Costantino Menna and Laura Esposito. Flexural behaviour of steel reinforced topology-optimised beams fabricated by 3D concrete printing. *Digital Concrete 2022* (accepted).
14. Laura Esposito, Lukas Gebhard, Costantino Menna, Jaime Mata-Falcon. Inter-laboratory study on the influence of 3D concrete printing setups on the bond behaviour of various reinforcements. (under review).
15. Costantino Menna and Laura Esposito. Design and assessment of steel reinforced topology-optimised beams fabricated by 3D concrete printing. (in preparation).
16. Pierluca Vitale, Costantino Menna, Laura Esposito, Maurizio Marchi. Environmental performances of 3DCP beam: a comparative LCA of innovative and conventional construction technique. (in preparation).
17. Laura Esposito, Costantino Menna, Martina Palomba, Luca Setti, Maurizio Marchi. Early age behaviour of fresh 3D printable mortar. (in preparation).